Microseismicity and the Dynamics of Rutford Ice Stream, West Antarctica

Emma C. Smith

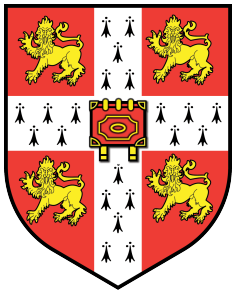

St Edmund's College
University of Cambridge

November 2015

This dissertation is submitted to for the degree of Doctor of Philosophy

Declaration

This dissertation describes my original work except where acknowledgement is made in the text. It does not exceed the page limit and is not substantially the same as any work that has been, or is being submitted to any other university for any degree, diploma or any other qualification.

- Emma C. Smith
November 2015

"He was determined to discover the underlying logic behind the universe. Which was going to be hard, because there wasn't one."

- Sir. Terry Pratchett, *Mort*

"So it goes."

- Kurt Vonnegut Jr., *Slaughterhouse-Five*

Acknowledgements

I am sure this is the point where I am suppose to write something very poignant, but after several months of feverish dissertation writing I feel like I have used up all the words I have and I am simply left with: Thank you!

Thank you first of all to my academic supervisors, Andy Smith from the British Antarctic Survey and Bob White from the University of Cambridge. From devising the project in the first place to endlessly proof reading manuscripts, you have both been integral parts of my academic career and have given me so many amazing opportunities over the past 4 years. Equally I would like to thank Alex at BAS and Alan and Mike at The University of Bristol, they have all been unofficial supervisors and given me a huge amount of their time and patience. The data set used in this study was collected by Hamish and Chris and it goes without saying that without their efforts in the field none of this would have been possible.

To my Bullard family: Tim, Rob, David, Jenny, Jenny, Tobba, Grace and Karen, you have been amazing people to work, play and laugh with! To my BAS Ph.D. crew: Sarah and Jim, I can't beleive we have all survived...now how about those BAS tatoos? I have been fortunate to have had many inspiring conversations and discussion that have helped me along the way, I would particularly like to thank Sebastian and Jerome for this.

So many people in Cambridge have extended their help and friendship during my time here. Jenny, Cat, Matea, Emily, Siobhan and Trish - the 'Richmond Towers' crew and associates have always had a wise word and a glass of wine for me. My BAS family: Jan, Toshington, Rowan, Emily, Clare, Chris and many more... I will have many incredible memories of slacklining in the park and drinking pints like a pirate! At Bullard: Gill, Joyce, Dave and Ian, who keep the whole place running smoothly and a second thanks to Dave for all the roast chicken dinners and highly opinonated 'debate'. A huge thanks to Jen and Rob for putting a roof over my head in my last few months, it's been a pleasure living with you both!

Tom and Debbie thank you for the cups of tea and shared love of Radio 4 comedy. Mel, Ben and Ian, you have always supported me during the good and bad and given me the strength to battle on. Lauren, you are the best egg! Thank you to James for both giving me the encouragement to apply for this Ph.D. and proof reading my application at an ungodly hour of the morning it was due and to Adam for suggesting it in the first place. To Roger Clark and Tim Clarke for giving me the encouragement to take the first steps towards this path.

Finally, my family: Mum, Dad, Adam, Paul and Auntie Pam - you have always supported me.

The last 4 years have been a crazy ride and I am hounoured, privilaged and grateful to have shared it with so many amazing people from all over the world. There have been too many of you to mention you all in person and sorry to anyone I have inadvertantly overlooked.

Cheers, Skál, Santé, Salud and Sláinte !

Microseismicity and the Dynamics of Rutford Ice Stream, West Antarctica

Emma C. Smith

The West Antarctic Ice Sheet (WAIS) discharges the majority of its mass through fast flowing ice streams. Understanding the dynamics of how and why these ice streams flow in the way that they do is fundamental to our ability to predict the evolution of WAIS and its future contribution to global sea level. Natural seismicity generated at the base of Rutford Ice Stream, West Antarctica, was recorded over a 34-day period using ten three-component geophones 40 km upstream of the grounding line. In this dissertation I use these data to detect and locate $\sim$ 3000 microseismic events in discrete spatial clusters around the ice-bed interface. I interpret the cluster locations as 'sticky spots' of stiff basal sediment within a matrix of deforming basal sediment at the ice-bed interface, where ice movement is accommodated by stick-slip basal sliding generating the observed seismicity. I use the shear waves generated to measure anisotropy in the ice fabric and show that the ice in this region has formed a fabric pattern consistent with ice flow in a laterally confined ice stream environment, suggesting the ice is accommodating flow by internal deformation as well as basal processes.

I make a thorough investigation of the uncertainties in hypocentral locations using synthetic testing and show that despite poor vertical resolution in the data, the events are likely to originate at the ice-bed interface, rather than in the ice or subglacial sediment. I investigate the source characteristics of the events by constructing fault plane solutions determining event magnitudes and fault geometry. The source mechanisms are the same across the survey area and are interpreted as sub-horizontal, low-angle faulting, slipping in the ice flow direction. The displacement for an individual slip on a 'sticky spot' is small as is the associated stress drop. This leads to the conclusion that 'sticky spots' probably accommodate only a small amount of the total basal motion. Seismicity at a cluster location turns on and off over time suggesting that a 'sticky spot' activates repeatedly. The timing of events shows no systematic pattern in space or time, suggesting that seismicity is relatively insensitive to periodic changes in surface velocity, caused by changes in basal stresses transmitted up stream from the grounding line.

I present measurements of shear wave splitting in the data set and use these to construct a model of the elastic anisotropy in this area of Rutford Ice Stream. I then use these results to invert for ice crystal orientation fabric and show how the ice fabric in the area is clearly influenced by the ice stream flow environment.

This dissertation highlights passive microseismic monitoring as a key tool for investigating both ice-bed interface characteristics and internal ice fabric in Rutford Ice Stream. The techniques established here can be more generally applied to provide analogous information in other fast-flowing ice stream environments . I show that passive microseismic monitoring adds new and complementary information about basal material characteristics to an area that has already been well studied using other geophysical methods. In particular, I show direct evidence that stick-slip basal motion accommodates ice stream flow in parts of this study area, and that this happens in combination with aseismic basal motion. I also show that the relationship between ice surface velocity and basal seismicity rates is not simple. This implies that the mechanism for transmission of stress changes, due to tidal forcing, upstream from the grounding line is complex. I provide the first conclusive study of ice fabric using passive microseismic monitoring. I show that the ice fabric in Rutford Ice Stream, a typical convergent flow environment, has formed a distinctive partial girdle fabric. This result is likely to be typical of many ice stream areas, and has significant implications for modelling of anisotropic ice flow.

Publications arising from this dissertation:

Smith, E. C., A. M. Smith, R. S. White, A. M. Brisbourne, and H. D. Pritchard (2015), Mapping the Ice-Bed Interface Characteristics of Rutford Ice Stream , West Antarctica, Using Microseismicity, *J. Geophys. Res. Earth Surf, 120*, 1881-1894, doi:10.1002/2015JF003587.

Contents

List of Figures

Chapter 1

Introduction

1.1 Motivation

The cryosphere accounts for around 75% of the world's fresh water (*Lemke et al.*, 2007) with the majority of this being stored in the ice sheets of Greenland and Antarctica. The West Antarctic Ice Sheet (WAIS) contains enough water to raise global sea level by approximately 5 to 6 m (*Tol et al.*, 2006) and according to the marine ice sheet instability (MISI) hypothesis, is inherently unstable. This states that an ice sheet largely grounded below sea level with a bed that slopes downwards from the coast to the interior, will suffer rapid retreat of the grounding line inland if the ice shelves (floating portion of the ice stream beyond the grounding line) that buttress many of these unstable regions are removed (*Mercer*, 1978), or the ice at the grounding line thins. WAIS fits the criteria for the MISI hypothesis over the majority of its extent (Figure 1.1) and evidence suggests that it has completely collapsed during some past inter-glacial periods (*Scherer et al.*, 1998). Understanding the processes that control movement of ice from WAIS into the oceans is therefore fundamental to our ability to predict the evolution of WAIS and its future contribution to global sea level. It is well established that ice sheets discharge the majority of their mass (*Bamber et al.*, 2000) through fast-flowing ice streams (Figure 1.2), what is still not as well understood is the processes that control the flow of ice streams.

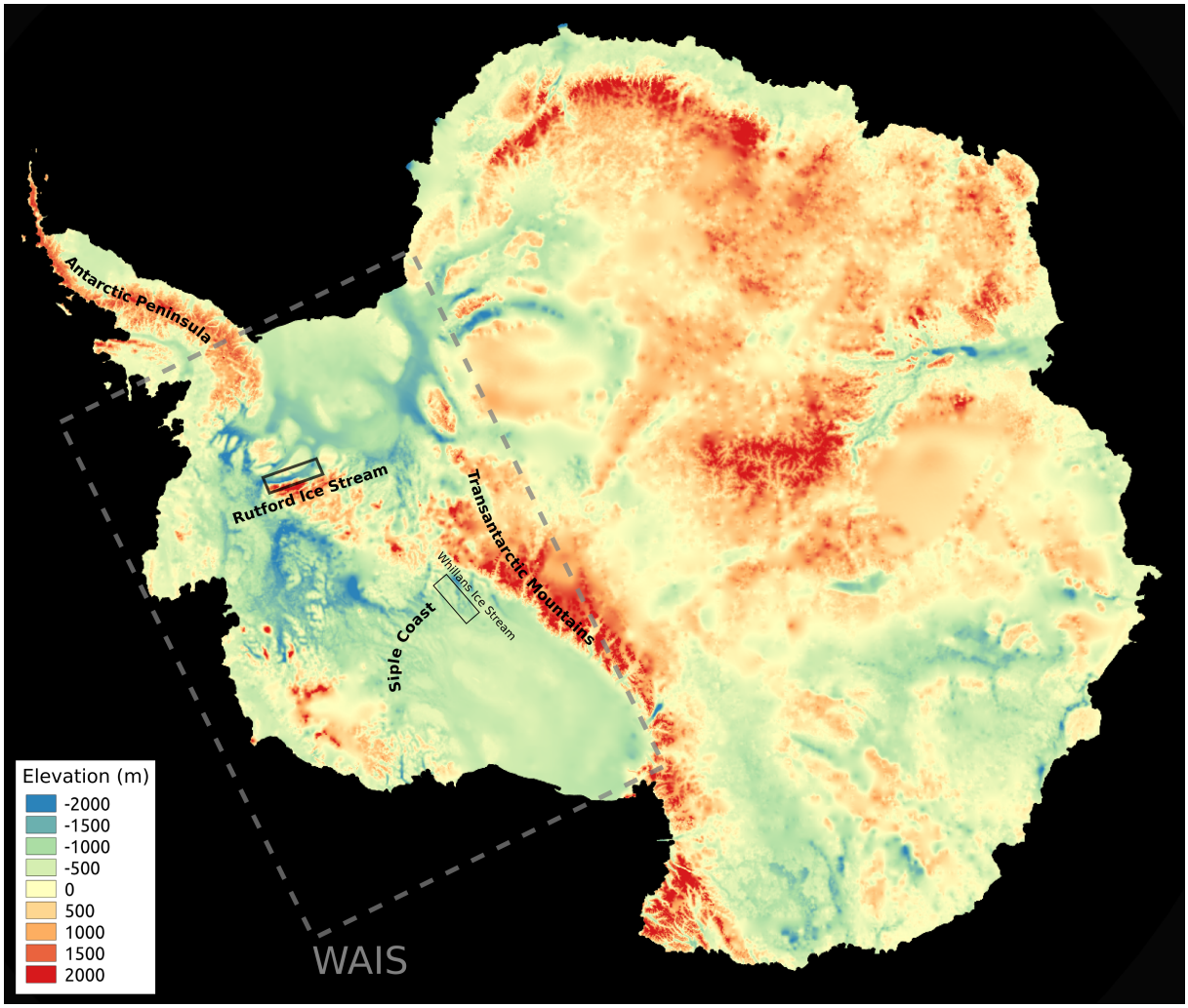

Figure 1.1: ***Antarctic bed topography***. *BEDMAP2 image of Antarctic bed topography (Fretwell et al., 2013). View as if all ice was removed. East and West Antarctica are separated by the Transantarctic Mountains, West Antarctica is approximately highlighted in the dashed box. A large proportion of the bed of West Antarctica is below sea level (green and blue colours) meaning WAIS is a marine ice sheet. Rutford Ice Stream is shown in the black box and is grounded below sea level. The Siple Coast region, also grounded below sea level, is indicated.*

An ice stream is a fast-flowing region of grounded ice within an ice sheet (*Paterson*, 1994). Strictly it should be bounded by slower moving ice, because if it is bounded by rock it is termed an outlet glacier, but this is often not simply defined. From now on the term 'ice stream' (Figure 1.2) will be used to refer to all fast-flowing ice sheet outlets and 'glacier' will refer to mountain and valley glaciers. Ice stream motion is accommodated by internal

deformation (the creep of ice crystals under stress) and by processes that occur at the base of the ice, both sliding over a consolidated (non-deforming) bed and deformation of water saturated subglacial sediments (*Paterson*, 1994). In general, basal processes dominate in ice streams. Understanding both the internal ice fabric structure of ice streams and the basal processes at work beneath them will improve models of these areas and lead to a better understanding of their response to external stimuli. The major challenge in investigating this is observing the ice column and base of the ice, in areas where the ice can be several kilometres thick.

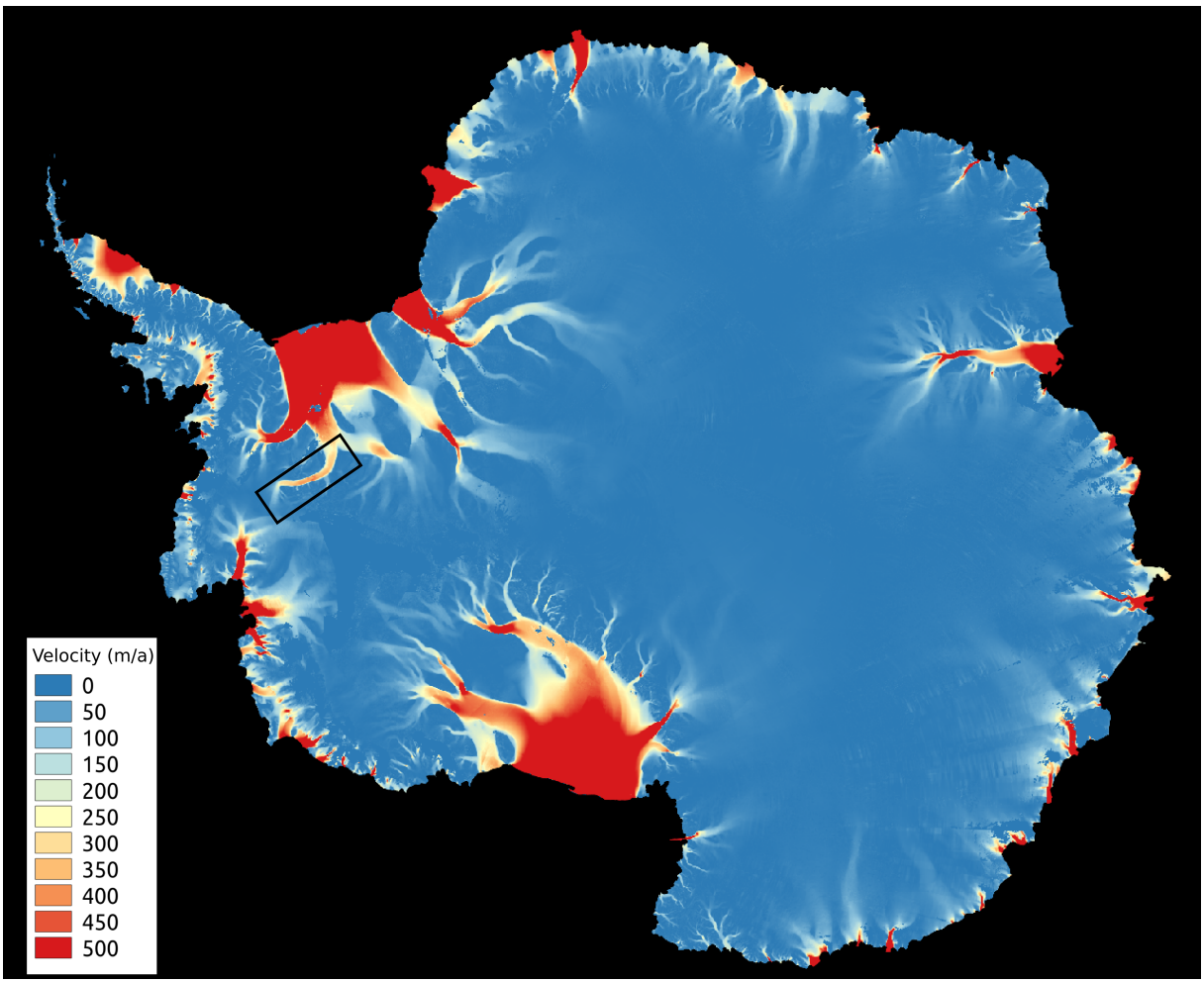

Figure 1.2: ***The surface velocity of ice in Antarctica****. Areas shown in blue are slow moving, red and orange features are fast moving ice streams and ice shelves. Rutford Ice Stream is shown in the black box. Created from InSAR satellite data (Rignot et al., 2011)*

Direct observation by drilling is possible (e.g., *Engelhardt et al.*, 1990), but this method is limited by logistical difficulties in drilling in an ice stream environment and only gives an insight into a very specific area of the ice stream bed. Geophysical methods allow indirect observation of both the ice column and the basal environment over a much larger geographical area.

In Antarctica, seismic reflection and radio echo sounding (RES) surveys have been used extensively to map the ice-bed interface and to provide details of spatial variation in basal material and hydrology (e.g., *Blankenship et al.*, 1986; *Smith*, 1997b; *Murray et al.*, 2008; *Fretwell et al.*, 2013). Repeat observations have also been used to infer temporal changes in basal conditions (*Smith et al.*, 2007), showing that subglacial bedforms and properties can evolve over decadal timescales or less. A more recent addition to these techniques is passive monitoring of natural seismic emissions from the base of ice streams, a technique derived from classical earthquake seismology. The emissions, known as icequakes, produce both P-wave and S-wave signals and provide a direct record of not just the spatial but also the temporal seismicity associated with ice movement. Since the first study by *Blankenship et al.* (1987), the technique has been used to infer basal conditions (e.g., *Anandakrishnan and Bentley*, 1993; *Smith*, 2006), to track subglacial water movement (*Winberry et al.*, 2009), to investigate ice fabric (*Harland et al.*, 2013) and to infer grounding zone conditions (*Pratt et al.*, 2014). This dissertation investigates the dynamics of Rutford Ice Stream, West Antarctica (Figure 1.2) using a passive microseismic data set recorded on Rutford Ice Stream, over a 34-day period during the austral summer of 2008/09.

1.2 Scope of Dissertation

The overall aims of this study are three-fold:

1. To highlight the use of passive microseismic monitoring as an effective method of investigating ice stream basal dynamics and internal ice structure.
2. To build upon data from independent active seismic and RES surveys to put together a robust interpretation of the basal characteristics and dynamics that govern the flow of Rutford Ice Stream.
3. To establish a model of internal ice fabric structure in this area of Rutford Ice Stream.

The remainder of **Chapter 1** gives a review of relevant literature and some brief theory covering the use of passive microseismic monitoring in ice and studies of ice crystal fabrics. It also provides an overview of the study area on Rutford Ice Stream, including a summary of previous work in the area.

In **Chapter 2**, I describe the data acquisition and give an overview of the 34-days of data that were collected including data preparation and quality control checks. This chapter contains a description of the methods that have been used both to locate the microseismic events and analyse shear wave splitting in the data.

In **Chapter 3**, I present the results of the earthquake locations and provide a thorough investigation into the uncertainties on the locations using synthetic testing, which is particularly important for a sparse network, such as the one described in this study. The timing of events is investigated with respect to a changing ice stream surface velocity in this area. I discuss how the location and timing of these events can be used to infer characteristics of the basal environment on Rutford Ice Stream and how the ice stream motion may be accommodated by this environment. This chapter includes work published in *Smith et al.* (2015) and extends aspects of it substantially.

Chapter 4 builds upon and extends the conclusions of Chapter 3. I investigate the source characteristics of the data by constructing fault plane solutions, determining event magnitudes and fault geometry and linking these together to look at the amount of basal shear stress accommodated by seismic deformation. The timing of events are re-assessed to show

how the changing surface velocity of the ice stream can be linked to event magnitude and thus changing basal stress conditions.

In **Chapter 5**, I present measurements of shear wave splitting in the data set and use these to construct a model of the elastic anisotropy in this area of Rutford Ice Stream. These results are then used to invert for ice crystal orientation fabric and show how the ice fabric in the area is clearly influenced by the ice stream flow environment. As far as I am aware, this is the most comprehensive measurement of ice anisotropy from a passive microseismic data set to date.

Chapter 6 provides a synthesis of all the elements of this thesis and how they come together to provide an understanding of the dynamics of Rutford Ice Stream. I show how both the basal dynamics and internal ice fabric are influenced by and influence the ice flow in this area, and how passive microseismic monitoring is a key tool for investigating this.

1.3 Background

1.3.1 Microseismic Monitoring on Ice

Microseismic monitoring is a technique derived from classical earthquake seismology and is the passive observation of small localised microseismic signals. In the case of ice these signals, known as icequakes, are produced by the fracture of ice or by the friction of ice against another surface, usually ice, till sediments or rock. Common causes are crevassing (e.g., *Mikesell et al.*, 2012), glacial calving (e.g., *Walter et al.*, 2012) and slip at the base and sides of a moving ice stream or glacier (e.g., *Anandakrishnan and Bentley*, 1993). It is the icequakes caused by basal motion that are most relevant to studying ice stream basal characteristics and dynamics. The energy released by basal icequakes radiates outwards from the source as compressional (P-wave) and shear (S-wave) signals, collectively known as body waves. These signals are too weak to be felt but can be recorded using seismometers and geophones which convert the ground motion produced by these waves into voltages. The P-wave signal is faster and arrives at the receiver (seismometer or geophone) first and the S-wave is slower, arriving sometime later. These signals can be inverted for source location and source mechanism to give spatial and temporal information about the active basal dynamics of a moving ice stream. The seismic waveform recorded at a receiver also contains information about the material it has travelled through. In the case of ice, the type of ice fabric present is of particular interest in relation to ice dynamics. A clear indication of the formation of a strong ice fabric (crystal preferred orientation fabric) is shear wave splitting (SWS), with two independent S-waves being seen at the receiver. More detail on this can be found in Section 1.3.2.

The first dedicated microseismic survey on ice was undertaken by *Neave and Savage* (1970) on the Athabasca Glacier in Canada, although natural glacial icequakes had been detected previously in the same area while undertaking active seismic surveying (*Roethlisberger*, 1955). *Neave and Savage* (1970) were hoping to observe evidence for faulting due to basal motion underneath the ice, but instead identified over 1000 icequakes thought to originate from crevasse opening in the marginal shear zones. It was not until 17 years later, in 1987, that passive microseismic monitoring was used to study an ice stream in Antarctica. The survey undertaken by *Blankenship et al.* (1987) was designed specifically to study "internal

stresses and basal sliding" (*Blankenship et al.*, 1987) on the fast moving (400-800 m a^{-1}) Whillans Ice Stream (formerly Ice Stream B) in West Antarctica (Figure 1.1). The study used high frequency three-component (vertical and two horizontal) seismometers designed to detect the, so far elusive, basal seismicity. *Blankenship et al.* (1987) succeeded in detecting a swarm of nine short-period icequakes that could be located to within tens of metres of the bed, although it was not clear whether the events originated within the ice, the subglacial sediments or the bedrock underneath. Significantly, they determined that the source of the events was consistent with low-angled thrust faulting in the ice flow direction. This was later confirmed by *Anandakrishnan and Bentley* (1993) who constructed fault plane solutions of the source of these events. It was also recognised that the detection of split S-wave signals was a good indication of seismic anisotropy in the ice, showing that microseismic signals could also be useful in investigating ice fabric within Antarctic ice streams. This study paved the way for the use of passive microseismics in studying basal dynamics and ice structure in Antarctic ice streams, and many studies have followed on from this.

The studies of *Anandakrishnan and Bentley* (1993) and *Anandakrishnan and Alley* (1994) built upon the microseismic studies of Whillans Ice Stream and the neighbouring, relatively slow moving (< 10 m a^{-1}) Kamb Ice Stream (formerly Ice Stream C). They concluded that in both cases icequakes were caused by slip on low angled basal thrust faults thought to be 'sticky spots' (*Alley*, 1993) of high friction subglacial material at the base of the ice stream that provided restraint to the driving stress of the overlying ice. *Anandakrishnan and Bentley* (1993) concluded that the icequakes were likely to originate from either the interface or the subglacial material, rather than from within the ice. They calculated that slip on these 'sticky spots' was responsible for only a tiny amount of the overall motion of the ice streams, although it accounted for several orders of magnitude more in the case of the slow moving Kamb Ice Stream. This led to a conclusion that the basal material underneath the Whillans and Kamb ice streams consists of a weak dilatant till interspersed with 'sticky spots' of high strength, high friction till. Many more and much larger 'sticky spots' are thought to exist underneath the slower moving Kamb Ice Stream, which provide a stronger restraint to ice stream flow. These studies provided the first direct evidence of ice stream motion over 'sticky spots' of stiff sediment, at a time when theories of ice stream basal dynamics were starting to concentrate on the idea that both basal sliding and bed deformation could happen in combination beneath ice streams (e.g., *Vaughan et al.*, 2003; *Alley*, 1993). In many of these

early studies the term 'till' is used to refer generally to subglacial sediments. Strictly the term 'till' refers to poorly sorted sediment that has been deposited by a glacier (*Paterson*, 1994). As the origin of subglacial sediments in these areas is unknown they may not be tills in the strictest sense. From here on-wards the term 'subglacial sediments' will be used to refer to subglacial sediments of unknown origin, even if they are referred to as 'tills' in the source text (e.g., *Anandakrishnan and Bentley*, 1993; *Alley*, 1993; *Anandakrishnan and Alley*, 1994).

Many studies of basal microseismicity on ice streams and glaciers have occurred in the intervening decades since these studies, and the information gained has become increasingly comprehensive and varied. Strong correlation between basal seismicity rates and tidal forcing on Kamb Ice Stream (*Anandakrishnan and Alley*, 1997) has led to theories of the transmission of stress from the grounding line through the subglacial material. Subglacial harmonic tremor signals, caused by water resonating in subglacial cracks and conduits, have been used to track subglacial water movement in Antarctica and Alaska (*Winberry et al.*, 2009; *West et al.*, 2010). These signals can be used to infer spatial and temporal characteristics of the subglacial hydrological system and link these to variations ice stream flow, for example, an increase in glacier surface velocity corresponding to an increase in resonant subglacial seismic events (*West et al.*, 2010).

Large long-period subglacial icequakes of magnitude (M_w) > 4 (not strictly microseisms) have been found to occur on Whillans Ice Stream in Antarctica (*Wiens et al.*, 2008; *Winberry et al.*, 2013), underneath areas of the ice streams that move by large scale stick-slip motion. It is thought that these large scale slips ($\sim$0.4 m in $\sim$30 min period, *Winberry et al.*, 2013) on Whillans Ice Stream are associated with tidal influence at the grounding line and possible changes in the pore pressure and strength of the underlying basal material. Repeated surveys on Whillans Ice Stream (*Winberry et al.*, 2014) have even shown them to vary over time with associated variations in ice stream velocity. *Pratt et al.* (2014) went on to use these events to infer basal material conditions in the grounding zone of Whillans Ice Stream. Similar large magnitude signals have been observed in Greenland (*Ekström et al.*, 2003; *Tsai and Ekström*, 2007; *Rial et al.*, 2009), which were originally thought to be caused by large scale stick-slip basal sliding but have since been shown to be the result of calving events (*Tsai et al.*, 2008; *Murray et al.*, 2015).

Microseismic studies on mountain glaciers have also yielded basal events thought to be related to stick-slip motion at the ice-bed interface. *Deichmann et al.* (2000) found seismicity near the base of Unteraargletscher, Switzerland and while the source mechanism was unknown, it was recognised that the events did not result purely from tensile cracking. *Stuart et al.* (2005) observed basal seismic events during a surge of Bakaninbreen, Svalbard. The events were located in the frozen 'cold based' area of the glacier downstream of the surge front, while there was a lack of basal events from the well lubricated 'warm based' areas upstream of the surge front, a possible analogy to the findings of *Anandakrishnan and Alley* (1994) in Antarctica. There have also been observations of stick-slip sliding of the ice caps on volcanoes (e.g., *Thelen et al.*, 2013) and of repeating stick-slip basal motion at discrete areas of the ice-bed interface of Glacier d'Argentière, France (*Helmstetter et al.*, 2015). Interestingly the conclusion by *Helmstetter et al.* (2015) indicated that it was "possible that the cumulated seismic slip due to the basal icequakes accounts for all of the glacier motion locally and temporarily", a contrast to the findings on Antarctic ice streams. In recent years extensive studies of the seismicity of Gornergletscher, Switzerland have been undertaken (*Walter et al.*, 2008, 2010, 2013) suggesting that tensile crack opening and closing by hydro-fracture at the base of the ice is the most likely source of basal seismicity.

Although the presence of shear wave splitting in basal microseismic data was recognised by *Blankenship et al.* (1987), the use of passive microseismics to study seismic anisotropy and the ice fabric that might produce this has been limited. Several studies have used active seismic data to study anisotropy, along with borehole profiling (e.g., *Gusmeroli et al.*, 2012) and ice core measurements (*Faria et al.*, 2014a). A preliminary study by *Harland et al.* (2013) using a 12-hour long section of the data set described in this dissertation, identified clear SWS of up to 6% with the fast S-wave direction perpendicular to the ice flow. *Walter et al.* (2015) have also suggested a method for monitoring changes in ice structure over time using changes in icequake phase velocity. A detailed discussion of seismic anisotropy in ice can be found in Section 1.3.2.

While Rutford Ice Stream has been extensively studied with a variety of geophysical methods (Section 1.4.2), there has been only one published microseismic study of basal conditions preceding the one described in this dissertation. The study of *Smith* (2006) was a preliminary study in the same area as the one described in this dissertation, it concluded that parts of the ice stream likely to be moving by basal sliding, identified from active seismic and RES studies

(*Smith*, 1997a,b; *Smith and Murray*, 2009; *King et al.*, 2009), showed levels of seismicity six times greater than those moving over a deforming bed. This conclusion was drawn from a simple count of the number of events detected at stations situated over the two different bed types and provided only weakly constrained locations of seismic events. The study of *Smith* (2006) was later used to compare basal microseismicity levels to ice stream surface velocity by *Adalgeirsdóttir et al.* (2008), who observed that in this area of Rutford Ice Stream the highest levels of basal seismicity correlated with spring tides, when the velocity is highest, and that there are often two peaks in both seismicity and velocity during a semi-diurnal tidal cycle.

The use of icequakes to study the basal conditions and dynamics of ice streams has provided great insights over the past ∼30 years, however, a key question that remains unanswered is the exact source and location of these signals: are they slip at the ice-bed interface, fracture of basal ice or faulting of sub-glacial material?

1.3.2 Ice Fabric

Glacial ice on Earth is formed of hexagonal ice crystals (Figure 1.3), a structure known as Ih ice (*Faria et al.*, 2014b). The Ih crystal structure is plastically anisotropic, deforming preferentially by slip (ice creep) on its basal plane, normal to the c-axis of the crystal (*Duval et al.*, 1983). This means that when stress is applied to bulk polycrystalline ice, such as the stresses induced by ice stream flow, the c-axes of many crystals will preferentially align forming an ice fabric, often referred to as a crystal preferred orientation (CPO) fabric.

When snow falls on the surface of an ice sheet the crystals are initially randomly orientated, giving a bulk isotropic fabric (Figure 1.4a). Over time the snow will be subject to compressive stress forming ice (typically at ice domes in the interior of ice sheets), and then subject to a variety of different stresses as it moves and flows. The type of ice fabric formed records the deformation history of that ice and will, in turn, affect the future response of that ice to the stresses induced by ice flow (*Alley*, 1988). Investigating the type of ice fabrics within an ice stream is essential to understanding the flow regime of that ice stream and predicting its future response to changing stresses.

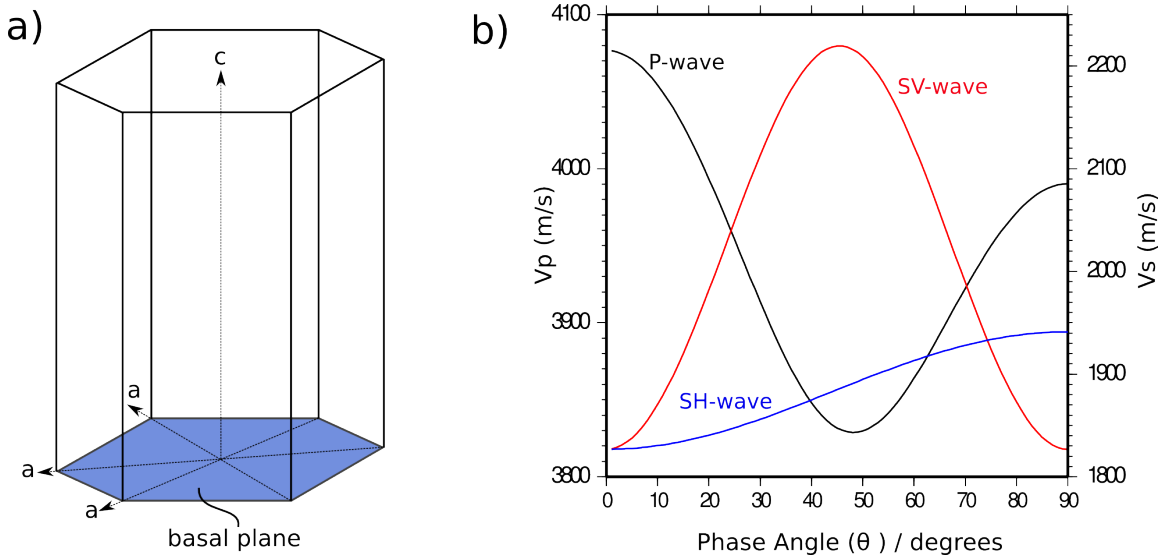

Figure 1.3: ***Ice crystal properties*** *a) Schematic of the structure of a single ice crystal, crystals deform preferentially on their basal plane (blue). The c-axis provides the major axis of symmetry for elastic anisotropy. b) Seismic wave propagation velocities through a single ice crystal (see Appendix A), 0° is along the c-axis. P-waves propagate fastest along the c-axis, SV waves at 45° to the c-axis and SH waves at 90° to the c-axis.*

Much work has been done predicting the type of fabric produced by different stress regimes and how these may be related to real world glaciological settings. Commonly found fabrics are given in Figure 1.4 along with a new category of fabric defined in this study the 'horizontal partial girdle' (Figure 1.4e). Pure uniaxial compression (Figure 1.4b), such as snow compressed into ice under gravity at ice domes, c-axes rotate towards the vertical (direction of applied compressive stress) forming a cluster around the vertical (*Alley*, 1988; *Azuma*, 1994), with an opening angle of ξ in the X_1 direction and θ in the X_2 direction, where $\xi = \theta$. This is known as a 'cluster fabric' (sometimes referred to as a cone in glaciology) and is a vertically transversely isotropic (VTI) fabric, meaning the anisotropy is symmetrical about the vertical axis but varies horizontally away from this axis. The extreme end members of this category are a vertical single maxima, where all c-axes are orientated vertically ($theta = \xi = 0°$) or an isotropic fabric ($\theta = \xi = 90°$). Pure uniaxial extension (Figure 1.4c) forms a 'thick girdle fabric' as c-axes rotate away from the extensional axis (*Alley*, 1988; *Azuma*, 1994). The girdle has an opening angle of ξ in the X_1 direction that defines the thickness of the girdle and an opening angle of $theta = 90°$ in the X_2 direction. The end members being all c-axes in a single vertical plane ($\xi = 0°$) or an isotropic fabric ($\xi = 90°$). In a glaciological setting this could be seen when ice is extended without a strong lateral or vertical confinement, for example, in a convergent flow environment at the onset of an ice stream, forming a vertical girdle perpendicular to the flow direction (i.e. the axis of extension). This fabric is horizontal transversely isotropic (HTI), with anisotropy being symmetrical about a horizontal axis.

A combination of extension and compression forms more complex stress regimes such as pure shear or simple shear. Pure shear is predicted by *Azuma* (1994) to be likely to occur in parallel flow environments, where the ice is longitudinally extended along the ice flow direction and compressed vertically (Figure 1.4d) forming a 'vertical partial girdle' (partial girdle of *Diez and Eisen*, 2015). A variation on this is an environment where ice is extended along the ice flow direction and confined laterally (Figure 1.4e), forming a 'horizontal partial girdle'. This type of fabric is not one commonly seen in ice cores and as far as I am aware it has not be defined prior to this study. I have defined it here (by a rotation of the partial girdle of *Diez and Eisen*, 2015) as it forms under a stress regime that is typical of an ice stream environment, such as Rutford Ice Stream.

Figure 1.4: ***Ice CPO fabrics properties****, figure adapted from Maurel et al. (2015) and Diez and Eisen (2015). The schematic for each fabric type shows the envelope of c-axis (blue area) and the projection of these c-axes on an upper hemisphere plot (blue dots on the horizontal plane). The angles ξ and θ are used to describe the opening angle of the c-axes envelopes in the X_1 and X_2 directions respectively. The type of stress regime under which these fabrics are commonly formed and the glaciological setting where this stress regime may be found are given. a) Isotropic b) Cluster c) Thick Girdle d) Vertical Partial Girdle e) Horizontal Partial Girdle*

Simple shear might be expected at the base and sides of an ice stream, forming a cluster or vertical single maxima (Figure 1.4b). From these predictions of ice fabric types *Azuma* (1994) derived a flow law for anisotropic ice and concluded that the inclusion of anisotropy in flow models is essential to effectively predict ice dynamics.

In a real world setting, such as an Antarctic ice stream, one would expect the ice fabric to be complex (*Alley*, 1988) as the ice will have undergone different types of stress regimes on its journey from the interior of Antarctica towards the outlet ice streams at the coast. It should also be noted that recrystallisation is thought to play a key role in high temperature, high shear environments (such as the base of a fast-flowing ice streams), potentially creating more complex fabrics still (*Budd and Jacka*, 1989).

In order to meaningfully include anisotropy in ice flow models (*Azuma*, 1994), observations of ice fabric types are needed. In situ measurement of ice fabric can be made by ice coring and borehole studies. The first Antarctic ice core was drilled by *Schytt* (1958) to a depth of 100 m and studies of the crystallography of the ice were made, noting changing CPO with depth. *Gow* (1967) recorded the first successful full ice core penetration of the inland Antarctic Ice Sheet at Byrd Station, drilling to 2164 m depth and breaking into the subglacial sediment beneath the ice. Between 900 - 1800 m into the core a clear CPO fabric had formed, with c-axes being orientated within 15° of the vertical. Below this it is thought that the crystals had melted and recrystallised due to high temperature and pressure, meaning the fabric structure was not clear (*Gow and Williamson*, 1976). This study set a new standard for deep ice coring and a great number of ice cores have been drilled in the intervening 40 years. A detailed and comprehensive review of the history of ice coring in Greenland and Antarctica is provided by *Faria et al.* (2014a,b).

The majority of drilling projects have been motivated by past climate studies, so they have been drilled at ridges and domes (*Faria et al.*, 2014a) and are not representative of the variety of ice flow regimes that might occur on an ice sheet. By analysing thin sections of these ice cores under co-polarised light the CPO can be observed at intervals within the ice core (e.g., *Durand et al.*, 2006); it can also be investigated by ultrasonic measurements through the core (*Kohnen and Gow*, 1979; *Anandakrishnan et al.*, 1994). Analysis of cores from ice dome sites confirms that strong vertical compression dominates, with vertical cluster and single maxima fabrics developing (e.g., *Azuma et al.*, 1999). Strong girdle fabrics were shown to develop in the middle sections of the NGRIP (*Wang et al.*, 2002) and Vostok (*Lipenkov et al.*, 1989) ice

cores, interpreted as evidence for extensional flow transverse to a ridge.

As well as being plastically anisotropic, ice crystals are also elastically anisotropic. This means the speed at which seismic waves travel through them will vary with direction. The c-axis provides the axis of symmetry for elastic anisotropy (*Harland et al.*, 2013) with the fastest P-wave velocities propagating along the c-axis and the slowest at $\sim 51^{\circ}$ to this (Figure 1.3b). Conversely for S-waves the slowest SV (vertically polarised, in the plane of propagation) wave is along the c-axis and the fastest at 45° to it. The SH (horizontally polarised, orthogonal to the plane of propagation) wave is less sensitive to variations in ice fabric (Figure 1.3b). A bulk polycrystaline ice fabric, made up of aligned ice crystals, will demonstrate a similar anisotropy to a single crystal, although somewhat weaker.

Sonic logging, a technique derived from the petrophysical industry, involves lowering a logger (transmitter and a number of receivers) down a borehole and continuously measuring the seismic velocity within the hole. It can be used to investigate continuous seismic velocity variations, which are indicative of ice fabric variations. The velocities of sound waves in ice are sensitive to changes in the temperature, pressure and ice fabric. The effects of temperature and pressure on seismic velocity can be corrected for (*Gusmeroli et al.*, 2012), allowing variations in seismic velocity as a function of ice fabric to be investigated. Borehole logging has the advantage of being both less labour intensive than obtaining and analysing ice cores and providing a continuous record, rather than discrete samples. The study of *Bentley* (1972) on the Byrd Station drill hole (*Gow*, 1967) used P-wave sonic logging to show that the technique was useful in identifying a continuous record of changing ice fabric. The P-wave velocities obtained were later compared to P-wave velocities measured in the Byrd ice core and showed good agreement (*Kohnen and Gow*, 1979). Borehole logging technology has moved on substantially in the past forty years and it is now possible to log both P-wave and S-wave velocities, an improvement that was suggested by *Bentley* (1972). However, very few studies have used this technique on ice, somewhat surprising given the relatively simple nature of ice as a material. The only published study (*Gusmeroli et al.*, 2012) details a framework for using full waveform P and SV wave sonic logging in ice to measure vertical single maximum fabrics. The study compares seismic velocity values derived from sonic logging and thin section analysis in the EPICA Dome C borehole, East Antarctica. Crucially *Gusmeroli et al.* (2012) conclude that the technique provides the "possibility to determine the variation of rheology with depth which is valuable for ice sheet modelling and ice core interpretation".

These techniques give detailed micro-scale information but over a very small spatial area and are logistically intensive to implement. It is particularly challenging to perform drilling in a dynamic ice environment, such as fast moving ice streams, and hence the majority of direct observations on ice fabric in Antarctica are towards the interior of the ice sheet (*Horgan et al.*, 2011). Seismic reflection, refraction and radio echo sounding (RES) techniques can be used to investigate a much wider geographical area, although they come with their own disadvantages over ice core and borehole studies, with lower resolution and a greater degree of interpretation needed. Nevertheless, where the macroscopic anisotropy measurements they yield can be related to microscopic ice fabrics, they provide an effective method of investigation. One of the best known geophysical observations of the effect of anisotropic ice fabrics on ice flow are Raymond bumps, first described by *Raymond* (1983). The stratigraphy of ice directly underneath an ice divide is arched upwards due to the fact that the ice deforms more easily on the flanks of the divide, where deviatoric stresses are higher. These features have been observed in radar-grams from RES surveying (e.g., *Vaughan et al.*, 1999; *Drews et al.*, 2013) and have been reproduced by modelling rheologically anisotropic ice flow (*Martín et al.*, 2009; *Pettit et al.*, 2007), demonstrating the importance of real world observations of anisotropy in improving ice flow models. RES data can also be used to view reflections due to changing CPO fabric with depth. Several studies (*Matsuoka et al.*, 2003; *Fujita et al.*, 2006; *Eisen et al.*, 2007; *Matsuoka et al.*, 2012) have developed robust methods of distinguishing reflections due to changing CPO from reflections due to changing dielectric permittivity by using multiple polarisations of radar wave. However, they cannot give specific information on the CPO fabric types.

As seismic wave velocities are so sensitive to anisotropy in ice, it would follow that seismic methods can be used to investigate types of CPO fabric. *Bentley* (1971) conducted an extensive set of of seismic reflection and refraction experiments over fourteen different locations in Antarctica, recognising strong indicators of anisotropy in the travel-times of seismic waves at all locations. For example, seismic P-wave and S-wave speeds were found that were extraordinarily high (up to 100 m s^{-1} higher than expected for both wave types) and out of the range that could be explained by temperature variations. The evidence suggested that anisotropic ice extends throughout 85% of the ice column. Although the exact fabric type could not be determined this highlighted a significant implication for ice sheet models. Wide angle reflection studies by *Blankenship et al.* (1987) later built upon this, analysing

seismic reflections data from Dome C and fitting the observed travel-times to different cone models of VTI anisotropic fabrics. Analysis of the nature of englacial seismic reflections, as well as travel-times, has also been used to detect changing CPO with depth in a number of ice streams (*Horgan et al.*, 2008, 2011) and ice domes (*Hofstede et al.*, 2013), although conclusions about the type of fabric causing the reflections could not be made without ice core evidence for comparison. A study of shear wave anisotropy using three component active seismic data from Whillans Ice Stream (*Picotti et al.*, 2015) has recently suggested that below the firn-ice transition at 65 m, the ice stream consists of a VTI ice fabric throughout the ice column. This suggests that in this area of Whillans Ice Stream both basal shear stresses and deviatoric stresses are low, indicative of an environment dominated by vertical compression and transversely divergent or parallel flow. *Picotti et al.* (2015) suggested that this finding is typical of large Antarctic ice streams, of which Rutford Ice Stream is one.

A recent and significant development has been to use full waveform inversion to investigate anisotropy in seismic and radar data (*Diez et al.*, 2015; *Diez and Eisen*, 2015). Unlike earlier studies the work of *Diez et al.* (2015) and *Diez and Eisen* (2015) do not reduce the data to travel-times or reflection characteristics, but rather look at the effect anisotropic fabrics have on the entire seismic wavefield. *Diez and Eisen* (2015) were able to use CPO eigenvalues (used to describe CPO distributions in ice cores) to derive the elasticity tensor for different CPO types. From the elasticity tensor they derive seismic velocities and reflection coefficients for P, SH and SV waves. Crucially, they were able to do this for both cone and girdle fabrics, whereas many earlier studies had focused on cone fabrics only. The method developed by *Diez and Eisen* (2015) was then applied to compare the P-wave velocities calculated from the EPICA Dronning Maud Land (EDML) core to vertical seismic profile (VSP) and seismic reflection data as well as RES reflections recorded at the EDML ice core site (*Diez et al.*, 2015). The combined results and interpretation are robust for the differing fabric types and show that the full waveform method can effectively predict seismic wave propagation in a large range of anisotropic ice fabrics. *Diez et al.* (2015) warn that the choice of elasticity tensor for converting CPO eigenvalues to seismic velocities has a strong influence on the results and must be investigated carefully. Although they conclude that "there is still a need for very high resolution measurement with fabric analysers or ultrasonic logging on ice cores or in boreholes to fully understand the formation and distribution of crystal fabric and its interaction", this study has provided key methods and results in the understanding of seismic

wave propagation in anisotropic ice.

Shear wave splitting has often been observed in seismic data from Antarctica, however, studies specifically analysing this are very scarce. A study was undertaken on a small section of the icequake data from Rutford Ice Stream presented in this dissertation (*Harland et al.*, 2013), and is the first published study I am aware of to specifically analyse SWS in ice. The advantage of using icequake data over active source reflection and refraction data for shear wave studies is that icequakes generate strong S-waves, whereas generating S-waves in seismic reflection and refraction studies is difficult. Techniques for analysing SWS in microseismic data are well established and have been used extensively in a variety of geological settings, with effective automated methods for analysing large datasets being developed (*Wuestefeld et al.*, 2010).

When a shear wave encounters an anisotropic medium it is split into two mutually orthogonal S-waves, polarised along the anisotropic axis of symmetry (*Savage*, 1999) arriving at a receiver separated by a delay time, which is proportional to the strength of the anisotropy (Figure 1.5). Measurements of the delay time (δt) and the angle of the fastest shear wave (ϕ) can be used to investigate the elastic anisotropy characteristics of the ice an S-wave has travelled through. From these measurements the ice CPO fabric characteristics can be determined.

In a single ice crystal the direction of minimum SWS is along the c-axis and the direction of maximum SWS is at 50° to that axis (*Harland et al.*, 2013). The study of *Harland et al.* (2013) concluded that up to 6% anisotropy was present with the majority of the fast S-waves being polarised perpendicular to the flow direction. They inverted for several ice fabric models, concluding that a combination fabric with both VTI and HTI components best fitted the observed splitting measurements. It was thought that this could indicate a combination of vertical cluster and girdle fabrics at different depths within the ice stream, or a fabric that was largely a vertical cluster fabric with vertically aligned cracks perpendicular to the flow direction. This suggests that the ice fabric in Rutford Ice Stream could be much more complex than the bulk VTI fabric thought to make up Whillans Ice Stream (*Picotti et al.*, 2015).

Using SWS to identify elastic anisotropy and therefore ice fabric variations in ice provides both spatial and temporal ice fabric information over a wide geographical area. It is also logistically much easier to implement than drilling or borehole studies, especially in an en-

vironment such as a fast moving ice stream. As can be seen from the review of different techniques here, it would be ideal to have a combination of very fine scale borehole measurements and wider scale seismic measurements to allow the results of each to be compared and tied to each other.

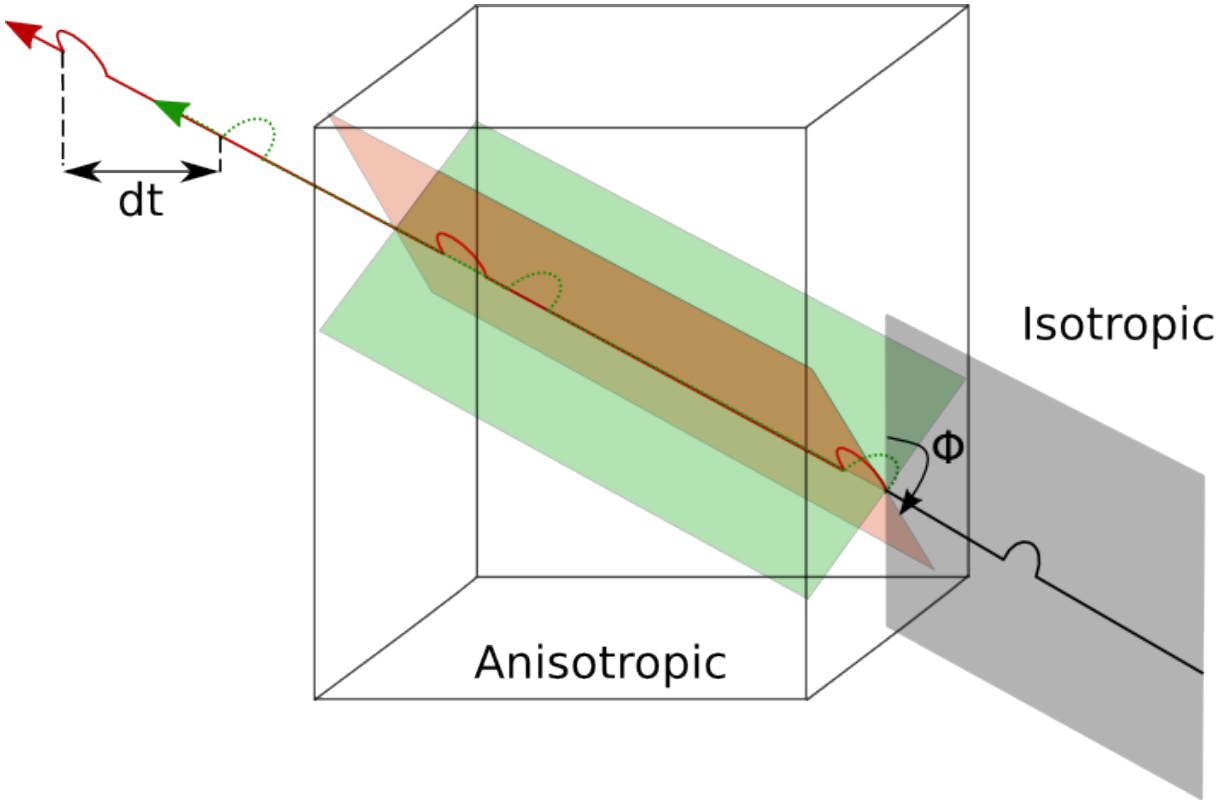

Figure 1.5: ***A cartoon of the mechanism of shear wave splitting*** *adapted from Crampin (1981). Measurements of the delay time (δ t) and the angle of the fastest shear wave (ϕ) can be used to investigate the elastic anisotropy characteristics of the ice fabric an S-wave has travelled through.*

1.4 Rutford Ice Stream

1.4.1 Field Site

Rutford Ice Stream is a fast-flowing ice stream located in West Antarctica (Figure 1.6). The ice stream drains ∼48,000 km^2 of WAIS into the Ronne Ice Shelf (*Joughin and Bamber*, 2005; *Doake et al.*, 2001). The area covered by the passive seismic survey used in this study is approximately 40 km upstream from the grounding line (Figure 1.6), the location where the ice stream becomes a floating ice shelf. In the survey region the ice stream is around 25 km wide and occupies an asymmetric trough which is deeper on the western side, where it is bounded by the Ellsworth Mountains and shallower to the East, bounded by the Fletcher Promontory (*Smith*, 1997a). There are clearly crevassed shear margins delineating the edges of the ice stream. The ice is ∼2.2 km thick with around 1.9 km of this lying below sea level. The average ice-flow speed is 377.3 m a^{-1} (*Murray et al.*, 2007) which is thought to be steady showing no significant long-term changes (*Gudmundsson and Jenkins*, 2009). The basal shear stress in this area is low around 35 kPa (*Vaughan et al.*, 2003); given this and the fast flow speed it is thought likely that the ice near the bed is at the pressure-melting point (*Smith and Murray*, 2009) and is well lubricated.

1.4.2 Summary of Previous Work in the Area

Rutford Ice Stream has been extensively investigated, with more than 35 years of in situ measurements being made along the ice stream and several studies concentrated on the area covered by this dissertation (Figure 1.6). The earliest field studies on Rutford Ice Stream began in the 1978-1979 field season and concentrated on the grounding line region (*Stephenson et al.*, 1979; *Stephenson and Doake*, 1982; *Stephenson*, 1984), as this zone of transition between grounded and floating ice was thought to be key to understanding the response of the ice stream to changes in climate. A campaign to determine the surface topography by optical levelling and ice thickness data from ground and airborne RES surveys was undertaken around the likely area of the grounding line between 1978 and 1981. By comparing the values of surface elevation and ice thickness it was possible to determine where the ice was in hydrostatic equilibrium and thus floating (*Stephenson and Doake*, 1982).

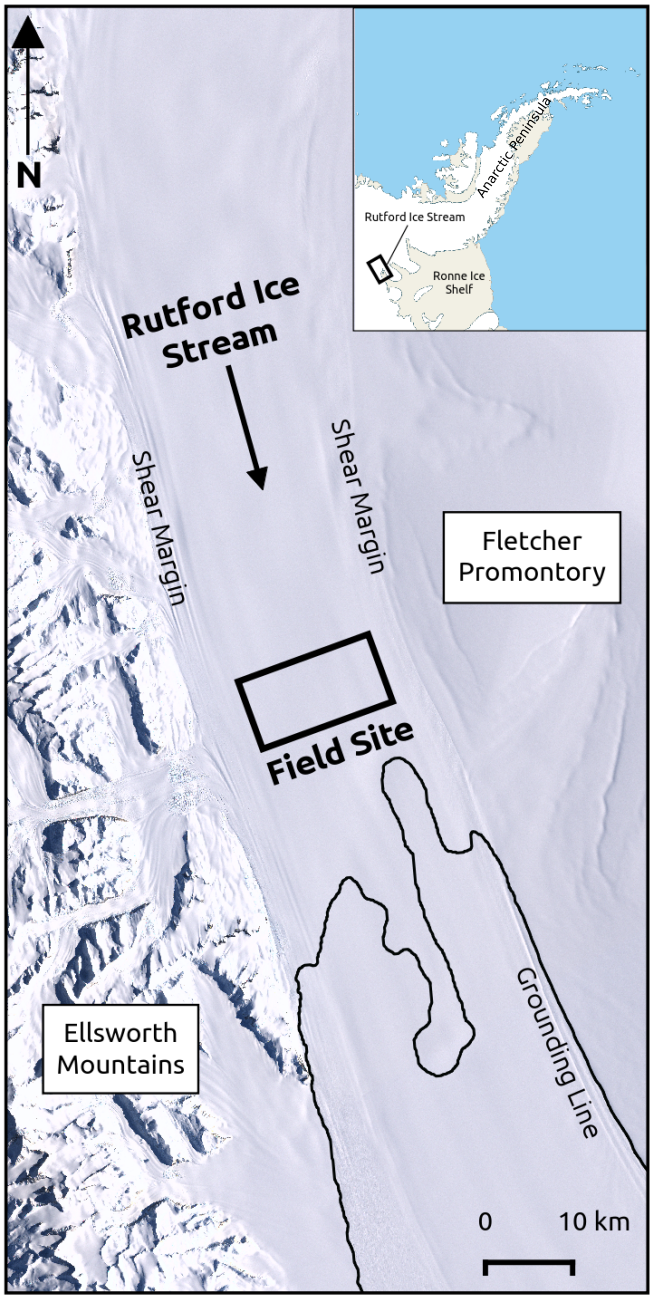

Figure 1.6: ***Location of study site on Rutford Ice Stream. Inset:*** *Rutford Ice Stream is located at the base of the Antarctica Peninsula, flowing into the Ronne Ice Shelf.* ***Main Image:*** *LIMA (Landsat Image Mosaic of Antarctica) image of the surface of Rutford Ice Stream. Study location is approximately 40 km upstream from the grounding line (black line - from the Antarctic Digital Database, coastline data set, Version 6.0.0 27/04/2012), where the ice stream is around 25 km wide and 2.2 km thick. Rutford Ice Stream is bounded by the Ellsworth Mountains to the West and the Fletcher Promontory to the East, the edges of the ice stream are delineated by clear shear margins.*

The basal profile of the ice stream in this region consists of "thick fingers of ice running parallel to the flow" (*Stephenson and Doake*, 1982), suggesting a complex basal morphology near the grounding line. In order to determine the location of the grounding line more accurately, tiltmeters (*Stephenson et al.*, 1979) were used to measure the flexing of the ice as the ice shelf was perturbed by the tide. These values were fitted to an elastic beam model to determine the probable position of the grounding line. Together these studies concluded that the grounding line was a complex asymmetric shape, being further upstream on the western side than the East (*Stephenson*, 1984) and being marked in the centre of the ice stream by a prominent surface knoll. These studies also yielded longitudinal and transverse strain rates and velocity profiles (*Stephenson and Doake*, 1982), showing that this region of the ice is largely in a compressive regime as the ice stream flows into the ice shelf. These early studies were the start of an on-going campaign to investigate the dynamics of Rutford Ice Stream and paved the way for many investigations to come.

The surface network of survey stakes to determine ice velocity and strain rates was extended upstream of the study of *Stephenson and Doake* (1982) during the 84/85 and 85/86 field seasons to produce a ∼100 km long network along the centre of the ice stream, with several transverse profiles (*Frolich et al.*, 1987; *Doake et al.*, 1987). These studies showed that the bed of much of Rutford Ice Stream is asymmetric, agreeing with the findings of an asymmetric grounding line, with a deeper bed and thicker ice to the West, where the ice stream borders the Ellsworth Mountains. Not unexpectedly, this is also the area of fastest ice surface velocity (*Frolich and Doake*, 1988). Analysis of the lateral and transverse velocity variations showed that shear margins at either side of the ice stream extend for about 10 km but that the central portion of the ice stream is largely unaffected by side wall shear. Therefore, in the central region of Rutford Ice Stream the ice flow must be balanced by a basal shear stress of around 40 kPa to balance a driving stress of the same amount (*Frolich and Doake*, 1988). Later estimates show this to be nearer to 35 kPa (*Vaughan et al.*, 2003).

Studies of ice stream velocity and tidal influence have been conducted more recently using high precision GPS data. They show that there is a strong fortnightly variation in the flow of Rutford Ice Stream, of around ±10%, modulated by tidal forcing on the ice shelf (*Gudmundsson*, 2006; *Murray et al.*, 2007). This variation is transmitted upstream from the grounding line, modulating the surface velocity in the study area presented in this paper. Combined studies using the surface stake network and later GPS datasets, jointly covering

~25 years, show no long term change in the ice stream velocity (*Gudmundsson and Jenkins*, 2009). Although there was evidence of annual variation over a particular 2-year recording period (*Murray et al.*, 2007), it is now thought that this was related to small seasonal variations during the period of data collection (*Gudmundsson and Jenkins*, 2009), possibly long period tides, and is not a long term variation in flow. Modelling studies conducted to relate the observed surface velocity variations to tidal forcing transmitted upstream from the grounding line have shown there is a non-linear response of Rutford Ice Stream to the known tidal cycle (*Gudmundsson*, 2007; *King et al.*, 2010), this can be explained using a non-linear viscous sliding law (*Gudmundsson*, 2011). A recent study (*Rosier et al.*, 2014) using a 3-D visco-elastic full Stokes model has demonstrated this in a more realistic 3-D ice stream setting. Previous flow line models (*Gudmundsson*, 2007; *King et al.*, 2010) did not account for transverse aspects of the tidal forcing, such as side drag. *Rosier et al.* (2014) showed that when the effects of lateral drag and grounding line migration are included in the model, tidal forcing on Rutford Ice Stream can still be explained by a non-linear basal sliding law, affirming this as a key feature of the flow of Rutford Ice Stream. *Adalgeirsdóttir et al.* (2008) suggested there was a relationship between the variation in ice stream velocity and basal seismicity levels, implying that the tidal forcing causes significant variation in the basal characteristics of the ice stream with implications for the flow dynamics of Rutford Ice Stream.

The majority of Rutford Ice Stream is covered by satellite imagery and measurements, and Landsat images have been used to identify surface and flow features in this area since the 1970s (*Doake et al.*, 1987). For example, two prominent surface knolls indicative of corresponding bedrock features can be seen (Figure 1.7). The furthest downstream knoll was identified by *Stephenson and Doake* (1982) as corresponding with a pinning point at the grounding line and the surface knoll 30 km upstream of this (*Frolich et al.*, 1987) corresponds to a bedrock knoll with around 500 m vertical relief, identified from RES data (*Frolich and Doake*, 1988). Satellite interferometry (Figure 1.7) has also improved knowledge of the location of the grounding line and its migration over time as well as suggesting that regions of the downstream part of Rutford Ice Stream are partially grounded (*Rignot*, 1998).

Investigations of basal conditions on Rutford Ice Stream began in 1991 with high resolution seismic surveys (*Smith*, 1994) being conducted in the region described in this dissertation, just upstream of the upstream knoll (Figure 1.8). This area was chosen for investigating

basal dynamics as it was thought to be the area where a deforming sediment bed was most likely to exist (*Smith*, 1997a). Subglacial sediment deformation had been shown to be a significant factor in controlling the flow of Whillans Ice Stream (*Blankenship et al.*, 1986; *Atre and Bentley*, 1993, 1994; *Engelhardt et al.*, 1990) and therefore investigating the properties of sediment underneath Rutford Ice Stream was thought to be an important step to understanding its flow dynamics. A total of nine separate seismic lines were collected between 1991 and 2005 (*Smith and Murray*, 2009), with one of these being repeated to monitor changing basal conditions (*Smith et al.*, 2007).

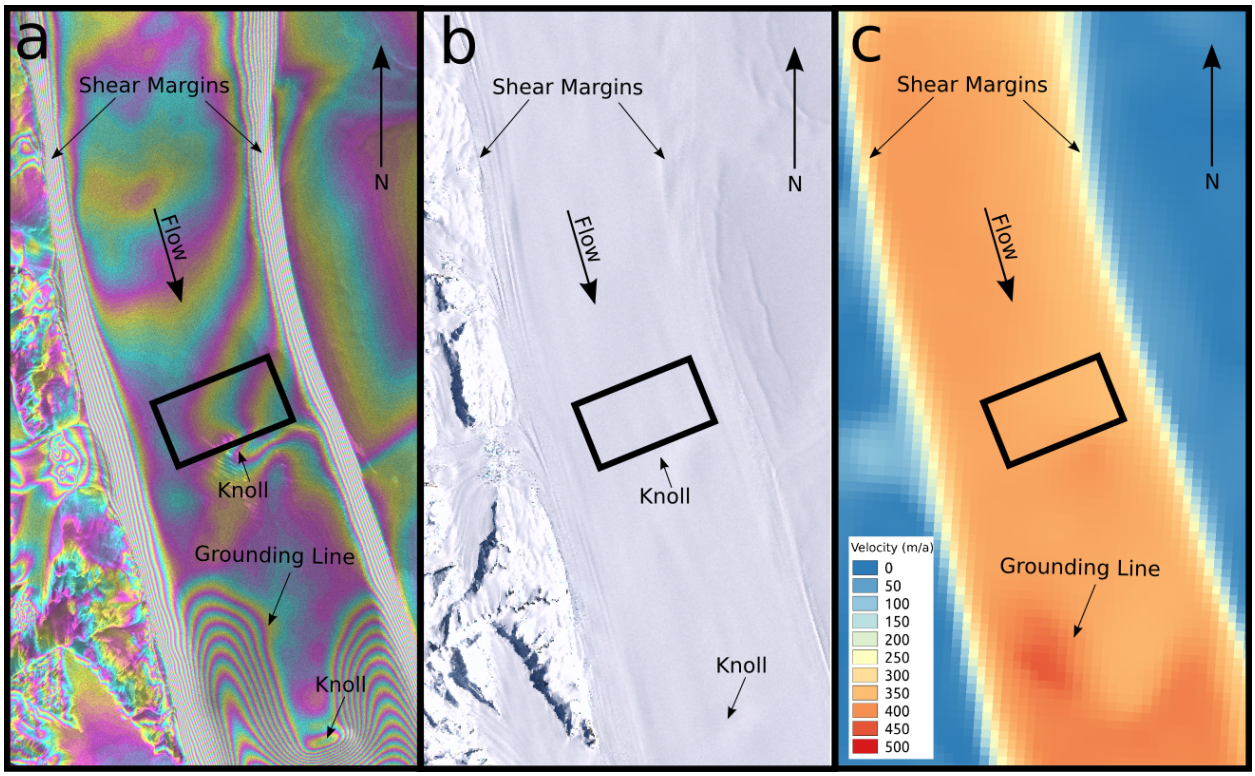

Figure 1.7: ***Rutford Ice Stream satellite derived observations.*** *Survey area is indicated by box, ice stream flow is down the page. a) Interferometric synthetic aperture radar (InSAR) image (H. Pritchard, personal communication) derived from European Remote-sensing Satellite (ERS) tandem mission images, frames 5463 and 5481 (ERS-1, 11^{t}h November 1995; ERS-2, 12^{t}h November 1995). The image gives an indication of surface deformation allowing the grounding line, shear margins and surface knolls to be identified. b) Landsat Image Mosaic of Antarctica (LIMA) image showing surface knolls and shear margins. c) Ice stream surface velocity from satellite measurement (Rignot et al., 2011), close up of Rutford Ice Stream from data shown in Figure 1.2.*

The first seismic line collected (Figure 1.8 - C1 line) confirmed that the bed topography was as expected from RES studies, with a central high flanked by troughs. There was a significant bump on the top of the central high, approximately 400 m wide by 50m high, termed 'the bump' (*Smith*, 1997a). The seismic reflection data were used to derive the reflection coefficient of the ice-bed interface, from which the acoustic impedance (the product of seismic velocity and density) of the bed could be determined, assuming the acoustic impedance of the ice did not vary significantly along the seismic line. Wide angle surveys were conducted across the centre of the line, with long enough data records to record the ice-bed interface reflection and its first multiple (seismic energy that has reflected from the ice-bed interface twice, with a reflection off the ice-air interface in between). Near offset traces from these wide angle records were used to calibrate the reflection coefficient of the ice- bed interface at this central point, using the reduction in amplitude between the primary ice-bed interface reflection and the first multiple. The seismic velocity profile of the ice was calculated using shallow refraction surveys in the firn layers (approximately top 100 m) and below this it was extrapolated using the relationship between ice temperature and seismic velocity (*Kohnen*, 1974). The base of Rutford Ice Stream in this area was found to be made of varying sediments, rather than bedrock. Taking the known relationship between changing acoustic impedance of sediments with changing porosities (*Atre and Bentley*, 1993), *Smith* (1997a) was able to distinguish between two different classes of sediment. High porosity sediments, which are thought to occur due to deformation (porosity >0.4) and hence represent a region of the ice-bed interface that is likely to accommodate ice stream motion by sediment deformation, and lodged sediment (porosity ≤ 0.3) which is non-deforming and thought to accommodate ice stream motion by basal sliding. 'The bump' is thought to be a drumlin of deforming sediments on top of the lodged sediment area.

Repeated seismic surveys over the C1 line (Figure 1.8) show both the rapid erosion of sediments from the bed in this region (6 m over a six-year period) and the formation of a drumlin-like feature of high porosity sediment (over a seven-year period) sitting on top of a lodged sediment area, much like 'the bump', but smaller in dimensions (*Smith et al.*, 2007). These were the first known observations of active drumlin formation under a contemporary ice stream and demonstrated the ability of an ice stream to transport and reorganise sediments over a relatively rapid time period of several years.

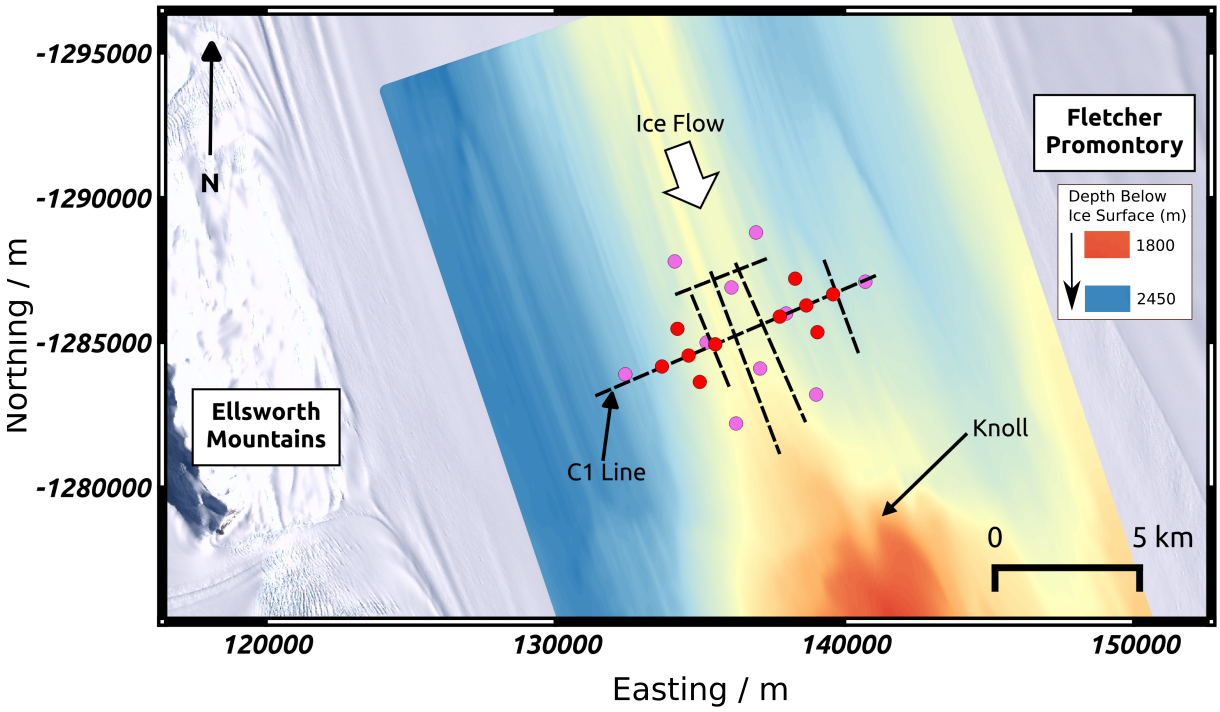

Figure 1.8: ***Map of previous studies on Rutford Ice Stream.*** *Map projection is Antarctic Polar Stereographic, standard parallel -71°S. Seismic lines used to make a 3-D basal interpretation by Smith and Murray (2009) are shown as dashed lines. Passive seismic stations from preliminary study of Smith (2006) are shown in purple and stations from the study described in this dissertation are shown in red. The coloured underlay is the RES survey described by King et al. (2009) showing the bed topography features, red colours are high bed topography and blue colours low. The bed knoll that corresponds to a surface knoll (see Figure 1.7) is shown.*

Bringing together all the seismic surveys in this area allowed a robust 3D interpretation of basal conditions in the area to be made (*Smith and Murray*, 2009), mapping areas of high-porosity deforming sediment and lower porosity lodged sediment (Figure 1.9) that coexist underneath Rutford Ice Stream. This interpretation was supported by a preliminary passive seismic study (*Smith*, 2006) that found seismicity levels were 6 times greater over areas interpreted as lodged sediment, where basal sliding was likely to occur, although no precise locations for the seismic events were determined. Seismic reflection surveys from further upstream showed this variety of bed characteristics underlying Rutford Ice Stream continues (*Smith*, 1997b). Many drumlin like features, thought to be mega-scale glacial lineations (MSGLs), were identified running roughly along the flow direction (deviating by up to 20°

from the flow direction), suggesting that the environment underneath Rutford Ice Stream is similar to that found in many palaeo-ice stream regions. It was found that there is likely to be a clear boundary between deforming sediment (upstream) and lodged sediment (downstream) in this area of Rutford Ice Stream (*Smith and Murray*, 2009). There is also some indication that there are seismic reflections up to 70 m below the bed, that could be from a layer representing the base of the deformable (but not actively deforming) sediments. Comparison between coincident seismic reflection and airborne RES data (*Murray et al.*, 2008) indicated that there may be channelised or canalised flow of water in deforming sediment regions and water filled cavities in the lodged sediment regions, improving our understanding of how the hydrology at the base of Rutford Ice Stream is linked to the sediment types, and how this may enable both sediment deformation and basal sliding to occur.

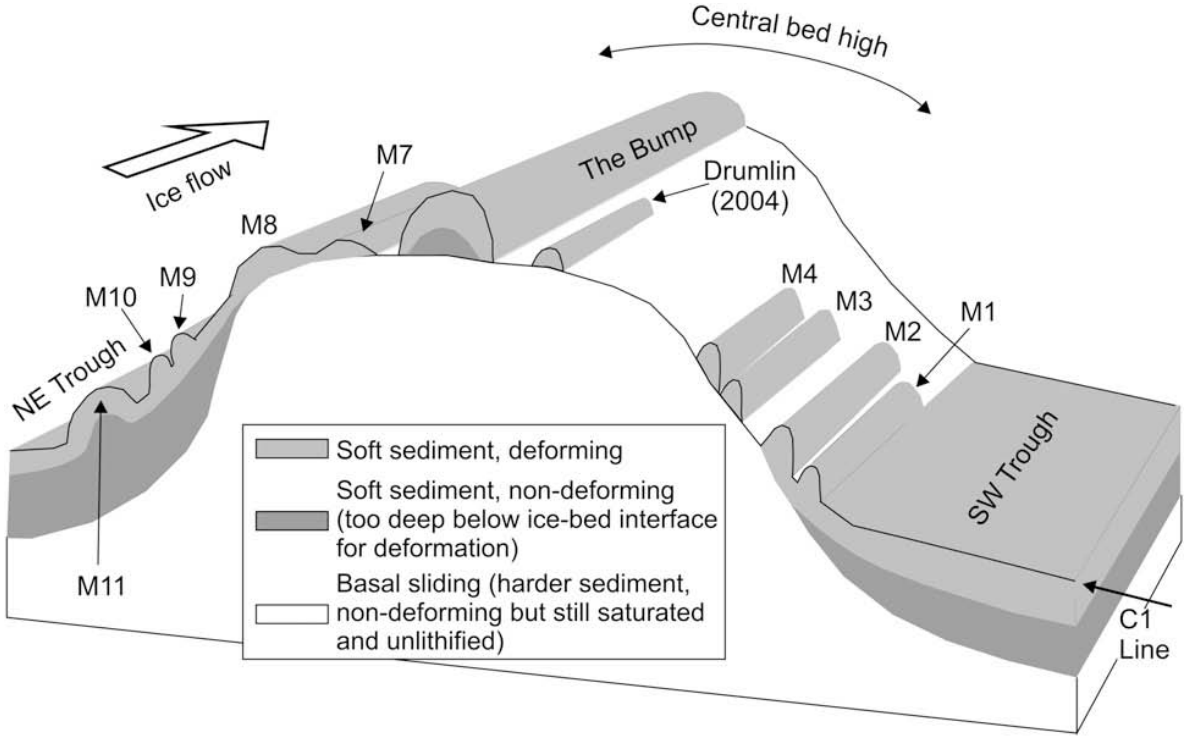

Figure 1.9: ***Schematic interpretation of the bed of Rutford Ice Stream (Figure taken from Smith and Murray (2009)).*** *View is looking down the ice flow direction, interpreted basal conditions are marked and seismic line C1 is shown for orientation. 'The bump' feature and the drumlin (Drumlin 2004) that formed between repeated surveys on the C1 line are shown (Smith et al., 2007) as well as 11 other MSGL type features.*

An extensive ground based RES grid (Figure 1.8) surveyed over this area (*King et al.*, 2009) extended and complemented this interpretation, suggesting that there is free water, several millimetres in thickness, in the areas of the bed where dilatant sediment is pinching out, possibly due to dewatering of sediment at the transition between stiff and dilatant sediments. This RES survey also extended the 3-D seismic interpretation of basal conditions, showing a pattern of many drumlin like features, some longer than 18 km, at the bed of Rutford Ice Stream.

It can be seen that while there is extensive knowledge of the basal environment underneath Rutford Ice Stream, there are still gaps in the understanding of how the movement of the overlying ice is accommodated, and there is little knowledge of the ice rheology and fabric in this area. Seismic reflection and RES techniques allow high resolution imaging of the basal environment, but do not provide any direct evidence of the process by which the movement of Rutford Ice Stream is facilitated and how this may vary temporally and spatially. The passive microseismic data presented in this dissertation is centred on the location of the original C1 line (Figure 1.8) and so can be directly compared and contrasted with the wealth of previous geophysical findings and interpretations in this area, to add to and improve knowledge of the dynamic basal environment and ice fabric in this region of Rutford Ice Stream.

Chapter 2

Data Set and Methods

2.1 Data Acquisition

Ten three-component geophones were deployed over a 34-day period during the austral summer of 2008/09. Geophones were orientated with the horizontal components pointing in the direction of flow (Y) and across the flow (X), Figure 2.1. They were buried around 1 m below the surface to ensure good coupling and to reduce environmental noise (Figure 2.2). The recording stations were configured into two adjacent cross arrays, with 1 km spacing between the central station in each array and each of the other stations (Figure 2.1). The arrays were positioned over areas of the bed that have been previously interpreted as having contrasting bed types (see Section 1.4.2). Array 1 (West) was located over an area with an inferred low-porosity ($\leq$0.3), consolidated basal sediment, where motion is primarily by basal sliding. Array 2 (East) was over an area with an inferred high-porosity (>0.4) dilatant sediment which deforms pervasively. Stations 2, 4, 5, 6, 7 and 10 were situated along the previously surveyed C1 active seismic line (see Figure 1.8). A dual-frequency GPS receiver was co-located with the centre of Array 1 and is indicated by a blue triangle on Figure 2.1.

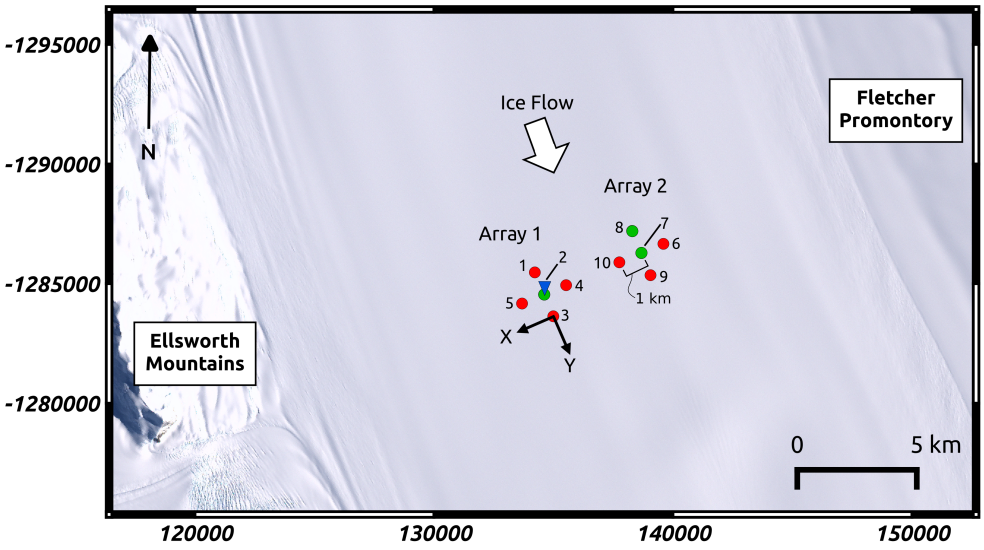

Figure 2.1: ***Survey configuration on Rutford Ice Stream.*** *Background to figure is the Landsat Image Mosaic of Antarctica (LIMA), projection is South Pole Stereographic. Seismic stations (circles) are approximately 40 km upstream from the grounding line. Geophones were orientated with the horizontal components pointing in the direction of flow (Y) and across the flow (X). Three stations are REFTEK RT-130 data loggers (green) and seven stations are ISSI SAQS data loggers (red). Stations are configured into two cross arrays situated over areas previously identified as having contrasting bed types from active seismic surveying. Array 1 (West) lies above a more solid 'sliding' bed and Array 2 (East) is over a 'deforming' bed (see Figure 1.8). A kinematic GPS station (blue triangle) is co-located with the center of Array 1.*

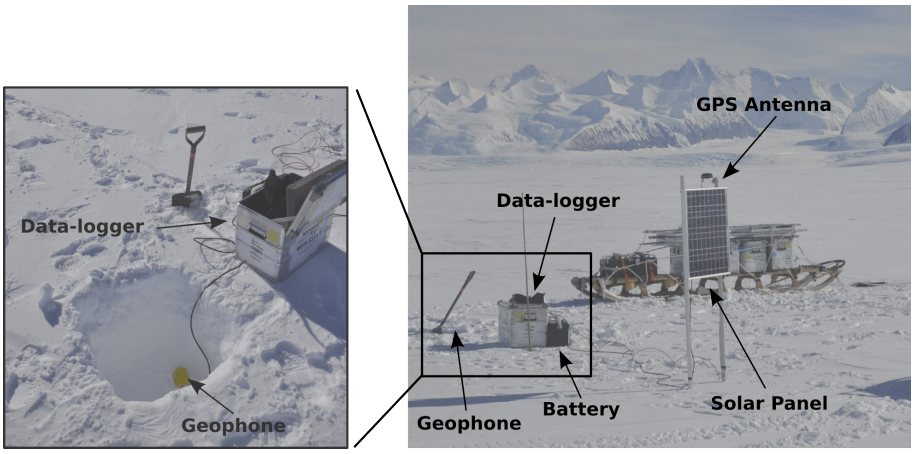

Figure 2.2: ***Photo: Seismic station configuration on Rutford Ice Stream (photo credit: A.M. Smith).*** *The geophone is buried 1 m below the surface to ensure good coupling (pit was later back-filled). The geophone is connected to a data logger, a battery, solar panel and GPS.*

Each geophone (4.5 Hz GS-11D) was connected to a data logger, a battery, solar panel and GPS antenna to ensure the relative timing on each station was synchronised (Figure 2.2). Two types of data logger were used, 3 x REFTEK RT-130 and 7 x ISSI SAQS. The type of data logger used for each station is indicated in Figure 2.1 by the station colour. All data loggers were sampling at 1000 samples per second.

2.2 Data Overview

Data were recorded over a 34-day period, between 1^{st} January 2009 and the 3^{rd} February 2009. Due to the time taken to install each station it was not until the 3^{rd} January that all stations were recording. For the purposes of this study the 32-day period over which all stations were installed and running (3^{rd} January 2009 - 3^{rd} February 2009) is used. During this 32-day period there were problems with excessive power consumption (*Pritchard et al.*, 2009) at some of the ISSI SAQS stations: 1, 4, 6 and 10 and a failed solar panel regulator on station 9, which led to data dropouts on these stations. Stations 2, 3, 5, 7 and 8 ran throughout the survey period without power issues, although a day of data was lost due to a corrupted flash card on station 8. The areas of data drop out can be identified by performing a basic seismic event count using a short-term average versus long-term average (STA/LTA) algorithm 'ms_picker' (SEIS-UK geophysical equipment facility, *Nippress et al.*, 2010). An STA:LTA ratio of 1:30 (with an STA window length of 0.01 seconds) was found to be optimal for this data set through testing on a sub-set of data, the STA/LTA algorithm was run on the full data record for each individual station (Figure 2.3). The areas highlighted in pink (Figure 2.3) identify the data drop outs and the area in grey highlights the section of corrupted data on station 8. The seismic waveforms in each of these periods were also manually checked to verify that they are true areas data drop out.

Overall, there were 16 out of 32 days on which all stations were active, on 23 out of 32 days at least 9 stations were active and on 27 out of 32 days at least 7 stations were active. This allows good detection and location of microseismic events that occur during these 27 days. Between the 14^{th} January and the 16^{th} January, 5 stations were inactive due to power issues. It may be difficult to identify and locate events in this period, particularly smaller amplitude events that are localised to Array 2, as 3 of the 5 stations in this array were inactive. With 5 stations active across both arrays it is still possible to locate events that produce high amplitude arrivals which can be identified across both arrays. .

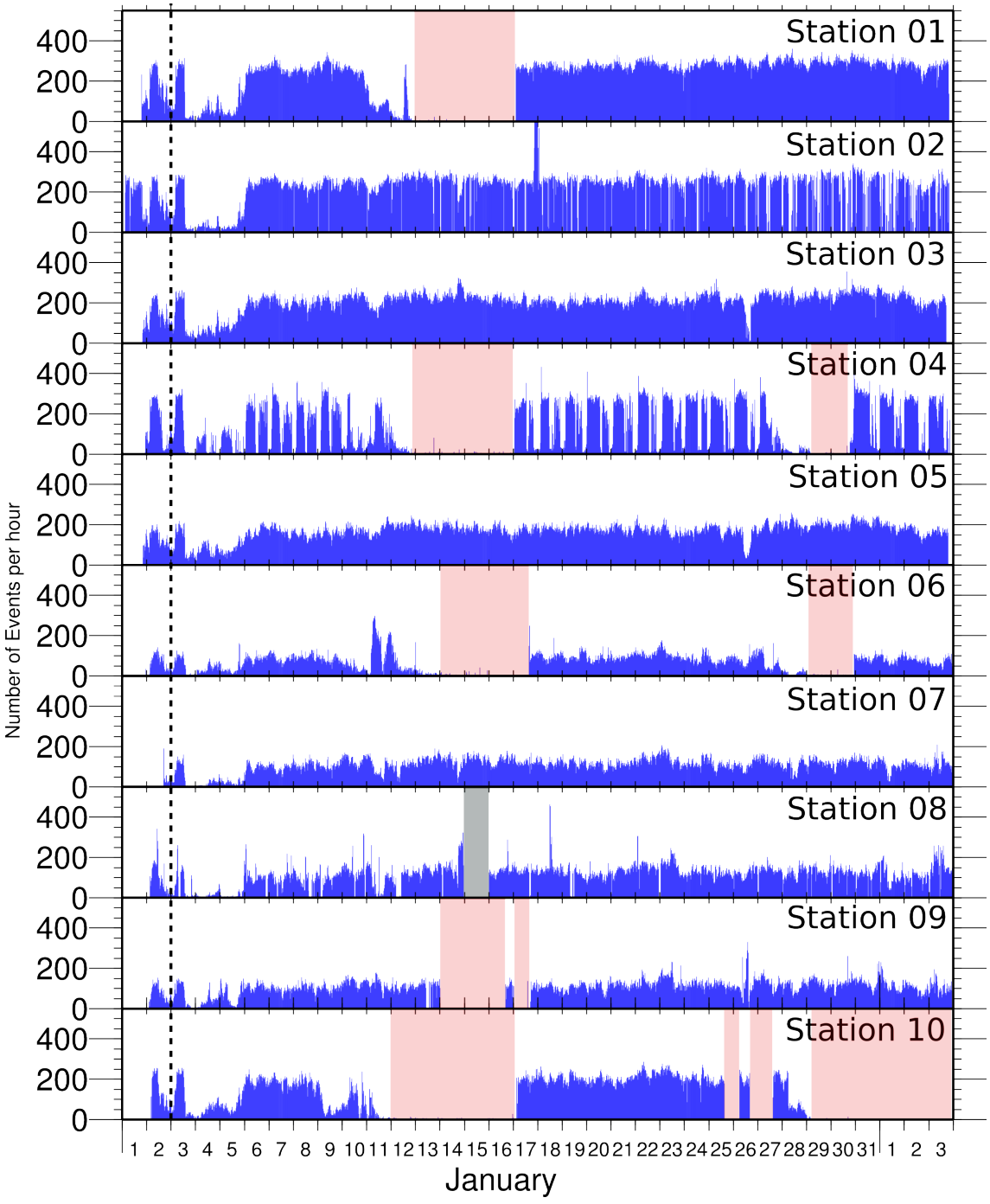

Figure 2.3: ***Basic seismic event counts for each station.*** *Event counts made using an STA/LTA algorithm with a ratio of 1:30 to identify possible seismic events. This is used to identify areas of data dropouts (pink) and memory card corruption (grey). All stations were installed and recording from the 3rd January (dashed line) to the 3rd February.*

The kinematic GPS station co-located with station 2 ran continuously with no problems.

During the 32-day recording period tens of thousands of seismic events were observed, with overlapping events occurring every few seconds (Figure 2.4a). All arrivals inspected were typical of basal seismic events in this region with a P-wave to S-wave travel time difference of 0.6 s, indicating events originated from around 2200 m distance (the average ice-bed interface depth). It appears there is little seismic noise from other natural sources in this area (e.g. crevassing) and anthropogenic noise is only seen when stations are serviced, at known times. Many of the basal seismic events produced very low amplitude seismic waves, close to background noise levels and are only visible on a single station. Low amplitude events, visible on a single station will not be easily identified or well located, therefore, it is important to identify coherent arrivals across multiple stations in order to accurately locate the microseismic events. A good number of events have high amplitudes with clear P-wave and S-wave arrivals (e.g. Figure 2.4b) and are visible across multiple stations. These events have a high frequency, impulsive P-wave arrival (Figure 2.5), with a corner frequency of $\sim$130 Hz and a lower frequency, but still clear S-wave arrival with a corner frequency of $\sim$50 Hz. The detection and location process described in Section 2.4 is optimised to identify these types of events.

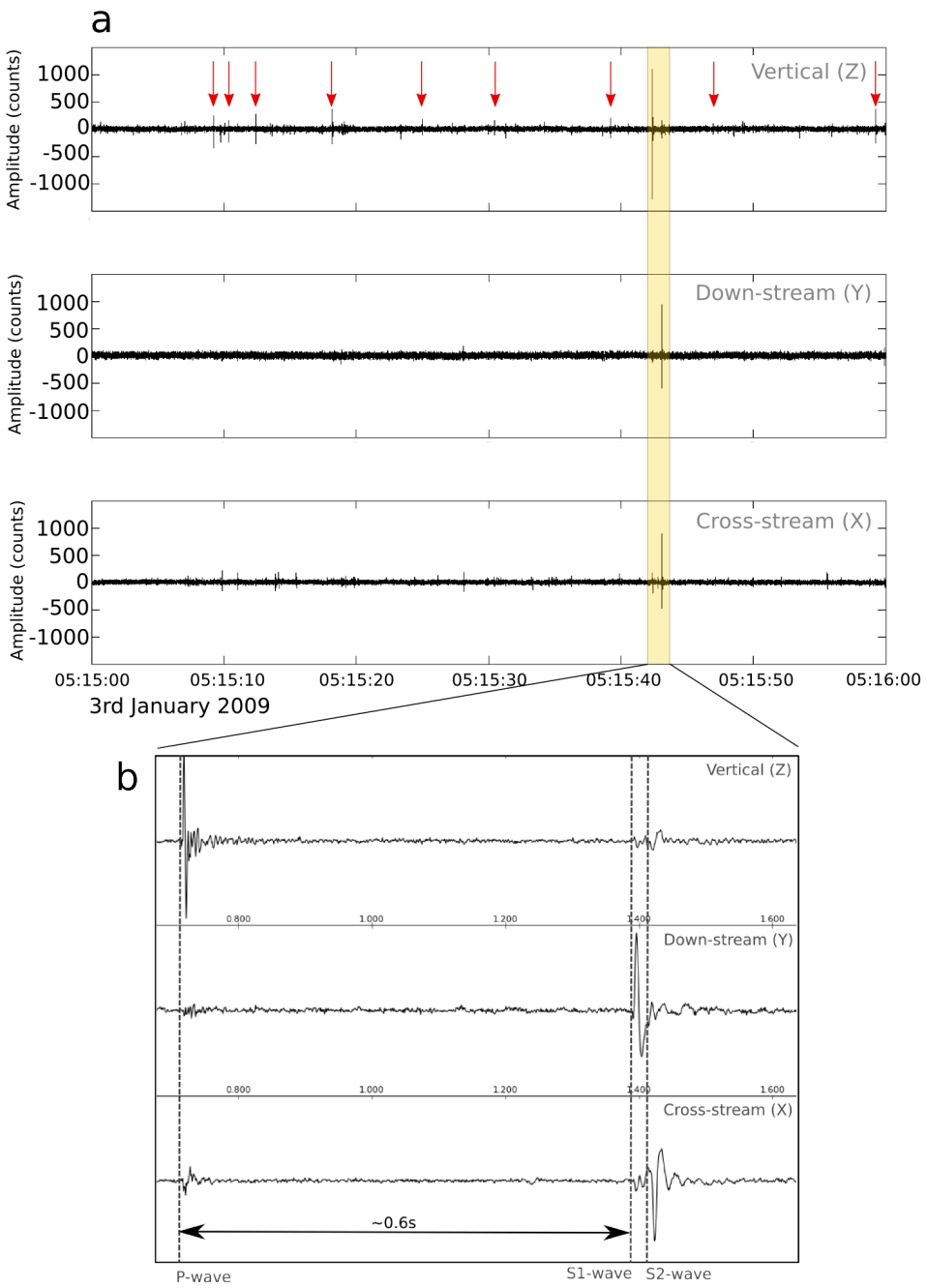

Figure 2.4: ***Nature of basal seismic events.*** *a) Example of one minute of data on three components of station 5, there are many low amplitude microseismic events (some of these are shown by red arrows). A high amplitude event with clear P- and S- wave signals is highlighted in yellow. b) Waveform of event highlighted in (a) - typical good quality basal seismic event recorded on all three components of a single station. These type of events are characterised by a high frequency impulsive P-wave (130 Hz) on the vertical component (Z) and strong shear waves on the horizontal components (X and Y). The vertical axis for each trace is the same and is in instrument counts, the horizontal axis is time.*

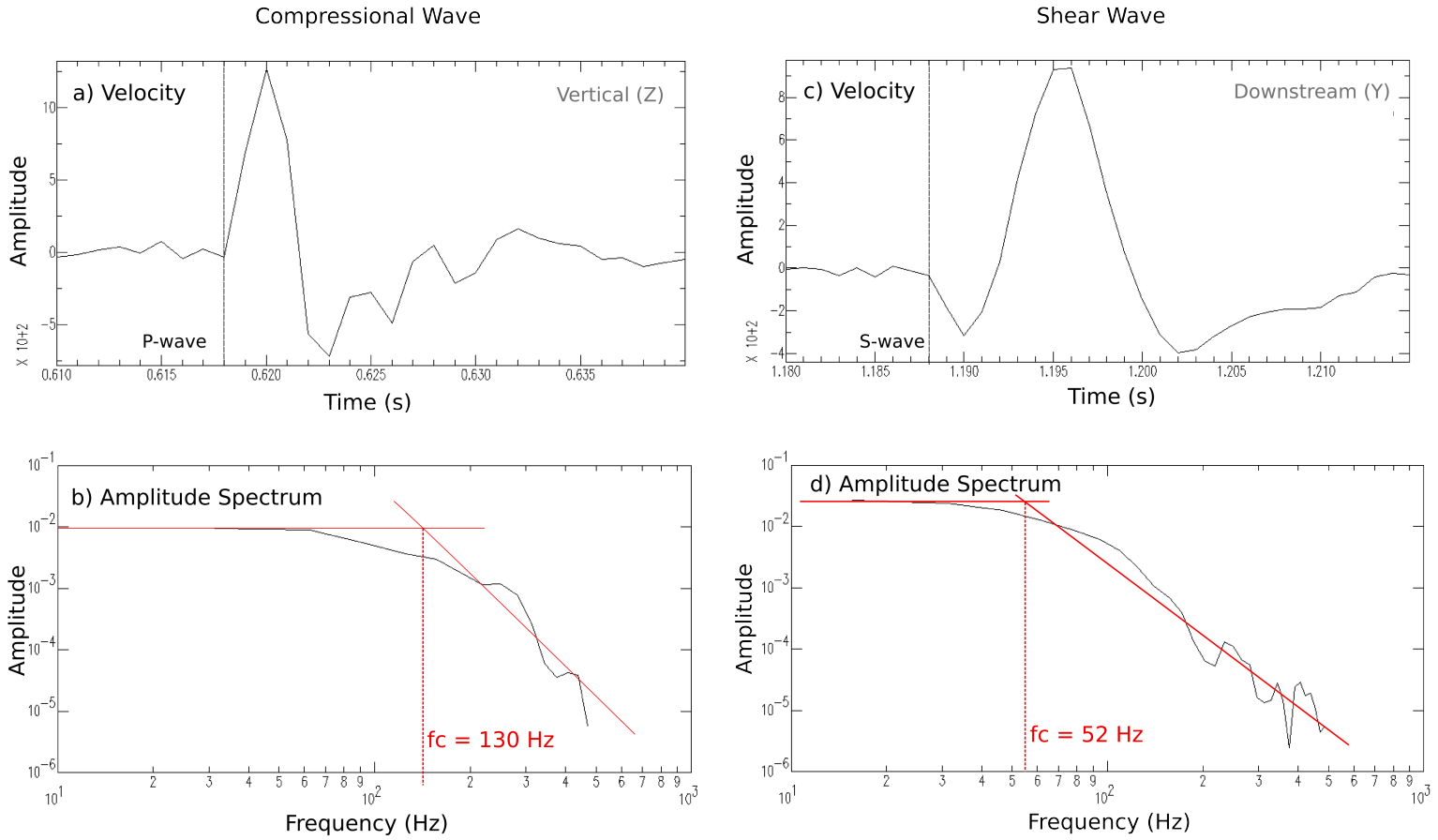

Figure 2.5: ***Amplitude spectrum of typical P-wave and S-wave.*** *a) A clear P-wave arrival on the vertical (Z) component of a single station. b) The amplitude spectrum of the P-wave waveform in (a), with a corner frequency of 130 Hz. c) A clear S-wave arrival on the downstream (Y) component of the same station. d) The amplitude spectrum of the S-wave waveform in (c), with a corner frequency of 50 Hz.*

2.3 Data Preparation

A number of quality control checks were made on the raw data to check for any inconsistencies or problems with the data set. Large scale data drop outs and gaps were identified using a basic STA/LTA event count, described in Section 2.2. However, a more detailed analysis of sections of the data revealed small data gaps due to timing problems on the stations using ISSI SAQS data loggers. Tests designed to check polarity convention of the arrivals recorded by the two different data loggers also revealed inconsistencies with the polarity and configuration of all the channels (X, Y, Z) on the ISSI SAQS stations. This section describes the problems found and the corrections applied to resolve the issues.

2.3.1 Timing Problems

As described in Section 2.1 the data loggers use GPS systems to synchronise their internal timing. The REFTEK RT-130 recorders keep their internal clocks constantly synchronised with GPS timing, but the ISSI SAQS data loggers only synchronise timing with the GPS every 5 minutes and record a timing correction; the difference in timing between their internal clock and the GPS time at that point. In general the drift between the internal ISSI SAQS clock and the GPS timing is small, around 1 sample (1 ms) in each 5 minute data section, which would not be likely to cause significant error in event location. However, if this correction is not applied to the raw data records, it leads to data gaps or overlaps between consecutive data files (Figure 2.6a), which causes corruption and data gaps when merging the files to form a continuous data record (Figure 2.6b).

This issue was discovered by the author during initial data checks, however, the process of applying the timing correction was devised and executed by A.M. Brisbourne (formerly of NERC's SEIS-UK geophysical equipment facility, now at the British Antarctic Survey) and I take no credit for the process described hencefourth in this section (Section 2.3.1). The total timing correction for each 5 minute data section was linearly interpolated and applied to the raw data. The timing of each data point was then rounded to the nearest sample (0.001 s), to ensure the sample times between all instruments remained constant. Once this process had been performed on each data section for each ISSI SAQS instrument, a continuous record for each station was created by merging the 5 min data files (Figure 2.6c).

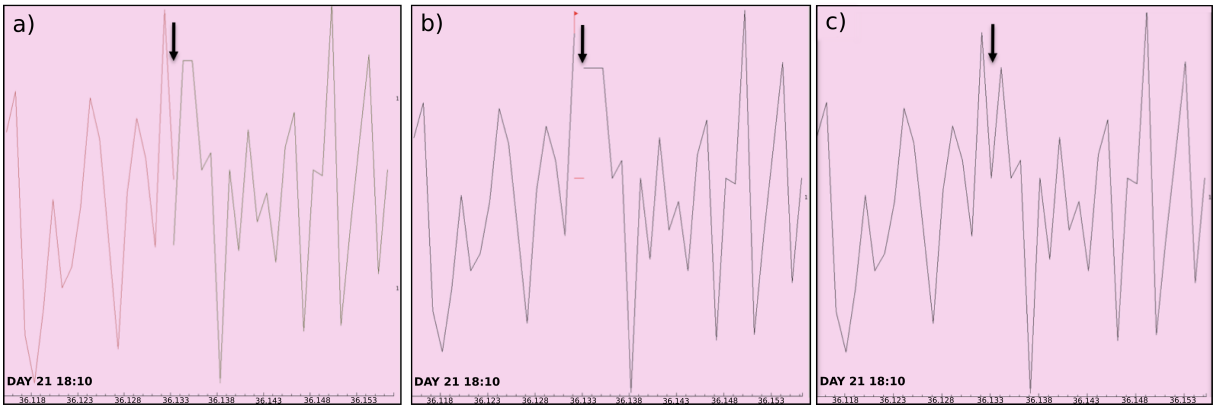

Figure 2.6: ***Example of timing correction for ISS SAQS instruments*** *a) Samples overlapping between two consecutive raw seismic data files - indicated by the arrow. b) The same two data files shown in (a) merged without timing correction being applied, causing a data gap where the overlap occurs. c) The same two data files merged after a timing correction has been applied to both raw data files, preventing overlapping data.*

2.3.2 Polarity Analysis

As two different types of data logger were used it was important to check the polarity convention of an arrival (i.e. compressive and dilation) was consistent between the two devices. This could be done during a pre-deployment huddle test or using an explosive seismic source, as these are known to have a compressive first motion only. Unfortunately neither of these methods was available for this data set, therefore, another seismic source that should have consistent polarity arrivals across all stations was needed. On the 18^{th} January 2009, during the recording period of this data set, an earthquake with $M_w = 6.4$ occurred near the Kermadec Islands, off the coast of New Zealand (USGS). As the array described in this dissertation is in the far field for the Kermadec Islands teleseismic event, the arrival waveform should be the same across all stations. The waveform of the teleseismic event was filtered between 0.1 Hz - 5 Hz, as the arrival is low frequency. A clear arrival can be seen at 14:22 on the vertical component (Z) of all stations (see Figure 2.7). For a given phase, there is a clear polarity reversal on the Z component between the stations using the REFTEK RT-130 and those using the ISSI SAQS data loggers. Curiously the polarity of station 6 (ISSI SAQS data logger) was consistent with the REFTEK RT-130 stations.The ISSI SAQS instruments have a pre-amplifier between the geophone and the data logger, and the internal

wiring in the pre-amps is not always consistent, causing some variation in the polarity of signals recorded. Conversely, geophones are connected directly to the REFTEK RT-130 data loggers and so there is no problem with changes in wiring convention. It was advised that the polarity convention of the REFTEK RT-130 stations was used as a reference by staff at NERC's SEIS-UK geophysical equipment facility, from whom all the instruments were on loan. The polarities for all stations were subsequently matched to the REFTEK RT-130 and inconsistencies corrected.

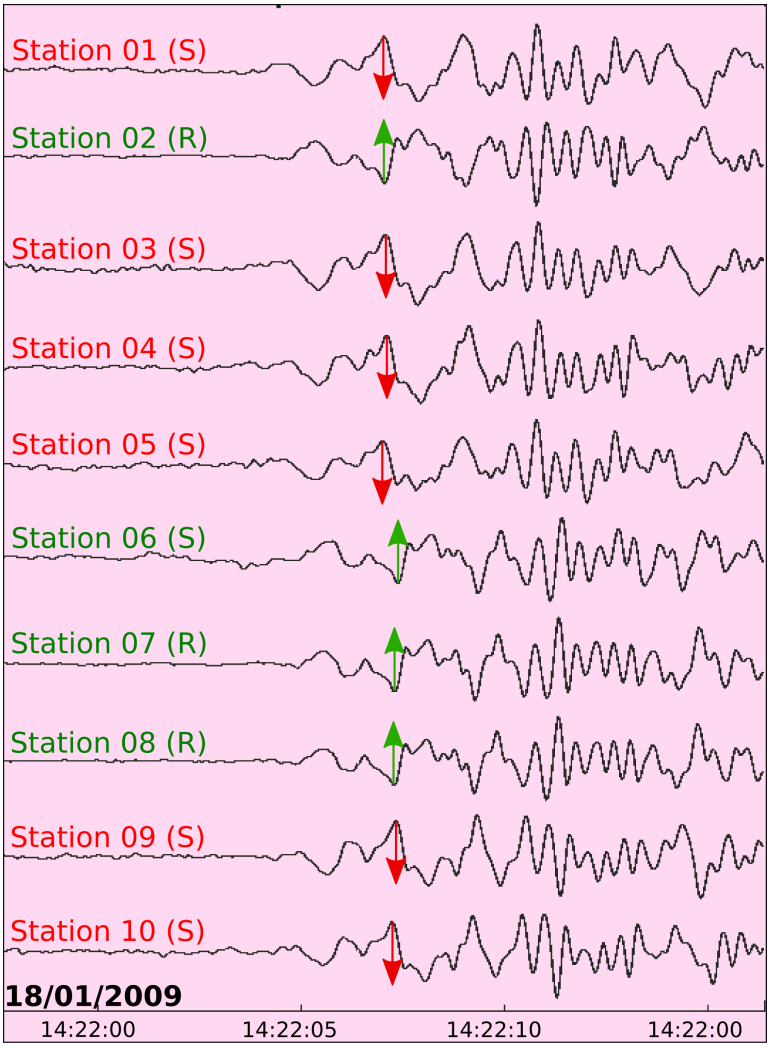

Figure 2.7: ***Teleseismic arrival across all stations on the vertical (Z) component, highlighting the inconsistent polarity between stations.*** *For a given phase, stations using the REFTEK RT-130 data loggers show an upwards deflection, as does station 6 which uses an ISSI SAQS data logger (green). All other stations using the ISSI SAQS data loggers show a downwards deflection (red).*

The teleseismic arrival was not recorded clearly on the horizontal components (X and Y) and therefore a different method was needed to verify the polarity of these. A hodogram of P-wave particle motion recorded on the horizontal components (X and Y) can be constructed, for a local microseismic event. This is essentially a cross-plot of the amplitude of the seismic signal on each component over a limited time window around the P-wave arrival. If the components are correctly orientated the particle motion should be consistent with the back-azimuth (receiver to event azimuth, clockwise from the Y component). This process also serves as an independent validation for the polarity convention of the REFTEK RT-130 data loggers. This process requires local microseismic events to have been detected and located and so it was performed once an event catalogue had been built (see Section 2.4). However, the detection and location process does not require any knowledge of the signal polarity, only P- and S- wave arrival times and so should not be adversely affected by any polarity inconsistencies found.

Hodograms of the raw data (see Figure 2.8) reveal that the particle motion (blue line) is only consistent with the back-azimuth (green line) on stations using the REFTEK RT-130 data loggers (stations 2, 7 and 8). Closer inspection of the waveforms for the stations using the ISSI SAQS data loggers showed that all of them had a reversed polarity X component compared to the stations using REFTEK RT-130 data loggers. In addition to this station 6 had a reversed polarity Y component and stations 4, 5 and 10 had the X and Y components incorrectly labelled and they needed to be swapped. This is most likely due to the channel assignment inside the pre-amps used with the ISSI SAQS data loggers. Once these changes had been applied the hodograms show a consistent particle motion on all stations (Figure 2.9).

It is also important to note that a compressive first motion is a downwards deflection on the REFTEK RT-130 data loggers; as all the records from the ISSI SAQS stations have been matched to the REFTEK RT-130 convention, that is the case for the whole of this data set.

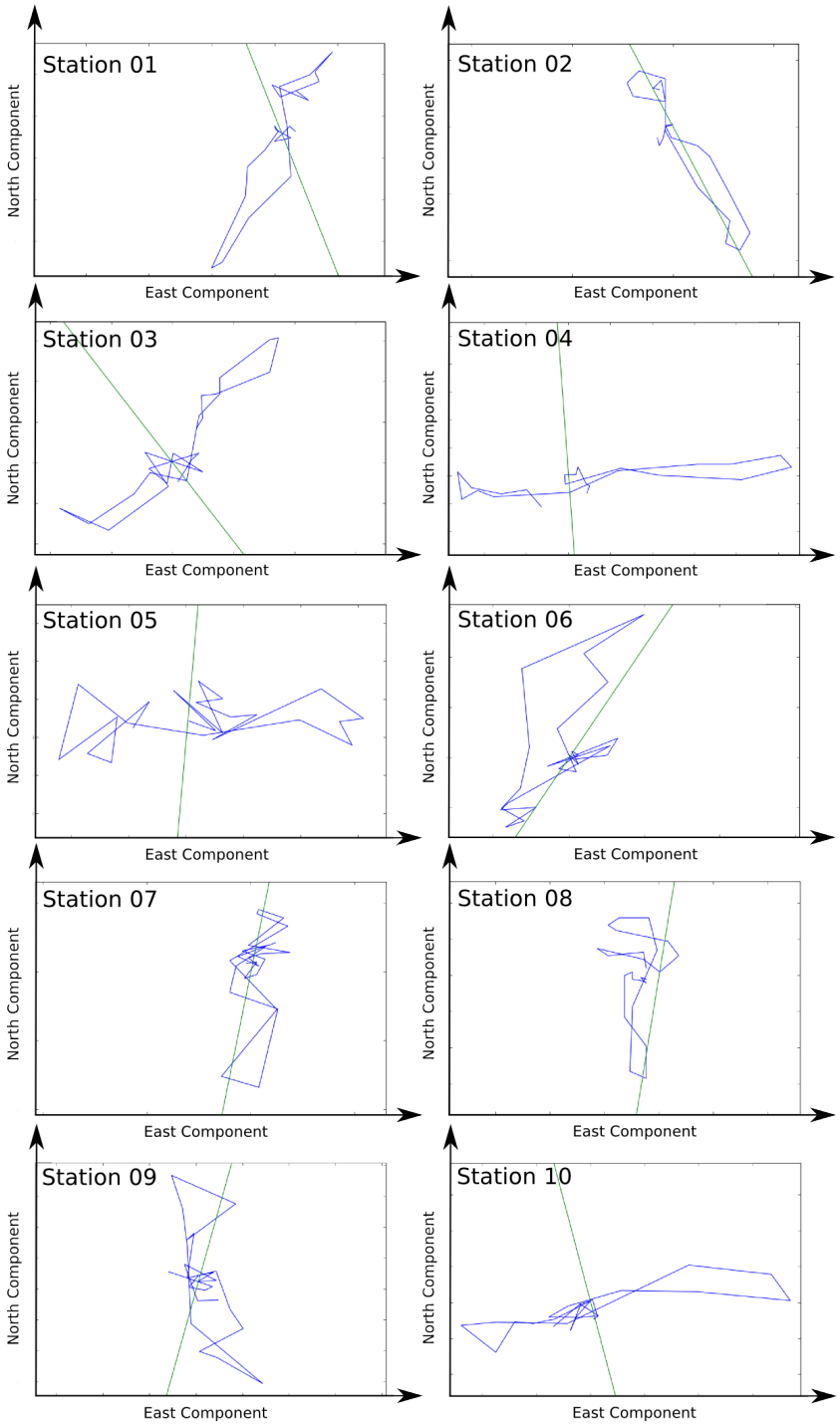

Figure 2.8: ***Hodograms of P-wave particle motion on X and Y components - raw data.*** *The particle motion of the P-wave on the X and Y components (blue) for a local microseismic event and the back azimuth clockwise from the Y component (green). Stations 2, 7 and 8, which use REFTEK RT-130 data loggers, show consistent particle motion. Other stations show inconsistent particle motion.*

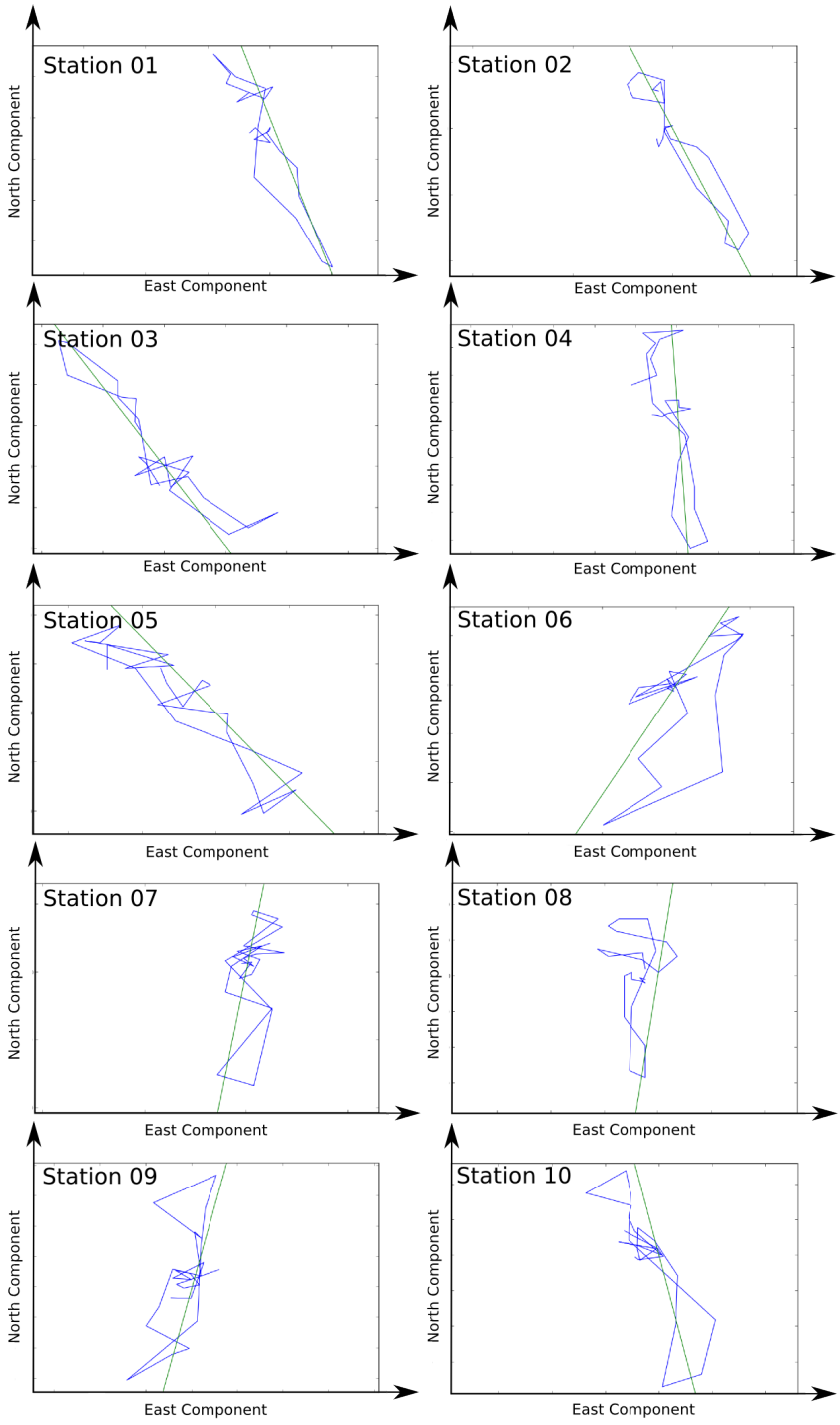

Figure 2.9: ***Hodograms of P-wave particle motion on X and Y components - corrected data.*** *The particle motion of the P-wave on the X and Y components (blue) for a local microseismic event and the back azimuth clockwise from the Y component (green). After corrections for component order and polarity are made the P-wave particle motion on all stations is consistent with the back azimuth.*

2.4 Microseismic Event Location Method

Due to the nature of this data set with events occurring every few seconds it would not be practical to manually identify and locate events, therefore an automated method of event detection and location is a more viable solution. This method needs to be able to deal with overlapping events, correctly identifying the phases associated with a single event across the ten stations in the array. A data processing flow based around the Coalescence Microseismic Mapping (CMM) technique (*Drew et al.*, 2013) was developed to achieve this (Figure 2.10). The CMM technique (Section 2.4.2) allows the detection and location of events without reducing data to discrete arrival-time picks and is designed to work with data collected on sparse seismic networks. The method allows coherent arrivals across the array to be identified, reducing 'false triggers' from seismic energy unrelated to a given event. Events identified using the CMM method were then refined using a further automated process (Section 2.4.3) to produce the final microseismic event locations described in Section 3.2. Details of each stage of the event location processing flow are given in the following sections.

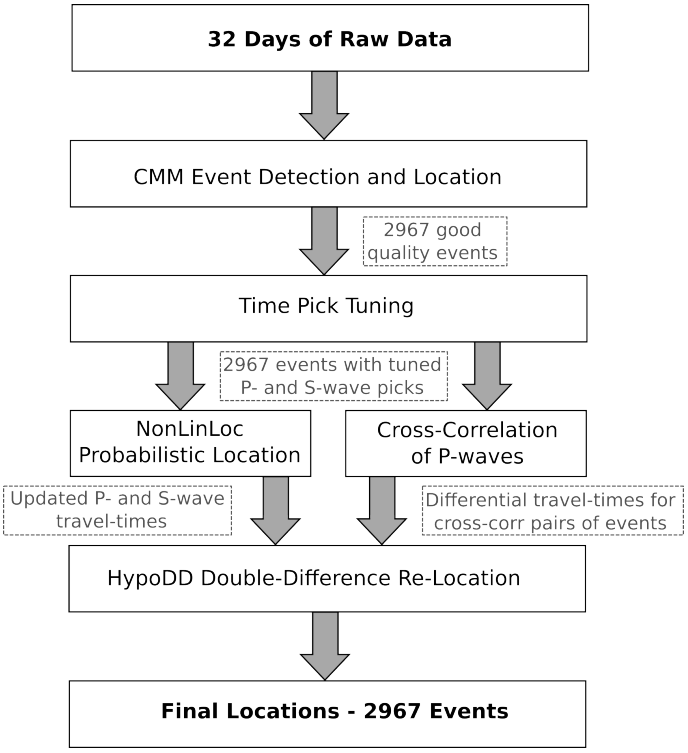

Figure 2.10: ***Data processing flow chart***

2.4.1 Velocity Model

Throughout each step in the locations process the same 1D seismic velocity model (Figure 2.11) was used. The P-wave velocity model contains a firn layer in the top 100 m, with a mean velocity of 2839 ±15 m s^{-1} derived from P-wave velocities determined by shallow refraction surveys, detailed in *Smith* (1997a). Below this a mean ice column velocity of 3841 ±15 m s^{-1} (*Smith*, 1997a) was determined using the relationship between ice temperature and seismic velocity (*Kohnen*, 1974). A velocity step was not inserted at the ice-bed interface as the velocity and depth of that region is not well constrained and a sharp step in the model can cause artificial clustering of hypocentres at the depth of the step. Instead the model consists of the ice column velocity down to a depth of 10 km, which is much greater than the possible ice depth. A constant Vp:Vs ratio of 1.95 was calculated using Wadati plots (*Wadati*, 1933) of P-wave and S-wave arrival times (Figure 2.12) and agrees well with values of *Roethlisberger* (1972). The S-wave velocity model for this area is calculated using the Vp:Vs ratio of 1.95, giving an average S-wave velocity of 1456 ±15 m s^{-1} in the firn layer and an average of 1970 ±15 m s^{-1} in the ice column.

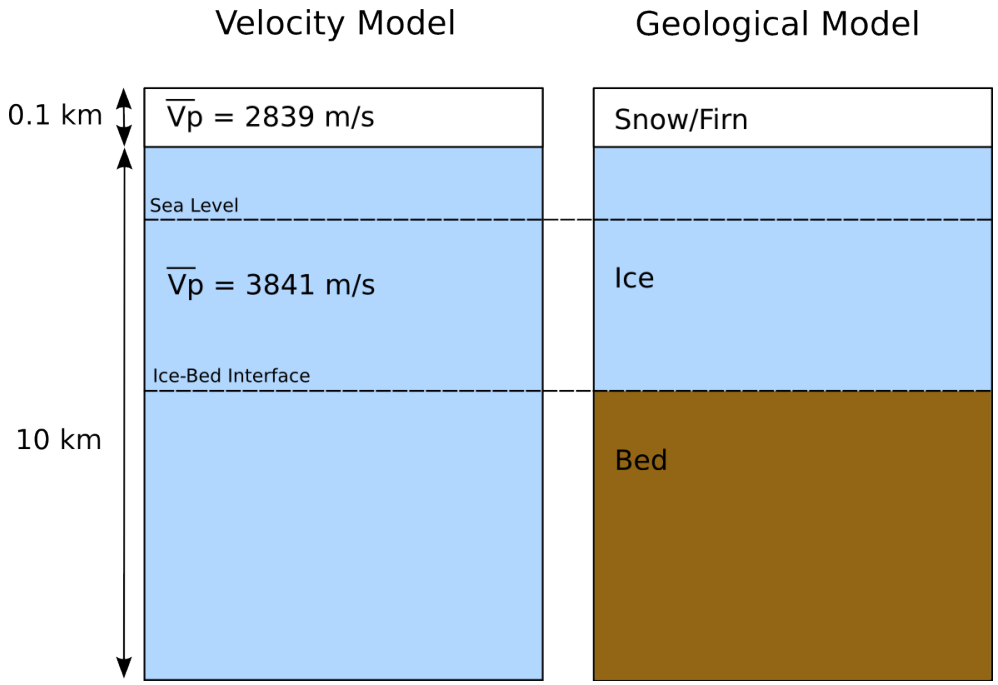

Figure 2.11: ***1-D seismic velocity model used to locate microseismic events.*** *The snow/firn layer has a mean velocity of 2839 ±15 m s^{-1} and the ice column a mean velocity of 3841 ±15 m s^{-1}.*

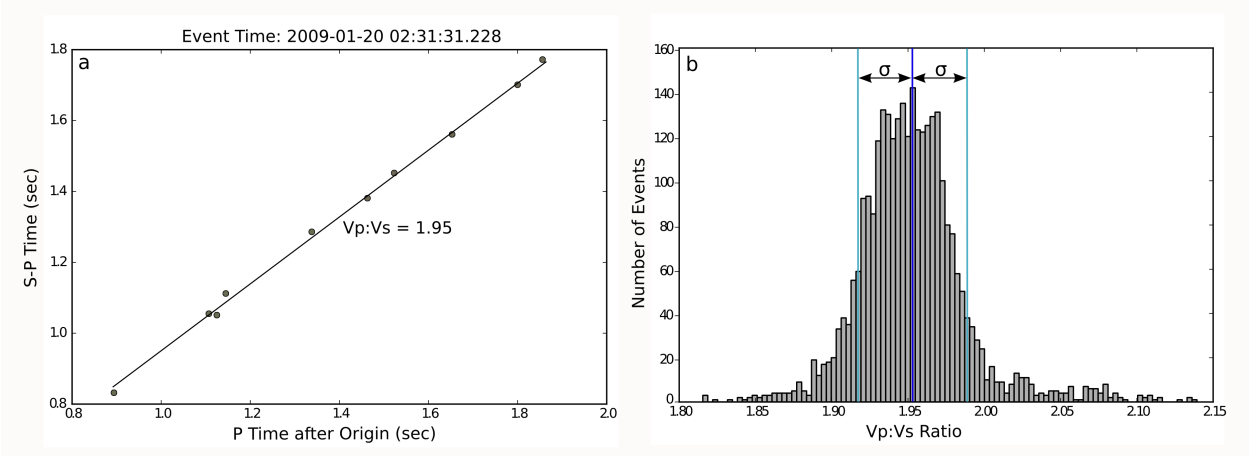

Figure 2.12: ***Vp:Vs ratio of seismic velocities.*** *(a) Typical Wadati plot for a single event, showing P-wave arrival time verses S-P time difference for each station. The gradient of the line fitting these points is used to calculate the Vp:Vs ratio. (b) Histogram of Vp:Vs ratio measurements for 2967 events, measurements have a mean, shown by the dark blue line, of 1.95 ± 0.04 (one standard deviation, which contains 80% of measurements.)*

2.4.2 CMM Automated Location Method

Initial event detection and location for the full data set was performed using the CMM method. In essence, the CMM method works by continuously migrating an envelope of seismic energy from each recording station back to each node in a pre-defined three-dimensional subsurface grid. A coalescence function is calculated at each grid node over time, to indicate where seismic energy concentrates, and a peak in this function indicates a location and origin time that best fits the observed seismic data.

The first stage in this process is to create a travel-time look-up table (LUT) by forward modelling P-wave and S-wave travel times from each node in the 3-D subsurface grid to each recording station, using a 1D seismic velocity model (see Section 2.4.1). The sub-surface grid had a node spacing of 150 m x 150 m x 50 m in X, Y and Z. This process only needs to be performed once for a given velocity model and speeds up the subsequent migration process.

The second stage is to calculate an 'onset function' at each station for the entire data set, by scanning through the continuous seismic record using an STA/LTA detection algorithm. A peak in the STA/LTA function indicates a possible arrival. This process is performed for both P-wave and S-wave arrivals, with P-wave energy being detected on the vertical component and S-wave energy on the combined horizontal components. Using both P-wave and S-wave arrivals helps to identify true seismic signals, rather than other sources such as instrument or wind noise. By testing on various sections of the data set it was found that an STA:LTA ratio of 1:30 produced a clear peak in the STA/LTA function for arrivals from basal seismicity in this data set and that a peak in the STA/LTA function with signal to noise ratio (SNR) > 9 represented a good quality arrival. This method does not reduce the data to discrete arrivals (i.e. picking the onset time of a P- or S-wave phase), but rather transforms the seismic waveform into an onset function signal which contains information about the seismic arrival time and SNR.

The final step is to migrate a Gaussian fit to the onset function back to every node in the sub-surface grid at each time step, using the LUT calculated in the first stage. At each time step a coalescence function is calculated at each grid node. This coalescence function is essentially the mean of the SNRs of the migrated onset functions. An event is triggered when the coalescence function exceeds a chosen 'detection threshold' (set to 2.5 in the case of this

data set). This threshold is essentially a SNR to reduce false events being triggered where the coalescence is low and it is likely that energy at a given time step is not related to a real event. To deal with uncertainties in the arrival times of the onset function CMM integrates the coalescence function over a time window, to include energy around the likely arrival time of an event at a given station. This integrated coalescence function is smoothed and the local maximum of the smoothed coalescence function represents the best fit event location. Additionally this results in an event location that is no longer tied to a subsurface grid node. The detection threshold of 2.5 was chosen conservatively, to maximise event detection, and yielded 14,644 events. These were then ordered by the SNR of the coalescence function and a selection were visually inspected. It was found that many of the identified events with lower SNR were of poor quality or false triggers. Events with a coalescence SNR>4 were found to be good and these were selected for use in this study, yielding 2967 good quality events.

For each detected event, CMM makes an 'autopick' of the P-wave and S-wave phase arrival time onset pick at each station in the array, using the maximum in the STA/LTA function at each station calculated in the second stage of the process as a guide. These picks are not used directly to locate events but are a useful by-product that allow the success of the method to be visually assessed and provide picks that can subsequently be used for further location refinement. Each event detected by this method was manually inspected to verify the technique.

A typical event of the quality described above is shown in Figure 2.4. The P-wave arrival is impulsive with a dominant frequency of around 130 Hz, typical of basal seismicity (*Anandakrishnan and Bentley*, 1993). The S-wave arrival is often 'split', appearing at slightly different times on the two horizontal components, due to the presence of anisotropy in the seismic velocity structure of ice. The fastest S-wave arrival (S1) was always used in this study.

2.4.3 Location Refinement

The CMM technique was an efficient means of processing a large data set, to identify and approximately locate good quality microseismic events. In order to analyse the events in more detail the locations were first refined using the following automated process (Figure 2.10). First, the CMM autopicks of P-wave and S-wave arrival-times for each station were tuned

(i.e. adjusted to more consistently identify the onset of the seismic arrival) by calculating the SNR in a limited window, 50 ms either side of the CMM arrival times. This 'time pick tuning' process produced a more precise and consistent onset pick (the time at which the wavelet arrival begins) for each event at each station. Using these tuned arrival times, the location of each event was re-calculated using a probabilistic, non-linear earthquake location technique (NonLinLoc; *Lomax et al.* (2000)). This technique works by calculating a probability misfit between theoretical modelled arrival times and observed arrival times at each station from each node within a 3-D subsurface grid. A minimum in this function (i.e. the highest similarity between modelled and observed arrival times) indicates a maximum likelihood origin time and location. Independently, travel-time picks were further improved by cross-correlating waveforms over a window around the P-wave arrival. This process produced a set of differential travel-times for pairs of events with highly correlated waveforms ($r > 0.75$). Finally, the refined locations (from NonLinLoc) and P-wave differential travel-times from cross-correlation were input to a double-difference, relative location technique (HypoDD; *Waldhauser and Ellsworth* (2000)). This technique exploits the fact that events that are spatially close will have very similar travel paths and thus differences in their travel times to a given station can be attributed to the spatial offset between events independent of velocity model errors. This process serves to improve relative locations within clusters of events that are spatially close and have similar waveforms. As a by-product of the relative location process HypoDD outputs events that it considers to be grouped in a cluster. The waveforms for events within a cluster can then be manually checked and re-grouped or split into smaller clusters depending on waveform similarity. Events within manually refined clusters can then be run through HypoDD a second time, cluster by cluster in order to get an even more refined relative location.

Figure 2.13 gives an overview of the locations output at each step of the process to illustrate the improvement with each stage. A comprehensive discussion of the final events locations can be found in Chapter 3. The locations output by the CMM process are shown in pink and, as expected, show the largest scatter in depth and X-Y locations. Many of them are masked by the locations output from NonLinLoc(light blue), suggesting the change in absolute location between the methods is not large. There is a noticeable improvement in the spatial clustering of events using the HypoDD method (dark blue), particularly in the X-Y plane.

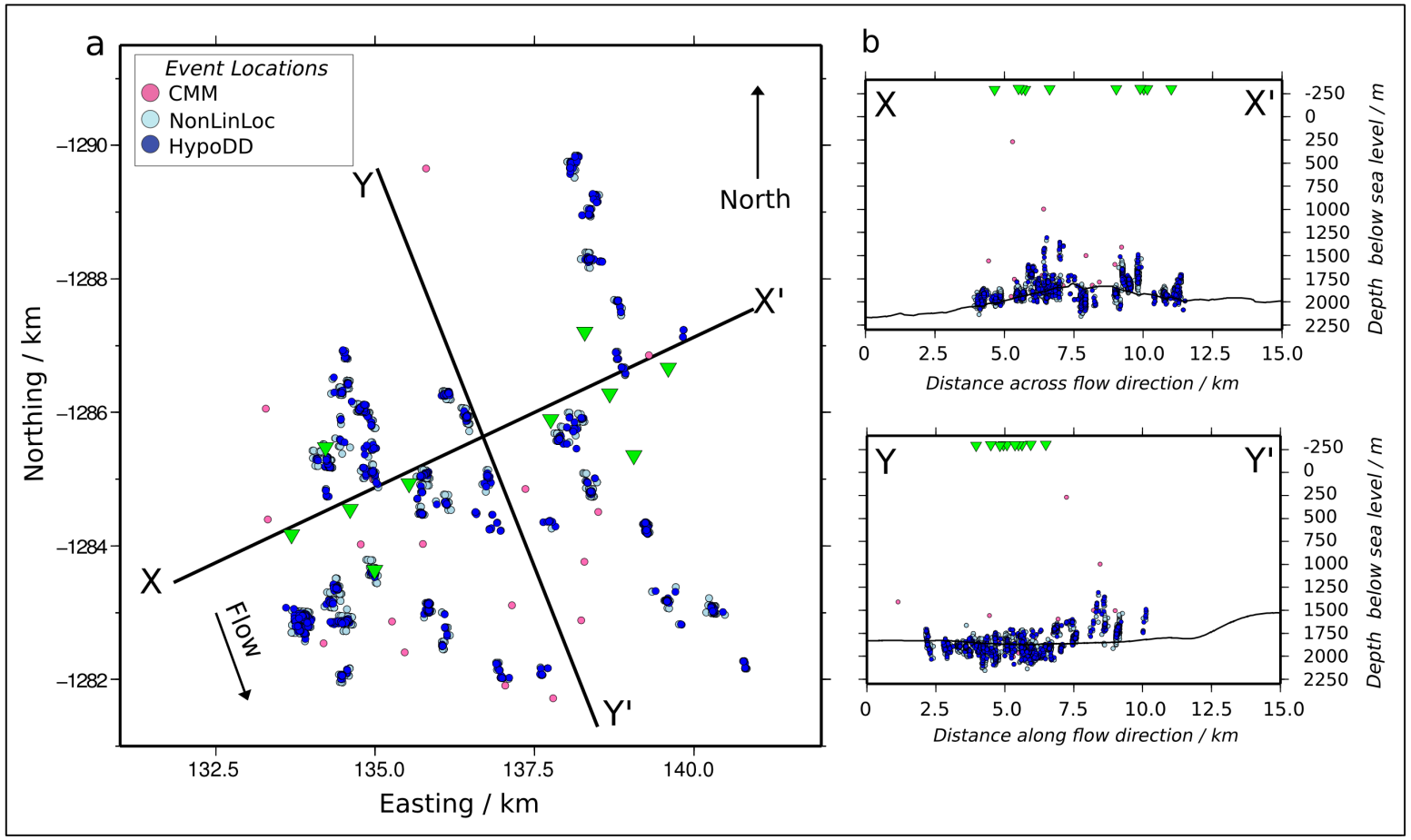

Figure 2.13: ***Improvement of event locations with refinement.*** *CMM locations (stage 1) are shown in pink, NonLinLoc locations (stage 2) are in light blue and HypoDD locations (final event locations) are shown in dark blue a) Plan view of event locations, spatial clustering of locations improves with each stage. b) Vertical profile across flow direction X-X' (top) and along flow direction Y-Y' (bottom) showing improved clustering of locations in depth, although not as dramatic as in the horizontal (X-Y) plane.*

2.5 Shear Wave Splitting Analysis Methods

Around 3000 good quality events were detected and located on 10 seismic stations over the 32-day recording period. This means there are ∼30,000 shear wave splitting measurements to be made, one for each shear wave arrival on each station for each event. As with the event detection and location process, it would not be practical to make this quantity of measurements manually and so an automated approach was used. The automated method of *Wuestefeld et al.* (2010) provides a way to process large quantities of microseismic data, outputting two splitting parameters for each measurement, the polarisation orientation of the fast shear wave (Φ) and the delay time (δt) between the fast and slow shear waves (Section 2.5.1). The method also calculates an automated 'quality factor' (Q) of the resulting shear wave splitting measurements which can then be used to filter the results by determining a suitable threshold of Q above which the measurements are of 'good' quality. The splitting parameters output by this method are then used to invert for the type of ice fabric which best fits the measured S-wave anisotropy (Section 2.5.2).

2.5.1 Shear Wave Splitting Analysis

As a shear wave travels from the base of the ice to the surface through an anisotropic ice fabric a number of things can happen. The shear wave can continue to propagate 'un-split' if the initial polarisation coincides with an anisotropic axis of symmetry or if the wave path is along an isotropic symmetry axis in an anisotropic medium. These are known as 'null' cases. If neither of these cases are true the S-wave is split into two mutually orthogonal S-waves (see Figure 1.5), polarised along the anisotropic axis of symmetry. As ray paths from each event to each station cover a variety of angles and inclinations, the splitting for each of these ray paths can be measured to build up a picture of the bulk elastic anisotropy of the ice fabric.

Shear waves are recorded at the surface, primarily on the horizontal components of the geophones at each of the 10 stations. The two split S-waves arrive at a receiver separated by a delay time (δt), which is proportional to the strength of the anisotropy ($\%A$) along a given ray path (see Section 2.5.1.1) and with an orientation of the fastest shear wave (Φ) along that ray path. The 'fast S-wave polarisation' (Φ) refers to the orientation in the ray frame and 'strike of the fast S-wave polarisation' (ϕ_p) in the geographic coordinate system

(clockwise from North). The automated technique of *Wuestefeld et al.* (2010) was used to make these measurements across all 2967 events.

Before the analysis takes place the traces for each event at each station are rotated from their field orientation (X, Y, Z) with the horizontal components pointing along flow and across flow (see Section 2.1) into geographical E, N, Z orientation. In many situations the traces are then rotated into the ray-frame in order to maximise the S-wave energy on the transverse components (SV and SH). However, due to the low velocity firn layer at the surface of Rutford Ice Stream most rays arrive at the receiver at near vertical angles of incidence, with the majority of S-wave energy on the horizontal components and so this step is not necessary.

The core principle of the SWS analysis method of *Wuestefeld et al.* (2010) can be summarised as follows: First a time window is defined around the picked S-wave arrivals on the horizontal (E and N) components of a geophone. Then a grid search over all possible values of fast shear wave orientation (-90° $< \Phi <$ 90°) and delay time (0 $s < \delta t <$ 0.1 s) is performed to determine which combination of these splitting parameters best removes the effects of splitting. The range of trial values of δt was chosen by manual testing on a subset of data. Before the correction there are two distinct S-wave arrivals (Figure 2.14a) and the particle motion is 'x shaped' (Figure 2.14b), once corrected the shear wave appears as a single arrival and the particle motion is linearised. The initial source polarisation of the shear wave is also determined from the corrected traces.

The automation comes into this technique in two ways. Firstly, the measurement is very sensitive to the choice of the analysis window around the shear wave, ideally a solution for the splitting parameters should be stable over a range of analysis windows to ensure the measurement is robust. The cluster analysis method *Teanby et al.* (2004) is used to automatically select the best analysis window from 25 test windows. The second part is in determining a quality factor (Q) in order to provide objective quality control of the measurements without the need to visually inspect each one. The value of Q is calculated by using two different techniques to determine the splitting parameters and comparing the results. The two methods are the cross correlation method (XC) and the eigenvalue method (EV).

The XC method is performed by rotating the horizontal components into a test orientation, applying a time shift to one of the components and assessing the similarity of the two signals

by calculating the cross-correlation coefficient between the two rotated components (*Ando et al.*, 1980). This is repeated for the full range of rotation angles and time shifts to find the best fit combination to correct for the splitting. The value of rotation and time shift that provide the optimal correction give the polarisation direction of the fast shear wave (Φ) and time delay (δt) for that measurement respectively. Qualitatively the EV technique works by searching for the value of Φ and δt that best linearise the particle motion on the two horizontal components (see Figure 2.14b). It does this by calculating the co-variance matrix for each test orientation and time shift combination and searching for the most singular valued matrix (*Silver and Chan*, 1991) by minimising λ_2/λ_1, where λ_1 and λ_2 are the eigenvalues of the co-variance matrix.

A comparison between the values of the splitting parameters, Φ and δt, determined using the two methods allows the identification of good, bad and null measurements. High similarity between the splitting parameters gives a value of Q = 1 (a good splitting measurement), null values (i.e. no splitting) are represented by Q = -1 and Q = 0 indicates a poor measurement that is neither a clear splitting measurement or a clear null. These values of Q can then be used to filter out bad or null measurements (Section 2.5.1.2). The final values of Φ and δt output by the process are those determined by the EV method.

2.5.1.1 Calculating the Strength of Anisotropy and Strike of the Fast Shear Wave

From the output of the automated shear wave splitting process the values of δt and Φ are used to calculate $\%A$ and ϕ_p. The strength of anisotropy ($\%A$) is calculated from the measured δt using Equation 2.1. This is the percentage shear wave velocity variation from the average isotropic velocity model value of $\overline{Vs} = 1944ms^{-1}$. Where r is the source-receiver straight line distance. As the traces in this study were rotated into a geographic coordinate system, rather than the ray frame, before analysis the measured value of Φ is equal to ϕ_p for this data set.

$$\%A = \frac{\overline{Vs} \times \delta t}{r} \times 100 \tag{2.1}$$

2.5.1.2 Quality Control

The quality factor (Q) is calculated by comparing the splitting parameters determined using two different methods, the EV method and the XC method (Section 2.5.1). Good SWS measurements should have a high positive value of Q with the best measurements having a value of Q = 1. From manual inspection of the data it was found that measurements with Q > 0.8 were good measurements (Figures 2.14a and 2.14b). However, using Q alone to determine high quality measurements breaks down for measurements performed on unclear waveforms with a low SNR.

Low quality SWS measurements can still result in a high Q value if the splitting parameters determined by the two methods are both in agreement (Figures 2.14c and 2.14d). Therefore, events were also filtered by SNR (determined as part of the automated analysis process) and it was found that waveforms with a SNR > 7.5 and a $Q > 0.8$ represented reliable and good measurements. The results presented in Chapter 5 are the 5951 measurements out of the 29670 automated measurements which fit these criteria. Null measurements (those with a Q value around -1) can contain information about the anisotropy of the fabric they have travelled through. However, they are not suitable for use in the inversion method for this study (Section 2.5.2) as the cause of the 'null' is unknown. It could be due the wave path being along an isotropic symmetry axis or because the initial polarisation coincides with an anisotropic axis of symmetry.

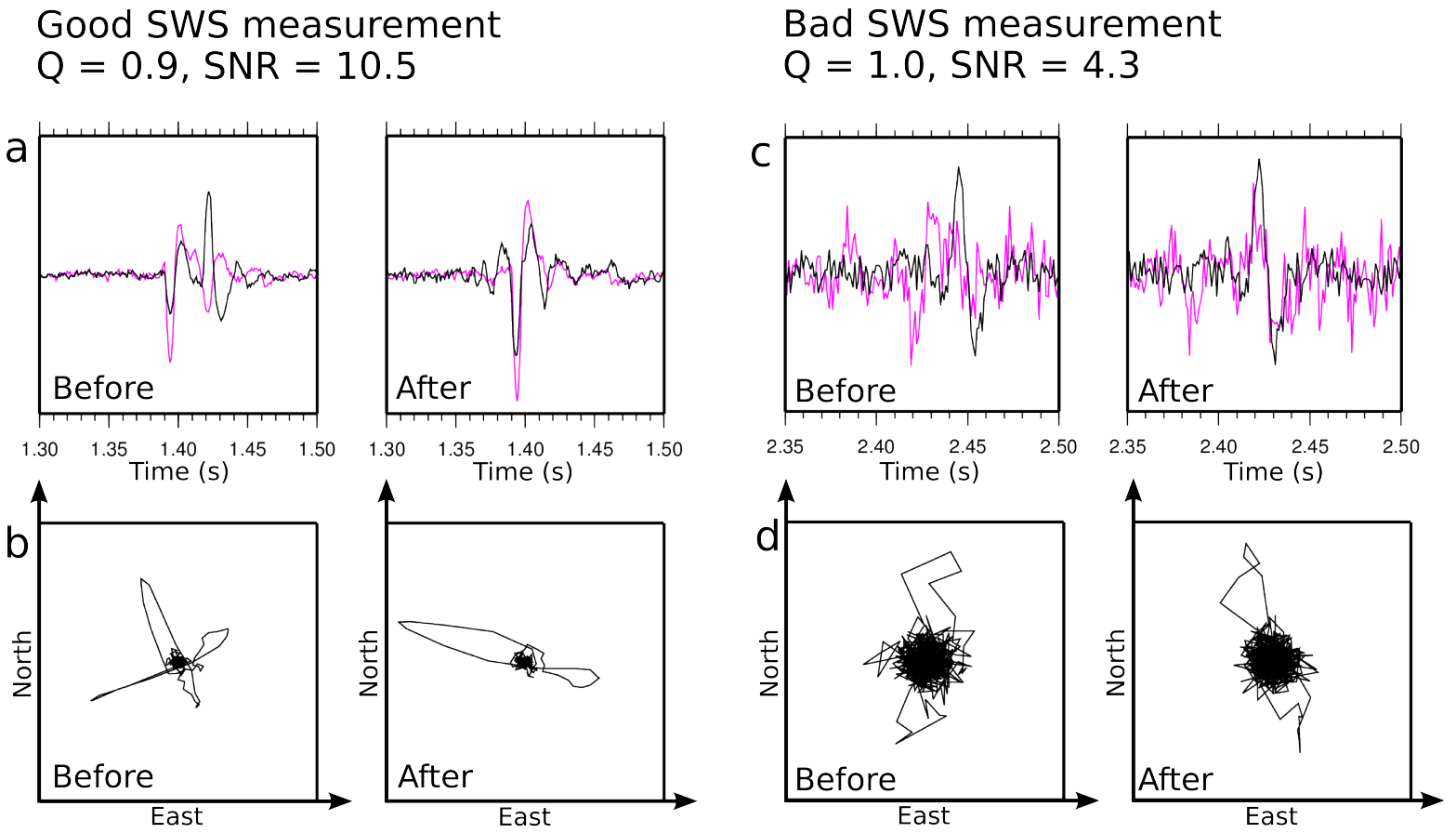

Figure 2.14: ***Example of good and bad quality shear wave splitting measurements*** *Split shear waves and associated particle motion before and after correction by determining the splitting parameters (Φ and δt). a) A clear split shear wave before correction and the well matched waveforms after correction. b) The shear wave particle motion before correction showing two clear orthogonal directions and after correction showing linearised particle motion. c) A low SNR ratio input waveform with S-wave signal close to background noise level. d) The shear wave particle motion before correction is not clear and does not show the characteristic X-shape as much of the measurement is masked by noise, after correction the particle motion is not clearly linearised*

2.5.2 Inversion for Ice Fabric

As described in Section 1.3.2 different types of ice crystal preferred orientation (CPO) fabrics form under different stress regimes. In general c-axes rotate towards the axis of compression and away from the axis of extension. In order to relate the shear wave splitting parameters that have been measured to the type of ice fabric they have travelled through I first need to understand how each of these ice fabrics affects the propagation of shear waves and thus the pattern of shear wave splitting that would be recorded at the surface.

Maurel et al. (2015) derived equations for the elasticity tensors associated with a cluster, thick girdle and vertical partial girdle fabric as a function of the opening angles θ and ξ. The elasticity tensor associated with the horizontal partial girdle can be formed by a rotation of the tensor for the vertical partial girdle. The elasticity tensors can then be used to determine the phase velocities of S-waves travelling through the specified fabric at different angles and thus the shear wave splitting parameters ($\%A$ and Φ) associated with this. Figure 2.15 shows the calculated pattern of SWS for each of the commonly observed ice fabric types, on an upper hemisphere plot. A combination of two fabric models can be made, for example a cluster and a thick girdle model, by mixing the two models in defined proportions (e.g. 70% thick girdle and 30% cluster) using a Voigt-Reuss-Hill (VRH) average. The phase velocities and resultant SWS parameters are then calculated from this mixed model.

In order to determine the fabric model that best fits the SWS measurements made on the data (Section 2.5.1) an inversion method created by A. Baird was used (A. Baird personal communication). Input data to the method are the splitting parameters for each measurement ($\%A$ and Φ) and the azimuth and inclination of the ray on which the measurement was made. It should be noted that in the case of this data set the measured value of Φ (which equals ϕ_p as traces were not rotated into the ray frame) needs to be transformed into a true value of Φ (in the ray frame) before inversion.

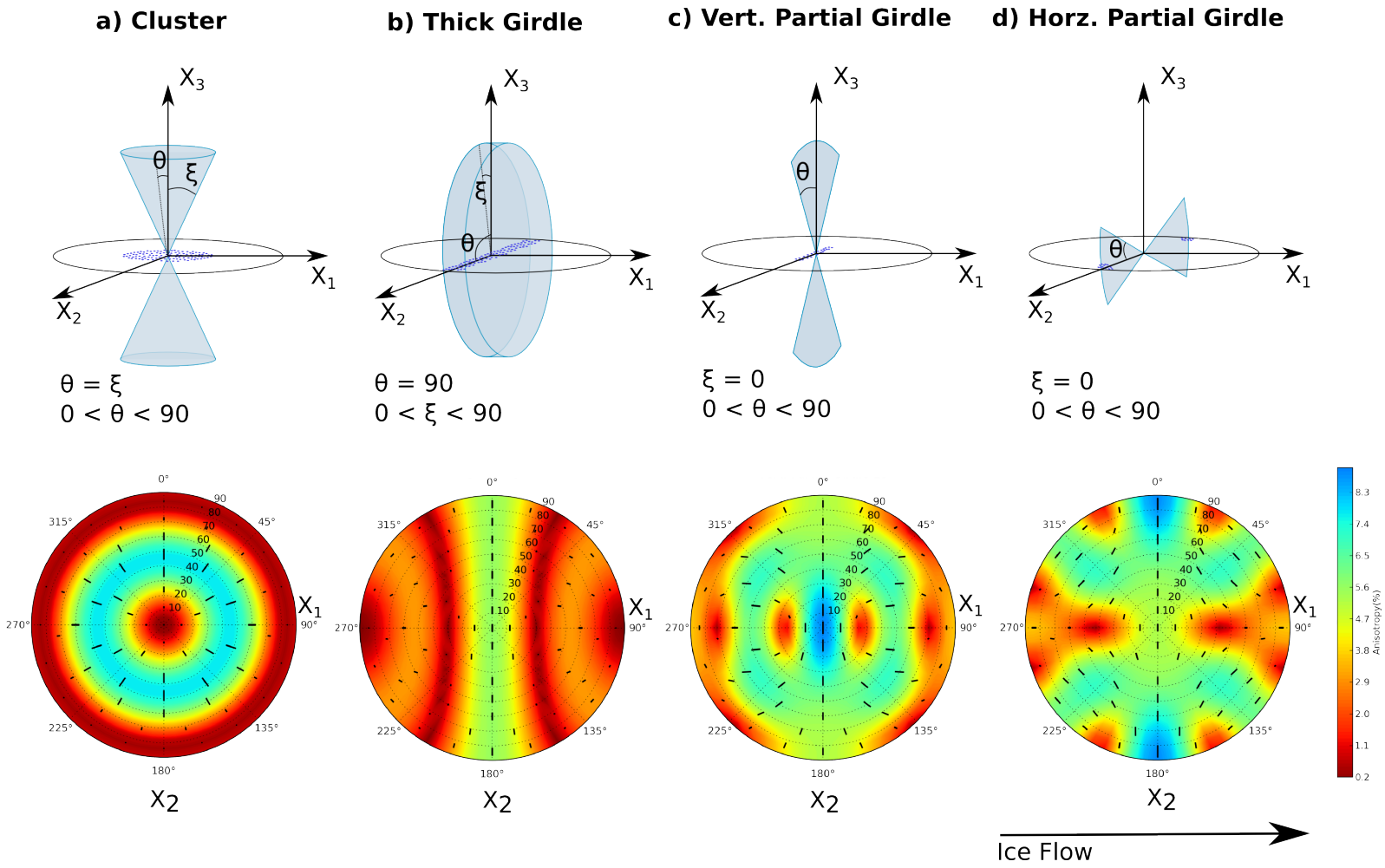

Figure 2.15: ***SWS parameters expected for different ice fabrics****. The top row shows a schematic for each fabric types, with the envelope of c-axes (blue area) and the projection of these c-axes on an upper hemisphere plot (blue dots on the horizontal plane), as in Figure 1.4. The bottom row shows the magnitude of SWS and direction of the fast shear wave for each fabric type on an upper hemisphere plot. a) Cluster with an opening angle* $\theta = 30°$*. b) Thick girdle orientated perpendicular to flow direction with* $\xi = 15°$ *d) Vertical partial girdle orientated perpendicular to flow direction with* $\theta = 15°$ *d) Horizontal partial girdle orientated perpendicular to flow direction with* $\theta = 15°$

For a trial ice fabric model the modelled splitting parameters are calculated at each point that an input SWS measurement exists and the misfit between the modelled and measured splitting parameters is calculated using the vector misfit given in Equation 2.2 (A. Baird personal communication). This is essentially a sum of the magnitude of the vector difference between the modelled splitting parameters ($\%A_m$ and Φ_m) and the measured splitting parameters ($\%A_d$ and Φ_d). Where n is the number of SWS measurements made and the factor of 2 accounts for the fact that Φ has 180° periodicity, rather than 360°.

$$\sum_n = \sqrt{(\%A_m sin2\Phi_m - \%A_d sin2\Phi_d)^2 + (\%A_m cos2\Phi_m - \%A_d cos2\Phi_d)^2} \tag{2.2}$$

As the inclinations and azimuths at which measured values are available can be highly irregular, the measured values of SWS are smoothed before inversion by taking the average of the measurements in inclination and azimuth bins of 5°× 5°. This is to prevent the inversion being biased towards areas where there are a high density of measurements. The misfit calculation is repeated for all variable parameters of the trial fabric model (opening angles and proportions of each input fabric) and the misfit is minimised using the differential evolution method (*Storn and Price*, 1997) to reach the best fit of the input fabric model to the data. The parameters of the best fit fabric model (proportion of each input fabric and opening angles for each fabric) are output for comparison with the measured splitting parameters.

While this method is limited to inverting for the ice CPO fabric models in Figure 2.15, or a combination of these models, this is a reasonable set of types of observed ice CPO fabrics and a good fit to the data can be found (see Chapter 5).

Chapter 3

Microseismic Event Locations

3.1 Introduction

During the 32-day recording period 2967 good quality (as defined in Section 2.2) basal microseismic events were detected and located, following the processes outline in Section 2.4. The location, timing and waveforms of each event provide information about the basal environment of Rutford Ice Stream which is investigated in this chapter. The chapter begins by presenting the results of the event location process and goes on to investigate the source and magnitude of uncertainties in this location using synthetic seismic events; this allows better constraints to be placed on the likely origin of the events. The temporal variation in seismicity is investigated with particular reference to known variations in surface flow velocity of the ice stream, due to tidal forcing. I discuss how the location and timing of these events can be used to infer characteristics of the basal environment on Rutford Ice Stream and how the ice stream motion may be accommodated by this environment.

Much of this chapter is included the following publication:

Smith, E. C., A. M. Smith, R. S. White, A. M. Brisbourne, and H. D. Pritchard (2015), Mapping the Ice-Bed Interface Characteristics of Rutford Ice Stream , West Antarctica, Using Microseismicity, *J. Geophys. Res. Earth Surf, 120*, 1881-1894, doi:10.1002/2015JF003587.

3.2 Basal Seismicity - An Overview

Figure 3.1 gives an overview of the locations of the 2967 events observed over the 32-day recording period. The topography of the ice-bed interface from radio echo sounding (RES) data is shown for reference (*King et al.*, 2009). A map view of the seismicity (Figure 3.1a) reveals that events are concentrated in spatial clusters. An individual cluster consists of many events occurring in close proximity to each other, with a near identical waveform at a given receiver throughout the 32-day recording period (Figure 3.2). This indicates that events within a cluster are highly likely to come from a single repeated failure point. Seismicity at a cluster location turns on and off over time suggesting that a failure point activates repeatedly. The range of time for which a cluster is active and the total number of events within a cluster varies across the survey area. Some clusters are active in bursts of several hours over the full 32-day recording period, for example the cluster in Figure 3.2a, which comprises 101 events. At the other end of the scale we see clusters that are active just once, for example the cluster in Figure 3.2b, which contains 7 events in total.

Vertical profiles along the ice flow direction and perpendicular to this (Figure 3.1b) confirm that the seismicity is close to the ice-bed interface. However, events seem to originate from both above and below this boundary in vertical 'pipe-like' features. Clusters on the right hand side (downstream) of profile Y-Y' appear to be located within the ice, whereas events in the centre and to the left hand side (upstream) of the profile appear to occur around the interface. Given the observation that events within a cluster have a consistent waveform at a given receiver, suggesting a consistent source mechanism and location, it is unlikely that the events in a single cluster lie both above and below the ice-bed interface. It is therefore important to determine the origin of these observed 'pipe-like' features. Waveforms between clusters also show a high degree of similarity, suggesting that each cluster is generated within the same source material, although we cannot determine from the depth distribution alone whether this is the ice, the interface or the bed material. For example, cluster 1 (Figure 3.2a) is one that appears to be located at the ice-bed interface, whereas cluster 2 (Figure 3.2b) appears to be located within the ice, yet the waveforms of events within these two clusters are very similar.

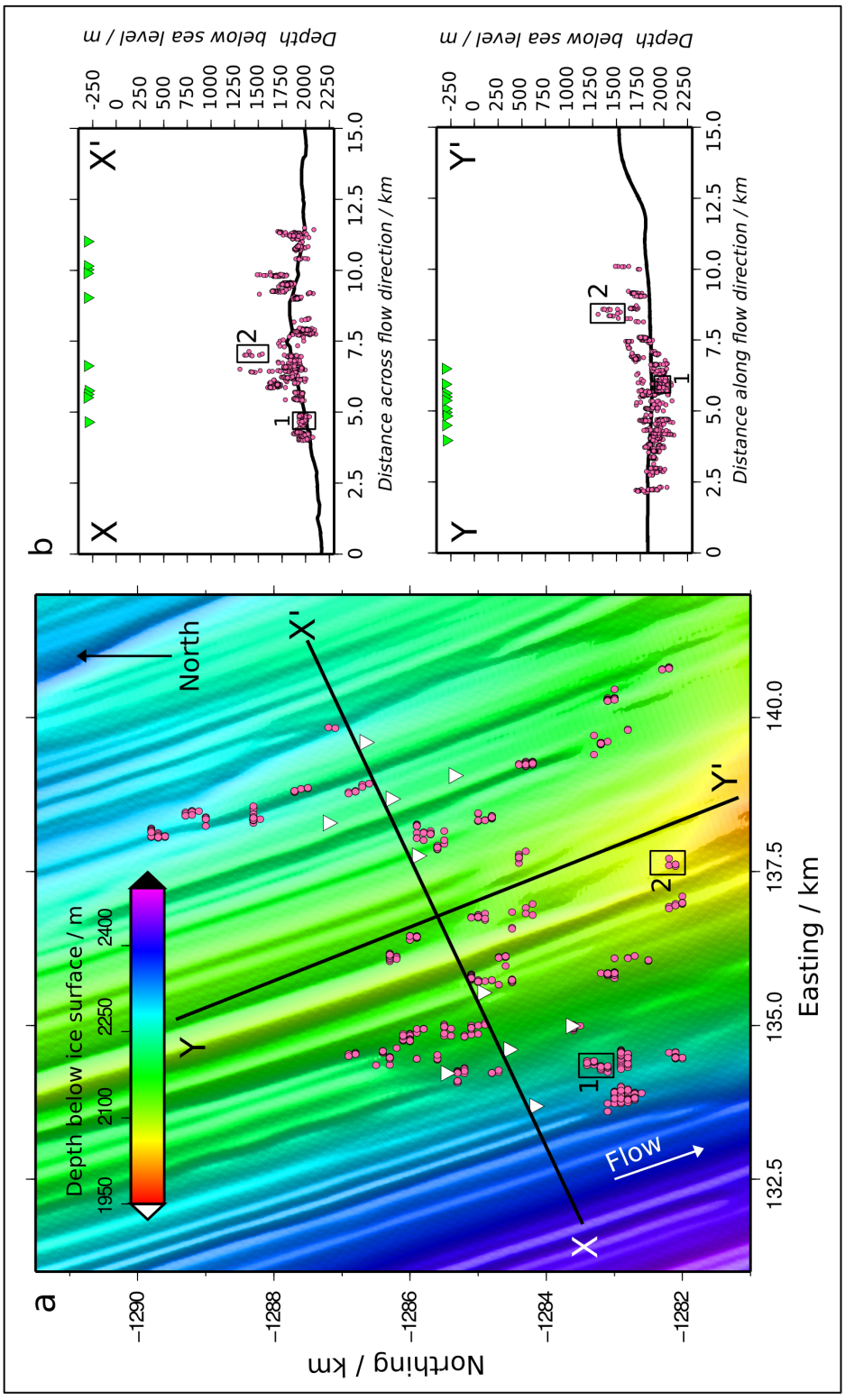

Figure 3.1: ***Location of 2967 basal seismic events.*** *a) Map view of event locations (pink) showing spatial clustering, many events are overlayed on top of each other. Seismic stations are shown in white and the coloured underlay is the depth of the ice-bed interface below the ice surface determined from RES. Timing and waveforms of clusters labelled 1 and 2 are investigated in Figure 3.2. b) Vertical profile across flow direction X-X' (top) and along flow direction Y-Y' (bottom) showing events in vertical 'pipe-like' features. Events are in pink and stations in green, the black line marks the ice-bed interface from RES data. All events are projected onto a profile through the ice-bed interface, therefore the interface shown may not be accurate for events far from the profiles.*

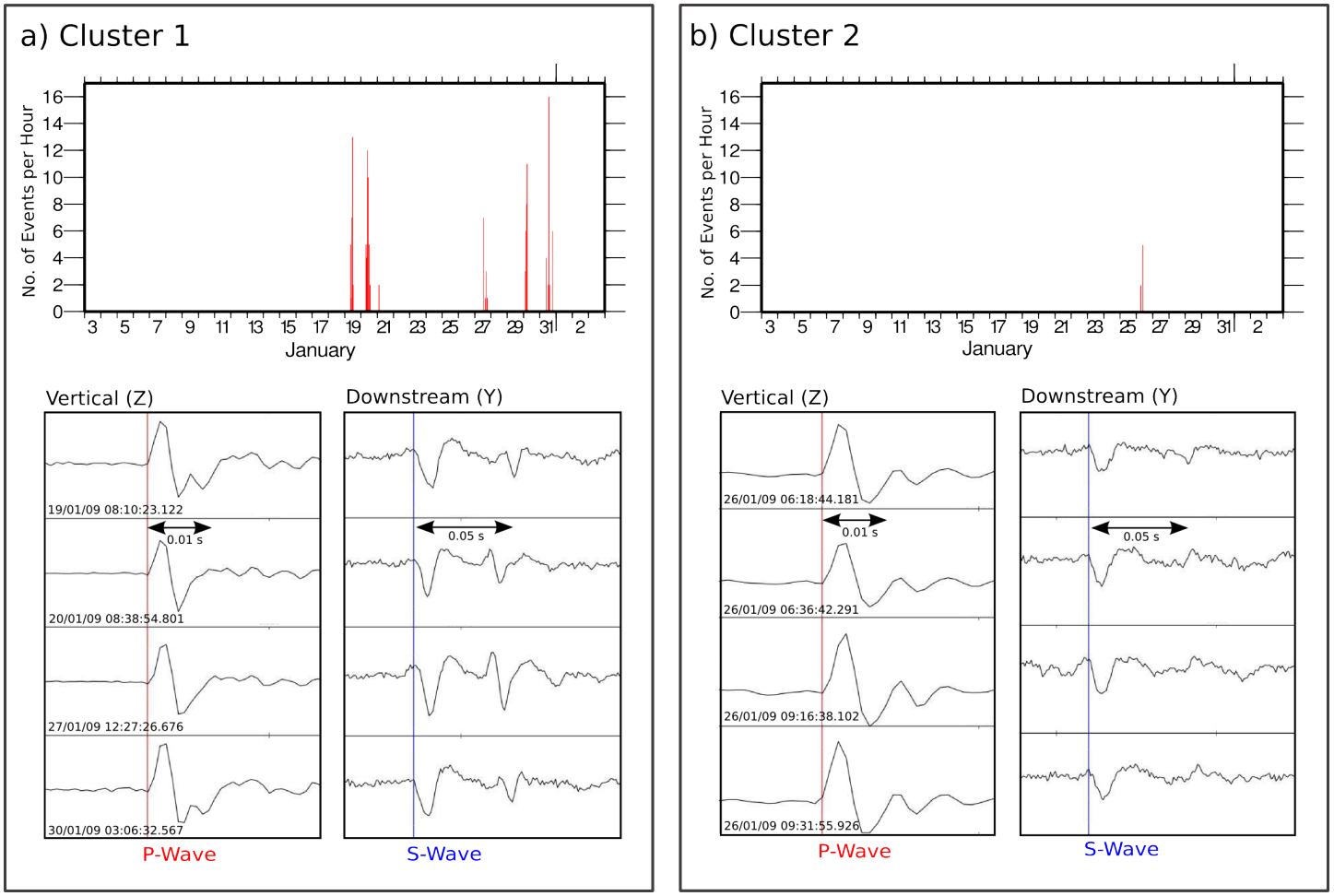

Figure 3.2: ***Characteristics of location clusters.*** *Top row: A single cluster turns on and off over the recording period. Bottom row: Waveforms at a single station for events within a cluster show a high degree of similarity, suggesting that the source of seismicity is the same for all events within one cluster. a) Cluster 1 - highlighted in Figure 3.1. Cluster consists of 101 events, waveforms for 4 of these events show a high degree of similarity, this is true for all 101 events. b) Cluster 2 - highlighted in Figure 3.1. Cluster consists of 7 events, waveforms for 4 of these events show a high degree of similarity. There is also a high degree of similarity between waveforms from the two clusters.*

Due to the presence of strong shear wave arrivals (e.g. Figure 2.4b), events cannot have originated from beneath a significant basal water layer; they are also unlikely to have come from a significant distance (more than 50 m) above the interface as we would expect to see reflected or converted arrivals after the primary P and S wave arrivals. The average duration of a P-wave arrival is ∼0.010 seconds. The travel-time difference for a P-wave that originates 50 m above the interface, at 4.5 km offset is 0.011 seconds (Figure 3.3) and so it is unlikely that a reflected arrival from this depth, or below, could be clearly distinguished from the primary arrival. Waveform modelling of primary and reflected waveforms has the potential to allow better constraints to be placed on event origin locations, however, 50 m can be seen as a maximum distance above the interface at which events could have originated without clear reflections being seen. For the majority of events the primary P-wave is not clear beyond 4.5 km offset and so any reflected arrivals beyond this offset would be not clear either.

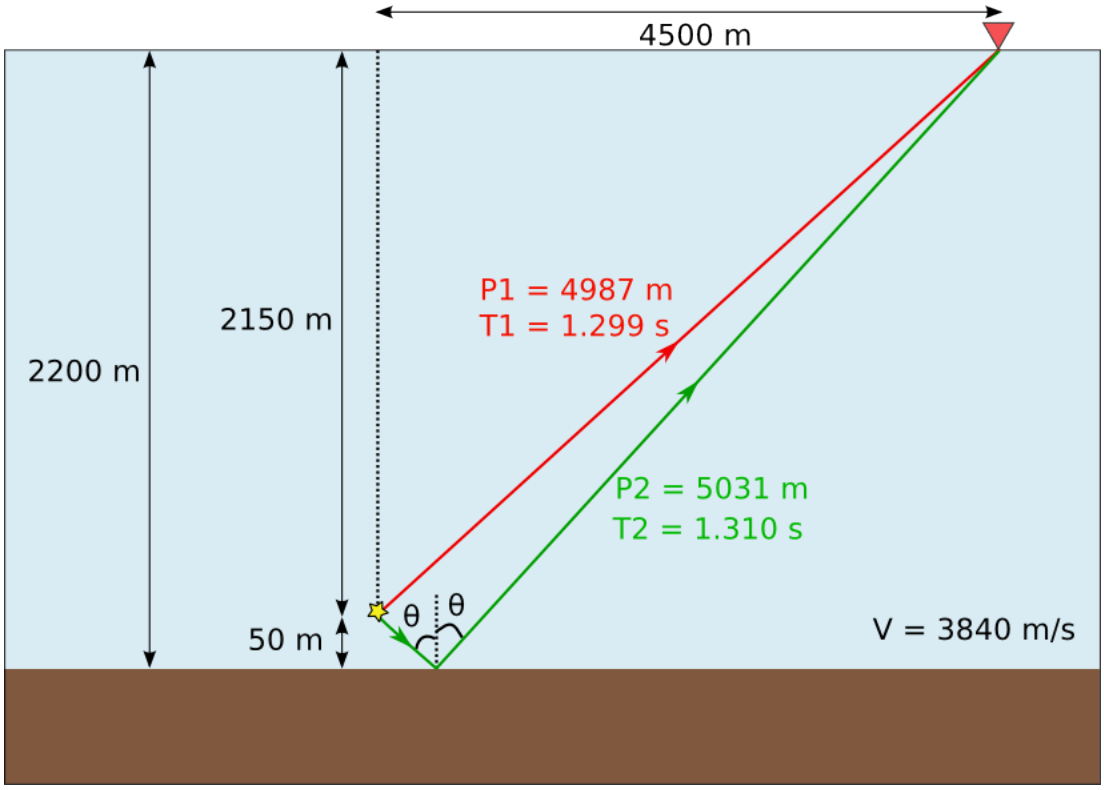

Figure 3.3: ***Schematic of the travel times and distance for direct and reflected arrivals from events that originate 50 m above the bed.*** *The path of the direct arrival is shown in red and the reflected arrival in green. An average ice thickness of 2200 m and an average P-wave velocity of 3840 ms^{-1} was used.*

3.3 Synthetic Testing of Location Uncertainty

There are many factors that affect the accuracy of microseismic event locations. The likely errors in this specific survey are: errors in picking the onset time of a phase (P- and S-wave), inaccuracies in the chosen velocity model and the coverage of the survey area by the station geometry. Understanding how each of these factors affects the hypocentral location is important in assessing the limitations of these data.

Hypocentral locations in the survey area appear to originate from 'pipe-like' features, spanning the ice-bed interface region (Section 3.2). Events have been located within the ice, within the bed and at the interface between them. It has also been observed that the waveforms of events are very similar within location clusters and indeed across the whole survey area, suggesting that events have a common mechanism. The disparity between these two observations can be explored using synthetic tests. I have designed two different sets of tests to explore the effect of the survey geometry (Section 3.3.2) and errors in the chosen velocity model (Section 3.3.3) on event locations. The synthetic tests also take into account random picking errors in both cases.

3.3.1 Method

In order to determine the resolution of the location method used I have performed a number of tests using NonLinLoc to generate synthetic seismic events with a known origin time and location. The P-wave and S-wave travel-times for each synthetic event to each station are calculated using the velocity model described in Section 2.4.1. Arrival times for each synthetic event then have a random Gaussian timing error added, to mimic a realistic mis-pick of up to 3 samples (i.e. 0.003 seconds) for P-wave picks and 5 samples (i.e. 0.005 seconds) for S-wave picks. These arrival times are then used to locate the synthetic events and derive output locations, following the same steps as used for the recorded data (Section 2.4).

3.3.2 Survey Geometry Testing

The number of stations in this study is small (10 stations) and covers a limited area with many events being located outside of the network of seismic stations (i.e. not directly below

either of the arrays). As a result of this many events in the survey have a limited range of ray inclinations and azimuths. Even for events inside the array the arrival-time differences and inclinations for an event recorded at each station are often very similar. All of these factors reduce the location accuracy, particularly the depth resolution, as there is a trade-off between the depth and origin time for a given event, due to the fact that both of these parameters are unknown.

The first test was designed to investigate the effect of this survey geometry on event locations, specifically whether this could be the cause of observed 'pipe-like' features. Fifty synthetic events were generated at the centre point of each of the location clusters observed in the recorded data, giving 2200 synthetic events in total. The yellow diamonds (Figure 3.4) show the true origin of the synthetic events.

When located using the same velocity model with which they were created the resulting distribution of synthetic arrivals exhibit a similar pattern to the recorded data, appearing to originate from vertical 'pipe-like' features crossing the ice-bed interface. These features become increasingly elongated towards the edges and outside the geophone arrays. Events at the downstream end of the profile Y-Y' show the greatest vertical elongation, as they are the furthest away from the geophone array.

For a single cluster, synthetic events all originated from a single point and were created and located with an identical velocity model. Therefore, the vertical spread in their apparent locations is probably a result of the survey geometry interacting with the arrival-time errors. When combined with the observation from the field data of nearly identical waveforms within a cluster (Figure 3.2), this is compelling evidence that the real events originate from discrete failure points associated with each individual cluster, rather than from across a significant vertical range. However, it does not answer the question as to where this discrete failure point may be.

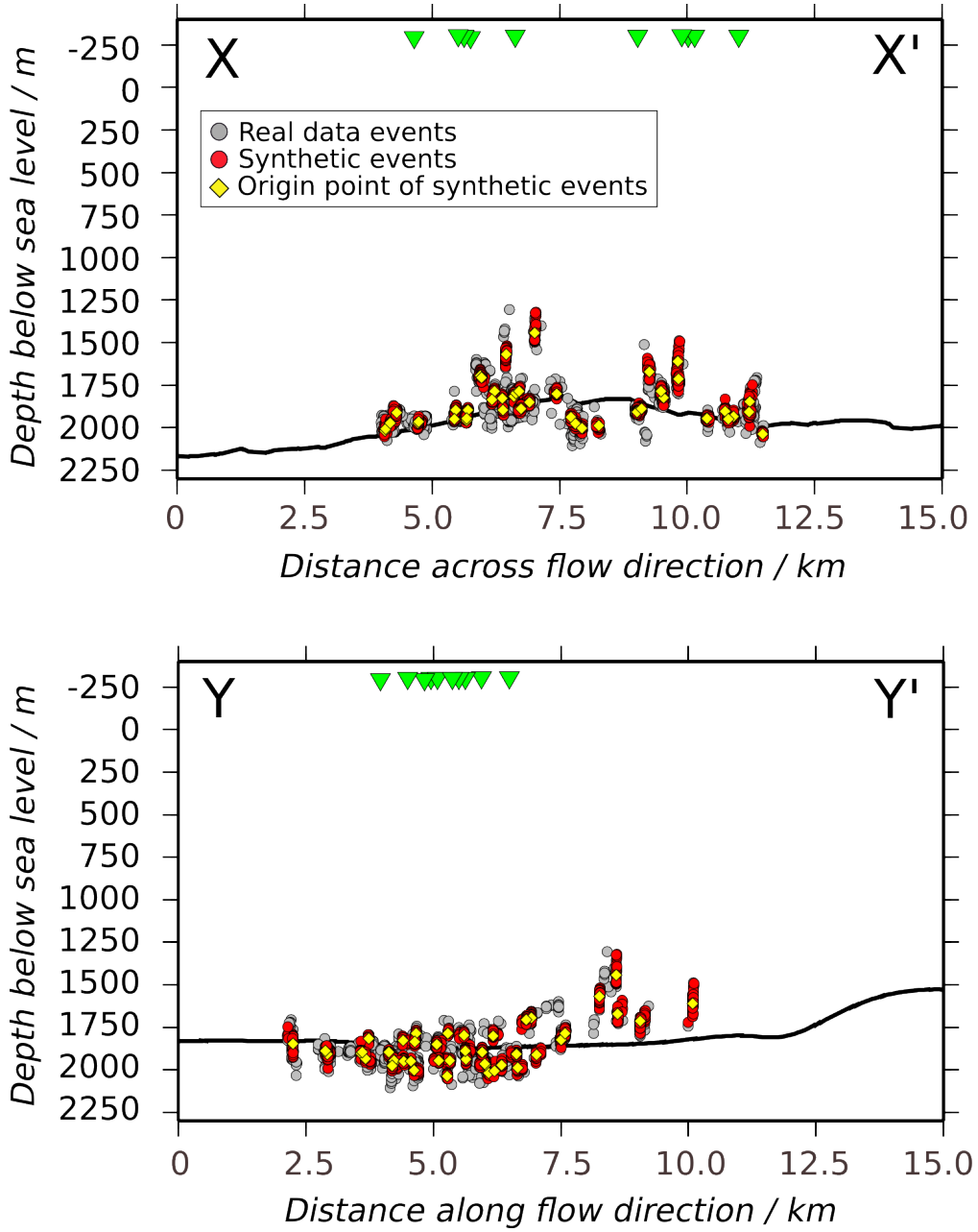

Figure 3.4: ***Testing the effect of survey geometry on depth location.*** *Real data events are shown in grey and are the same as those in Figure 3.1b, synthetic event locations are shown in red. Synthetic events originated from a single point at the centre of each cluster (yellow). When located with a small amount of random noise added to the time picks at each station they exhibit the same pattern as the real data, with an apparent origin in vertical 'pipe-like' features that straddle the ice-bed interface. These 'pipe-like' features become increasingly elongated outside the seismic array (seismic stations shown in green). This suggests that the same is true for the recorded data and that events within a single cluster originate from a single failure point. All events are projected onto a profile through the ice-bed interface, therefore the interface shown may not be accurate for events far from the profiles.*

3.3.3 Velocity Model Testing

The second suite of tests was designed to determine whether velocity model errors could account for the distribution of clusters in the ice, in the bed and at the interface and whether this spatial distribution is likely to be a real feature. In many survey settings (i.e. on land rather than ice) near surface layering varies significantly between stations and can have a large effect on the local seismic velocities around a station. Throughout this survey area the thickness of the near surface firn layer does not vary significantly and the surface elevation difference between stations is only a few metres, therefore, near-surface effects are unlikely to play a significant role and are not examined further here.

As with the previous test, clusters of 50 synthetic events were created but this time at the ice-bed interface underneath each of the recorded data clusters. This will be used to test the case that events originating at the interface could appear to locate in the pattern observed in the real data, given a reasonable error in the velocity model used to locate them. These synthetic events were then located with velocity models that varied from +5% to -5% (Figure 3.6) of the velocity model they were created with and also located with velocity models that had a Vp:Vs ratio of 1.9 and 2.0 (Figure 3.5) - 0.05 lower and higher respectively than the velocity model with which they were created, just over 1 standard deviation (σ) of the mean Vp:Vs ratio of 1.95 measured for the survey (see Section 2.4.1).

Figure 3.5 shows the effect of changing the Vp:Vs ratio. Locating events with a velocity model with a lower Vp:Vs ratio (1.9) than the one they were created with causes events to be located deeper than their point of origin (the ice-bed interface) across the survey area (red events in Figure 3.5a). Conversely, locating events with a velocity model with a higher Vp:Vs ratio (2.0) than the one they were created with causes events to be located shallower than their point of origin across the survey area (red events in Figure 3.5b). Neither of these patterns fits the observed data (grey events), which shows some events being located above the interface and some below.

Figure 3.6 shows the effect of changing the overall velocity model by +5% and -5%, with respect to the model the synthetic events were created with. Using a velocity model 5% lower to locate events causes them to be 'pulled up' (Figure 3.6a) and located above their point of origin in the centre of the survey (underneath the station array) and 'pushed down' and

located below the point of origin outside of the arrays, with this effect increasing with distance from the station array. Using a velocity 5% higher to locate events causes the opposite with 'push down' in the centre of the array and 'pull up' at the edges (Figure 3.6b). Locating events with a higher velocity best fits the pattern of synthetic data (red) to the observed data (grey), however +5% appears to cause too much 'pull up' at the edges of the survey area. Further testing showed that using a velocity model 3% higher (Figure 3.7) than that with which the synthetics were created best fits the locations of the observed data events. This illustrates the situation where the chosen velocity model for locating events is higher than the "true" seismic velocity model.

In Figure 3.7, the majority of synthetic events exhibit a similar pattern to the recorded data with event clusters outside the geophone arrays being located upwards and outwards from their true position. The effect is increased with increasing distance and hence increasing angle of arrival at the geophones. This suggests that a small velocity model error combined with a small arrival-time pick error is a likely explanation for this vertical pattern of event clusters. Being able to replicate the pattern of observed data for the majority of events suggests that in most cases the observed microseismic events are likely to be from the ice-bed interface, despite appearing to be located within the ice towards the edges and outside of the geophone array.

A small number (19 events) of locations that appear to be within the ice, around 300 m above the bed, cannot be explained by these tests (events inside the blue circle in Figure 3.7 and inset on Figure 3.8). Closer inspection of these events shows that the time picks are good and that the waveforms, source mechanisms and Vp:Vs ratios are similar to the other events within the survey (Figure 3.8).The waveforms show no evidence of reflections or converted arrivals from the ice-bed interface, which would be expected $\sim$0.07 sec after the primary P-wave arrival for events 300 m above the bed (Figure 3.8). Seismic reflection studies conducted in this area (see Section 1.4.2) confirm that the impedance contrast between the ice and various underlying sediment types in this region would produce good reflections at a range of angles of incidence. There is no simple conclusion as to whether these events truly originate from within the ice: they are in an area where the ice stream bed topography rises sharply and it remains possible that there is englacial (in ice) seismicity associated with this or a local velocity heterogeneity caused by this.

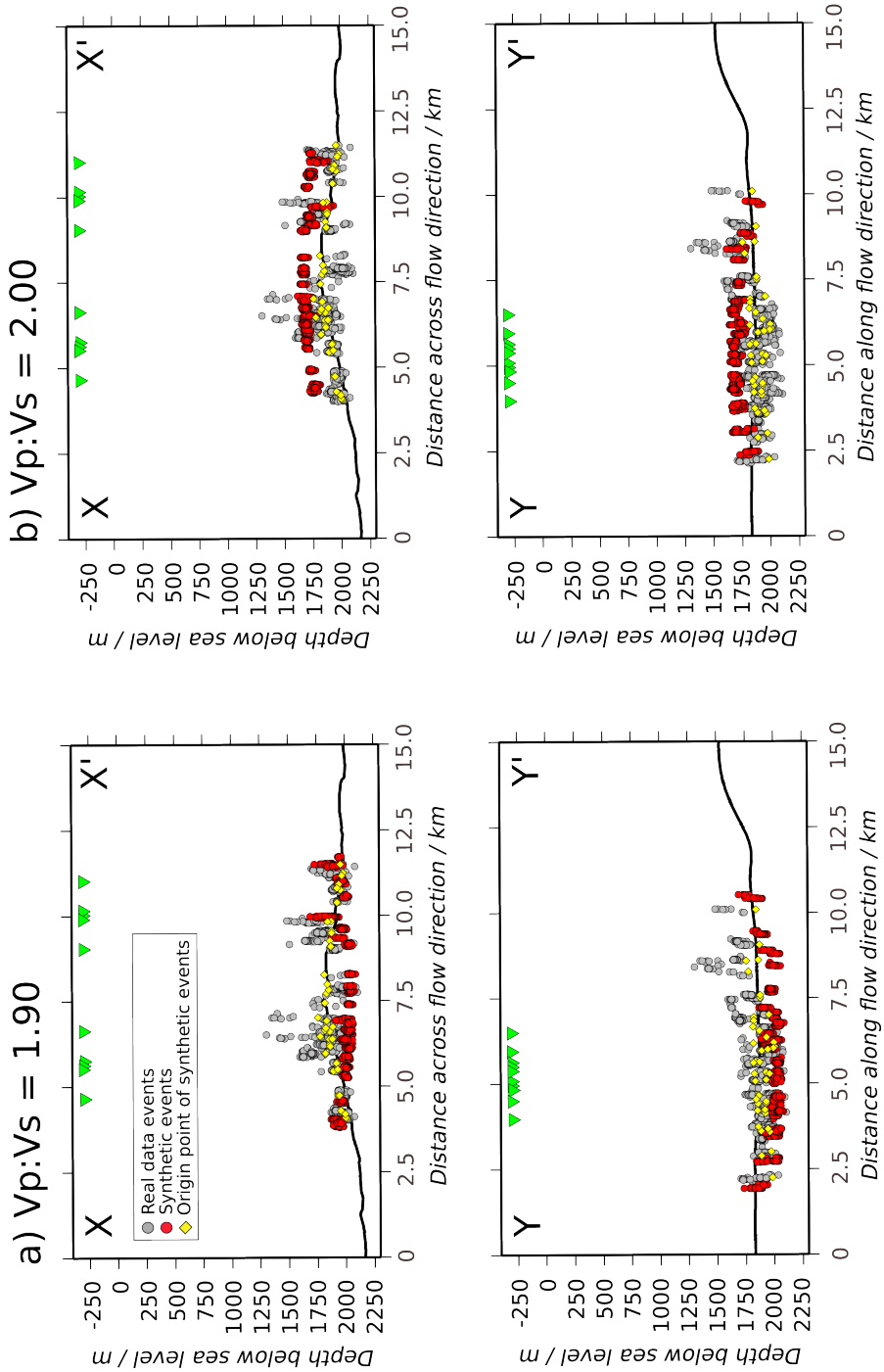

Figure 3.5: ***Testing the effect of velocity model error on event location - varying Vp:Vs ratio.*** *Real data events are shown in grey and are the same as those in Figure 3.1b, synthetic event locations are shown in red. Synthetic events originated from the ice-bed interface directly underneath each cluster, origin points are shown in yellow. The ice-bed interface (black line) is a 2-D profile taken through the 3-D interface shown in Figure 3.1a, therefore, some of the yellow diamonds do not appear to plot at this interface because they are off this profile. a) When synthetic events are relocated with a Vp:Vs ratio of 1.9 events are located deeper (red circles) than their point of origin (yellow diamonds). b) When synthetic events are relocated with a Vp:Vs ratio of 2.0 events are located shallower (red circles) than their point of origin (yellow diamonds). Neither pattern in the synthetic data (red) fits the observed data (grey) well.*

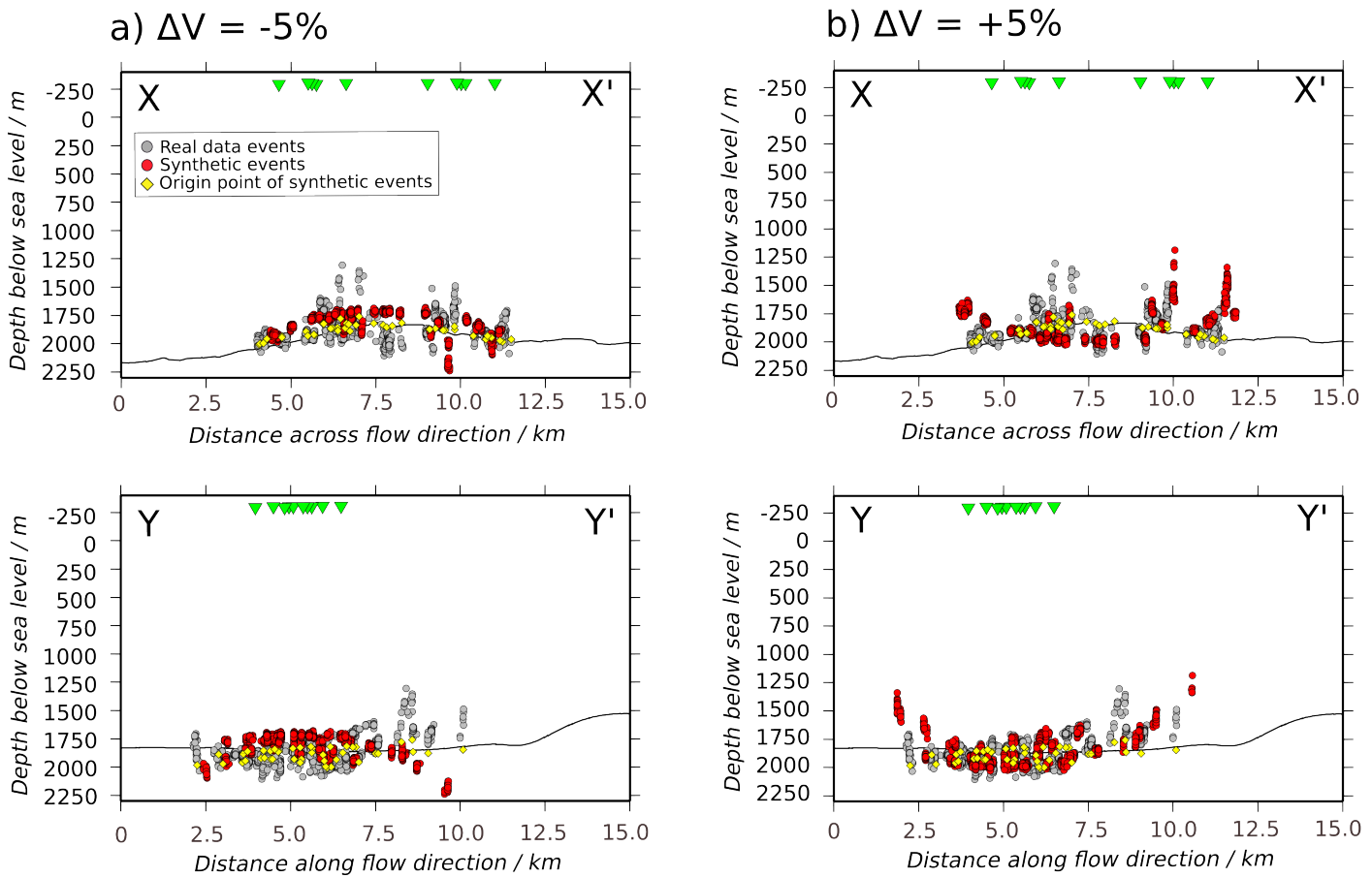

Figure 3.6: ***Testing the effect of velocity model error on event location - varying overall velocity model.*** *Real data events are shown in grey and are the same as those in Figure 3.1b, synthetic event locations are shown in red. Synthetic events originated from the ice-bed interface directly underneath each cluster, origin points are shown in yellow. The ice-bed interface (black line) is a 2-D profile taken through the 3-D interface shown in Figure 3.1a, therefore, some of the yellow diamonds do not appear to plot at this interface because they are off this profile. a) When synthetic events are relocated with a velocity model 5% lower than that with which they were created the locations are 'pulled up' with respect to their point of origin (yellow diamond) in the center of the survey area and 'pushed down' at the edges. b) When synthetic events are relocated with a velocity model 5% higher than that with which they were created the locations are 'pushed down' with respect to their point of origin (yellow diamond) in the centre of the survey area and 'pulled up' at the edges. The pattern of events locations seen in (b) best fits the pattern in the observed data but 'pull up' at the edges is too much.*

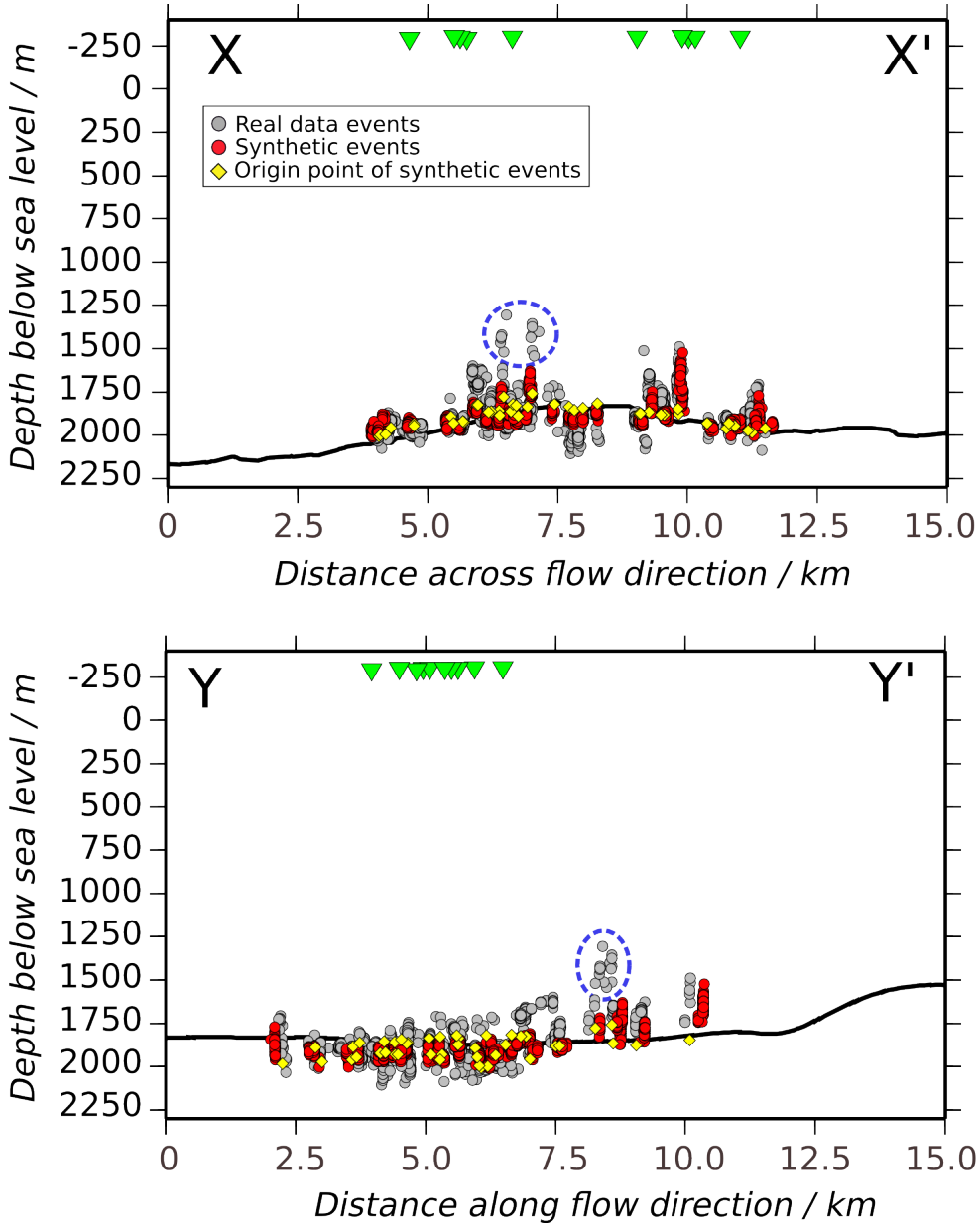

Figure 3.7: ***Testing the effect of velocity model error on event location - best fit synthetic model.*** *Real data events are shown in grey and are the same as those in Figure 3.1b, synthetic event locations are shown in red. Synthetic events originated from the ice-bed interface directly underneath each cluster, origin points are shown in yellow. The ice-bed interface (black line) is a 2-D profile taken through the 3-D interface shown in Figure 3.1a, therefore, some of the yellow diamonds do not appear to plot at this interface because they are off this profile. When synthetic events are relocated with a small amount of random noise and a velocity 3% higher than that with which they were created, the majority of them exhibit the same pattern as the real data. This suggests that events that appear in the ice could have originated from the ice-bed interface, with the exception of the events circled in blue.*

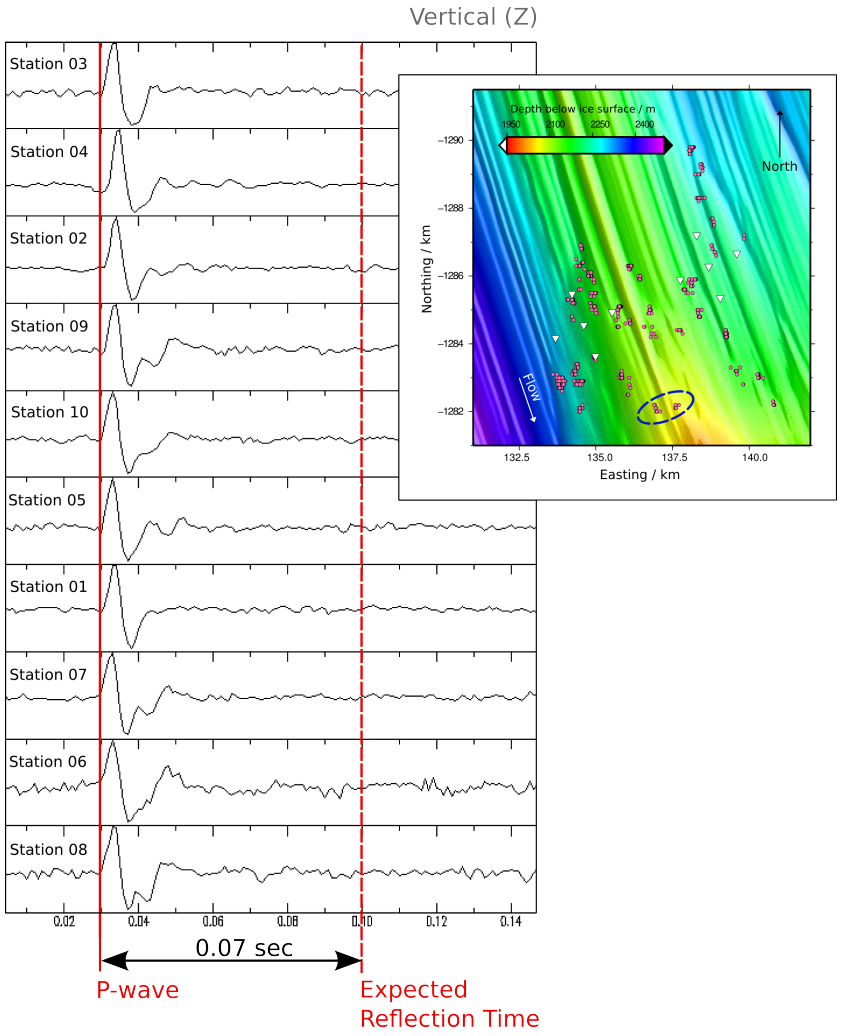

Figure 3.8: ***Waveforms for an event that appears to be 300 m above the bed.*** *Stations are in order of distance from the source, nearest at the top. Event waveforms show no clear reflected arrivals from the ice-bed interface that would be expected if the events were truly located in the ice, 300 m above the bed. There is no evident movement of a particular phase with increasing distance from the source, as would be expected for a reflected arrival. Inset: Map view of the clusters that appear 300 m above the bed (circled), they comprise a total of 19 events.*

3.3.4 Vertical and Horizontal Resolution

For a given synthetic cluster all events originate from the same point and so the distance of their apparent location from this origin point indicates the magnitude of errors expected from the location method. By looking at the location spread of a cluster of 50 synthetic

events in the centre of the survey area from the first test, the best resolution of the location method with the given array configuration is ±20 m in the horizontal direction and ±32 m in the vertical. Looking at the location spread for a cluster of 50 synthetic events at the edge of the survey area the horizontal resolution is ±33 m and the vertical resolution ±98 m. This result highlights the decrease in vertical resolution towards the edge of the survey area, outside the station array, compared to the horizontal resolution, which does not decrease a great deal with distance from the stations. The horizontal error in event locations is of a similar order to the total movement of the sensors on the surface of the ice stream during the 34-day recording period (∼35 m); I have not corrected for the daily motion of recording stations so this effect is incorporated within the errors.

3.3.5 Implications for Source of Seismicity

This analysis highlights the poor resolution of the depth location of events from this array configuration and the sensitivity of location to the velocity model. Caution must therefore be exercised when using event depth to inform the exact source of seismicity with respect to the ice-bed interface. It is likely that events come from the ice-bed interface in most cases and that the appearance of events being located within the ice and the bed may be due to a small error in the chosen velocity model of +3%. If this is indeed the case, the source of the velocity model being used to locate the field data (see Section 2.4.1) being slightly faster than the "real world" model could be due to the presence of warm ice near the base of the ice stream, which would have a slower seismic velocity than the cold ice velocity used in the velocity model to locate events in this study. It should also be noted that the seismic velocity of ice can be highly anisotropic (see Chapter 5). Therefore, the use of an isotropic velocity model in this study will introduce some location error. Synthetic testing has allowed us to explore possible explanations for the disparity between observed event locations being in vertical 'pipe-like' features but also having near identical waveforms within a cluster and between clusters.

3.4 Temporal Analysis

A temporal view of the 2967 good quality events observed over the 34-day recording period (Figure 3.9) does not show a clear progression of seismicity in a given direction (up or

down stream) or a clear change in depth over time. The seismicity occurs in bursts at a particular cluster location but there is no indication that there is a temporal pattern in cluster activation. A histogram of the total seismicity over time (Figure 3.10) shows there is no regular periodicity or event rate cyclicity. There is a noticeable lack of events between 14^{th} and 16^{th} of January (highlighted in grey, Figure 3.10), this is due to data drop out on 5 stations during this time period.

In this area the surface flow velocity of Rutford Ice Stream varies due to stress transmission of tidal forcing upstream of the grounding line (see Section 1.4.2). This variation is dominated by a periodic cycle of 14.77 days, causing a surface velocity variation along flow of around $\pm 10\%$ (*Gudmundsson*, 2006; *Murray et al.*, 2007). It would follow that the changing basal stress causing this velocity variation might be visible in the levels of basal seismicity. *Adalgeirsdóttir et al.* (2008) observed that in this area of Rutford Ice Stream the highest levels of basal seismicity correlated with spring tides, when the velocity is highest, and that there are often two peaks in both seismicity and velocity during a semi-diurnal tidal cycle. Figure 3.10 shows no apparent correlation between the overall levels of seismicity and the dominant fortnightly spring/neap variation in surface velocity of the ice stream, determined from the surface GPS station. In fact, the highest levels of overall seismicity occur between January 18^{th} and 22^{nd}, during a low surface velocity period.

It is not clear why our observations of event timing differ from the findings of *Adalgeirsdóttir et al.* (2008). It may be related to considerable differences in the event detection and location methods between the two studies, although it is clear in both cases that events are from the ice-bed interface region. The microseismic data presented by *Adalgeirsdóttir et al.* (2008), from a study by *Smith* (2006), were acquired using different recording equipment and acquisition parameters than the data presented here, particularly in station spacing, geophone response and logger sampling rate. They also used a simpler and very different event detection method. The field data recorded by *Smith* (2006) was triggered by high amplitude P-wave arrivals only; and event identification in post-processing was based only on a count of the number of events detected at each individual station within an array, rather than the detection of coherent energy across a number of stations as used in this study. It is therefore possible that the different methods used resulted in different sub-sets of the total microseismic activity being selected in the two different studies. It also remains possible that the dynamics of this area have changed over the time between these two studies.

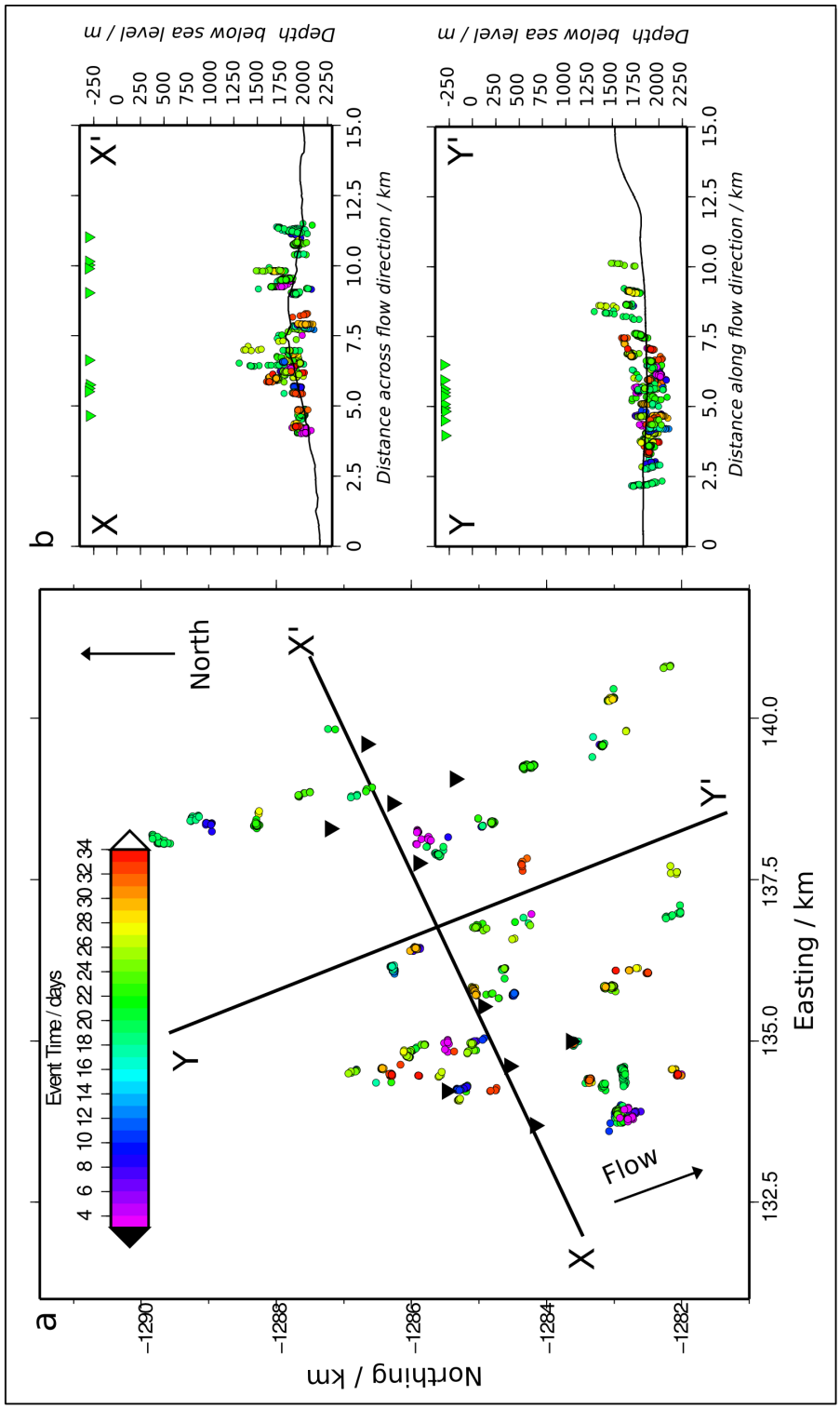

Figure 3.9: *Location of basal seismic events coloured by time.* *Blue and purple events were recorded at the start of the 32-day period and red and orange events at the end. There is no clear pattern in event timing with no progression of events within a cluster up or down stream and no clear change in depth of events over time. a) Map view of event locations coloured by time. b) Vertical profile across flow direction X-X' (top) and along flow direction Y-Y' (bottom) showing events coloured by time.*

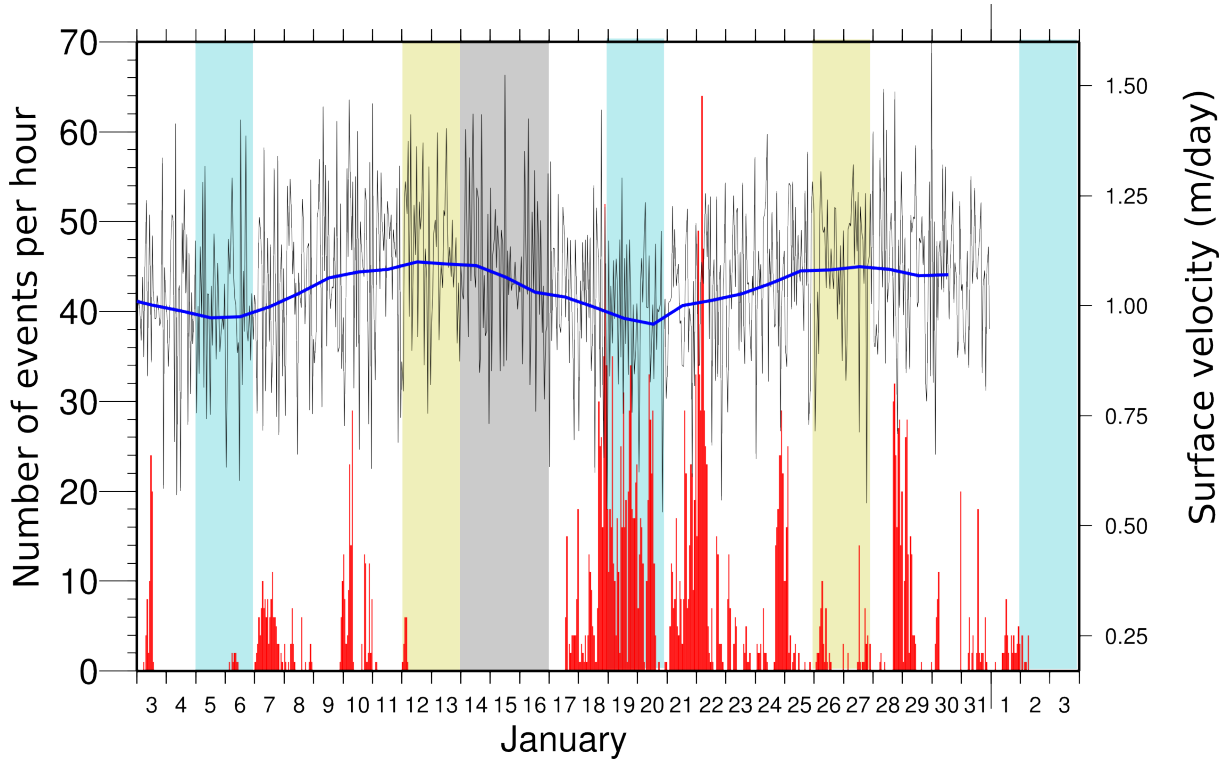

Figure 3.10: ***Histogram of the 2967 good quality events observed over the 32-day recording period.*** *Events (red) are binned in number of events per hour (left axis) and the surface flow velocity of the ice stream (right axis) determined from surface kinematic GPS data is also shown. The surface flow velocity is calculated once per hour (black). The blue line highlights the long wavelength cyclicity of 14.77 days, spring tides at the grounding line are highlighted in yellow and neap tides in blue (S. Rosier, personal communication). The area highlighted in grey shows the period of data drop out on 5 stations. The level of seismicity through time shows no clear pattern relating to the changing surface flow velocity.*

3.5 Discussion

The spatial pattern of seismicity from the base of Rutford Ice Stream shows that events are located in discrete spatial clusters near the ice-bed interface. The discrete cluster locations show repeated failure over time with a near identical waveform observed for each event that happens at a given cluster location. It is not possible to tell from the depth resolution of these data exactly where the seismicity originates, although hypocentres do locate within the vicinity of the ice-bed interface. The presence of strong shear wave arrivals means events cannot have travelled through a significant amount of water beneath the ice, and the absence of reflected or converted arrivals indicates that they did not originate more than 50 m above

the ice-bed interface.

Synthetic testing shows that events within a cluster are likely to come from a single failure point and that the vertical smearing of event locations across the ice-bed interface can be explained by the survey geometry combined with small picking errors in waveform arrival times. I also showed that for synthetic events originating at the ice-bed interface a small error in the seismic velocity model of +3% can be used to explain the observed pattern of hypocentral locations within the ice, in the bed and at the interface. I therefore conclude that the discrete failure point for each cluster is most likely to be at the ice-bed interface, rather than in the ice or in the bed. One possible exception to this is the small number of events that appear to originate within the ice (Figure 3.7 and Figure 3.8), although the fact that their waveforms, source mechanisms and Vp:Vs ratios are similar to the other events within the survey suggests that even these events may actually still come from the ice-bed interface.

These observations are consistent with microseismic clusters located at 'sticky spots' at the ice-bed interface where Rutford Ice Stream is moving by basal sliding of ice over a stiff consolidated subglacial sediment, accompanied by seismic failure. It therefore follows that areas outside these 'sticky spots' are accommodating ice stream motion aseismically, probably by pervasive deformation of dilatant sediments underlying Rutford Ice Stream or by sliding over a well-lubricated, stiff bed. From a preliminary passive seismic survey in this area, *Smith* (2006) concluded that parts of the ice stream likely to be moving by basal sliding showed levels of seismicity six times greater than those moving over a deforming bed. This conclusion was drawn from a simple count of the number of events detected at stations situated over the two different bed types, previously determined by seismic reflection surveying, and locations of seismic events were only weakly constrained. This study gives much better constraint on the location of basal seimsic events and shows the ice-bed interface region to be much more complex with a distributed pattern of seismic and aseismic areas.

It has been shown that a strong (±10%) periodic variation in ice surface flow velocity in this area is caused by tidal forcing (*Murray et al.*, 2007; *Gudmundsson*, 2006). This indicates that a strong periodic variation in basal stresses, resisting ice flow, exists. Therefore, a reflection of this in the levels of basal seismicity would also be expected, as has been demonstrated on other Antarctic ice streams (*Anandakrishnan and Alley*, 1997). The lack of this correlation between surface velocity and basal seismicity levels in Rutford Ice Stream indicates that the

'sticky spots' in this area are unaffected by changes in basal stress. It could also suggest that it is the material outside the 'sticky spots', that I have suggested is deforming aseismically, which is subject to alterations in stress due to tidal forcing. *Thompson et al.* (2014) and *Rosier et al.* (2015) have suggested a mechanism for the transmission of stresses upstream of the grounding line by tidally modulated changes in subglacial sediment pore pressure, causing a slow down or speed up of the ice stream. This model is consistent with my suggestion that changes in the aseismic dilatant sediments are responsible for surface velocity changes and that the 'sticky spots', formed of stiffer sediment, are not affected by these changes. This could explain why rates of seismicity on the 'sticky spots' do not change with changing surface velocity.

3.6 Conclusions

In this chapter I have used passive microseismic monitoring on Rutford Ice Stream to locate ∼3000 good quality basal seismic events over a 32-day period using an optimised automated detection and location process. Events are concentrated in spatial clusters that turn on and off over the recording period. The clusters are interpreted as occurring at 'sticky spots' of stiff sediment at the ice-bed interface, where ice movement is accommodated by stick-slip basal sliding. The overall levels of seismicity show no correlation with tidally modulated surface ice flow velocity variations, suggesting a possible mechanism for transmitting tidal stresses upstream of the grounding line is through changes in the pore pressure of the dilatant sediment. The location of microseismic events has allowed me to investigate the material characteristics of an ice stream bed and the basal dynamics that accommodate ice stream motion.

Chapter 4

Seismic Source Analysis

4.1 Introduction

Basal microseismic events are located in spatial clusters around the ice-bed interface (Chapter 3), however the resolution of locations alone is not sufficient to determine their origin. In this chapter, I investigate the source characteristics of the microseismic events described in Chapter 3, by constructing fault plane solutions to determine the type of failure causing the events. I also calculate event magnitudes and determine the likely fault geometry, and go on to link these together to look at the amount of basal shear stress accommodated by seismic deformation in this area. I discuss how the additional information about seismic sources can be used to provide a more robust interpretation of both the material characteristics at the bed of Rutford Ice Stream and the spatial and temporal basal processes that accommodate ice stream motion.

Parts of this chapter are included the following publication:

Smith, E. C., A. M. Smith, R. S. White, A. M. Brisbourne, and H. D. Pritchard (2015), Mapping the Ice-Bed Interface Characteristics of Rutford Ice Stream , West Antarctica, Using Microseismicity, *J. Geophys. Res. Earth Surf, 120*, 1881-1894, doi:10.1002/2015JF003587.

4.2 Fault Plane Analysis

In order to investigate the seismic source mechanisms that are responsible for generating basal microseismic events, fault plane solutions (FPS) were constructed for a representative event in each of the location clusters (see Chapter 3), using the first motion of P-wave arrivals at each station. The polarities at each station (compressional or dilatational) were plotted on a lower hemisphere stereographic projection. A double-couple model was assumed in order to separate the focal sphere into compressional and dilatational quadrants using two orthogonal nodal planes, the fault plane and the auxiliary plane, using the program FPFIT (*Reasenburg and Oppenheimer*, 1985).

It is not possible from the FPS alone to determine which of these nodal planes is the fault plane. Figure 4.1b shows a typical lower hemisphere FPS. The P-wave first motion polarity picks are of excellent quality and unambiguous. The most likely fault plane and auxiliary plane are marked, indicating a low-angled thrust fault slipping in the ice-flow direction. The alternative would be a near-vertical fault slipping across the flow direction, which is physically unlikely. Both compressive and dilatational arrivals are recorded, which eliminates the possibility of the events being from basal crevasses opening and closing (which would have the same polarity of arrival at all stations). The dip and strike of the fault plane are not tightly constrained. However, the slip vector to this plane is tightly constrained by the auxiliary plane, giving a consistent indication of low-angled slip in the ice-flow direction. Across the survey area there is a consistent source mechanism of low-angled (likely sub-horizontal) faulting, slipping within $\pm 10^{\circ}$ of the ice-flow direction (Figure 4.1). This further supports the conclusions drawn in Chapter 3 that the mechanism of failure for each location cluster is the same. It implies that events identified as originating from above the ice-bed interface in Section 3.3.5 could be at the interface, rather than within the ice. The pattern of low-angled faulting in the ice-flow direction is consistent with the findings of *Anandakrishnan and Bentley* (1993) on Kamb Ice Stream (formerly Ice Stream C), Antarctica.

The polarity of the FPS is consistent with an upper block moving southwards with respect to the lower block and suggests a mechanism of basal sliding of the upper block (glacial ice) over the lower block (basal sediments). This is consistent with the suggestion in Chapter 3 that location clusters represent 'sticky spots' of stiff basal sediment that accommodate the overlying ice stream motion by basal sliding accompanied by seismic failure.

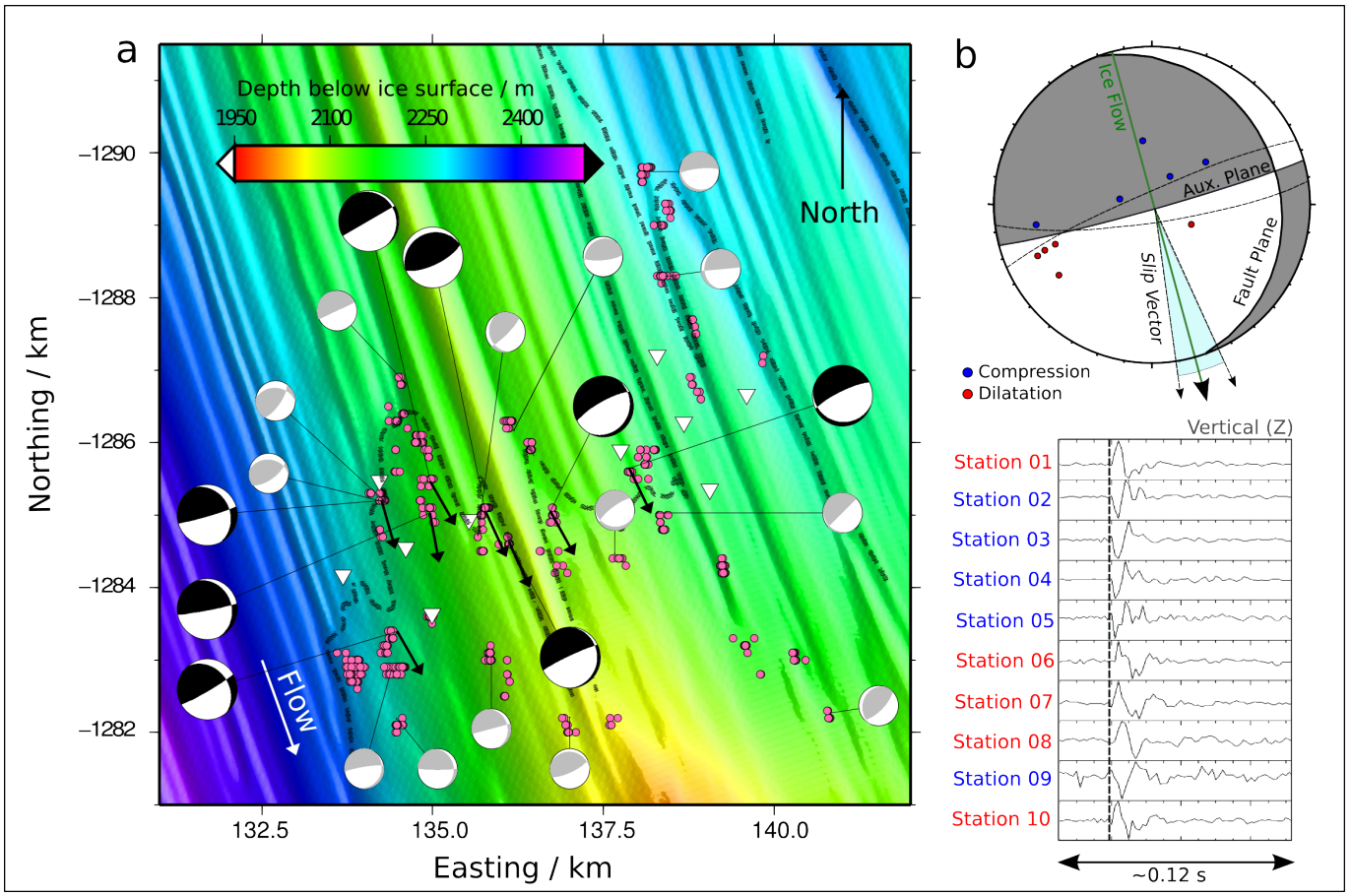

Figure 4.1: ***Fault plane solutions.*** *(a) Fault plane solutions for a representative event in each cluster, constructed by picking first motion P-wave polarities. Large black solutions are those that are well constrained and the corresponding slip vectors are shown (black arrows originating at cluster centres). Small grey solutions are less well constrained, but are shown for completeness. The pattern of low-angled faulting in the ice-flow direction is consistent across the survey area. The dashed line indicates the interpreted boundary between stiff basal sediment and dilatant basal sediment (G. Boulton personal communication), determined from independent studies of seismic reflection and radar data (Smith and Murray, 2009; King et al., 2009). Areas of seismicity largely coincide with the stiff basal sediment areas (south of the boundary) (b) A typical lower hemisphere fault plane solution (top), compressional quadrants (downwards trace deflection) are shaded. The dashed lines show the limits of the auxiliary plane and the corresponding region of possible slip vectors is shaded in blue. The fault plane is low-angled and its strike is not well constrained. The slip vector constrained by the auxiliary plane is well constrained and is in the ice-flow direction. P-wave polarities are clear and unambiguous (bottom).*

4.3 Event Magnitude

There are several scales typically used to define the magnitude of a seismic event. The first widely used magnitude scale was defined by Charles Richter in the 1930s and is now known as the local magnitude scale (M_L). Richter noticed that plotting the log of the largest recorded event amplitude ($\log_{10} Amp$) against epicentral distance (X), from the event to the seismometer, produced a decay curve that was of a similar shape for many different earthquakes. This meant that the size of an earthquake could be compared to other earthquakes in the area by determining the offset of the decay curve for a particular event from a reference event. This was later turned into an empirical formula (Equation 4.1).

$$M_L = \log_{10}(Amp) + 2.56 \log_{10}(X) - 1.67 \tag{4.1}$$

This specific scale is only valid for events recorded on a Wood-Anderson torsion seismograph in southern California at a range of $10 < X < 600$ km. However, the form of Equation 4.1 can be adapted to determine local magnitude scales for other specific areas. Other commonly used magnitude scales, based on measuring ground displacement or amplitude from seismographs, are the body wave magnitude (m_b) and the surface wave magnitude (M_s) scales: these are suited to global seismology problems and would not be suitable for a very localised study, such as this one.

Each of the scales described above (M_L, m_b and M_s) allow us to compare earthquakes. However, they do not give a measure of the size of an earthquake that is directly related to the physical properties of the earthquake source. The seismic scalar moment, M_0 (*Aki and Richards*, 2002), is given by Equation 4.2 where μ is the shear modulus, D is the fault displacement, and A is the fault area. It is the basis of the moment magnitude (M_w) scale (Equation 4.3, *Hanks and Kanamori*, 1979)

$$M_o = \mu A D \tag{4.2}$$

$$M_w = \frac{2}{3} \log_{10}(M_0) - 6 \tag{4.3}$$

I have developed a local magnitude scale for this study area on Rutford Ice Stream (M_R) using Equation 4.4, which follows the general form of magnitude scales (e.g. Equation 4.1). This has then been tied to the moment magnitude (M_w) for a typical event in order to allow derivation of the source characteristics of the microseismic events from the base of Rutford Ice Stream.

$$M_R = \log_{10}(Amp) + 0.21x - 4.69 \tag{4.4}$$

For each event the maximum amplitudes (in instrument counts) of the clear P-wave arrivals at each station were measured (Amp) and a distance correction (in km) to account for the hypocentral source to receiver distance (x) was added. The distance correction term $0.21x$ was derived by linear regression of the relationship between x and $\log_{10}(Amp)$ for each event within the survey (an example of one of these is given in Figure 4.2) and a mean distance correction was calculated from all events with an R-squared value (r^2) > 0.4 (threshold determined by visual inspection of a range of results).

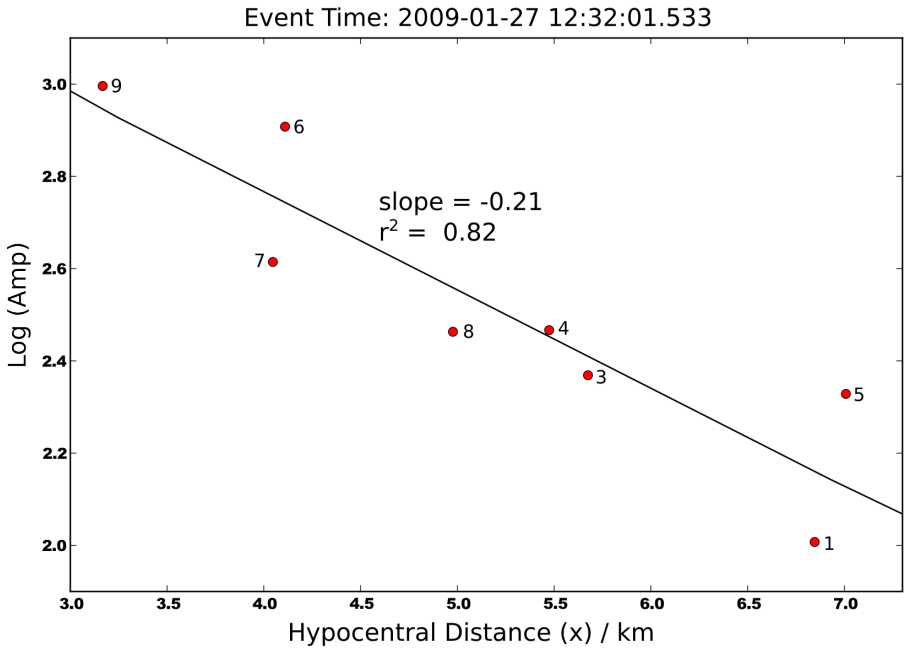

Figure 4.2: ***Determining the distance correction term from a linear regression of x and $\log_{10}(Amp)$***

The mean of the M_R measurement at each station was taken to calculate the final M_R for an event. A scaling factor of -4.69 was determined by comparing the value of M_R to a value of the seismic scalar moment (M_w) determined for the same event and serves to tie the two scales at this point.

The value of M_w for a typical event was calculated by A. Brisbourne (personal communication, 2014) using the implementation by *Walter et al.* (2009) of the linear time domain moment tensor inversion scheme used by *Dreger et al.* (2000) and *Dreger and Woods* (2002) to determine M_0 for that event. Green functions were computed using the F-K software developed by *Zhu and Rivera* (2002). The 1D velocity model used in the event location was employed with seismic quality factor $Q_p = 350$ (*Peters et al.*, 2012). Although fault plane orientations are not well constrained by the inversion, due to poor focal sphere coverage, the scalar moment is robust and varies little when different numbers of stations are included (A. Brisbourne, personal communication, 2014). The seismic moment (M_0) for this single microseismic event is $6\text{x}10^6$ Nm giving a moment magnitude of M_w = -1.48 (using Equation 4.3). An estimate of the seismic scalar moment for a second event was determined to provide a validation of the M_R magnitude scale. A value of M_w = -0.69 was determined, compared to a value of M_R = -0.89 for the same event.

A histogram of the magnitudes for all events (Figure 4.3) displays a range of -1.77 $< M_R <$ -0.67. The drop-off in number of events with $M_R <$ -1.43 is typical and is due to event detection limits of smaller magnitude events. The upper magnitude limit, M_R = -0.67, equates to a maximum seismic moment of $M_0 = 9.6\text{x}10^7$ Nm. This is significant as it suggests this is the maximum amount of energy that can be released by this type of seismic failure at the base of Rutford Ice Stream. The magnitude distribution appears to have a double peak with events with $M_R > -0.9$ in one peak and events with $M_R < -0.9$ in another.

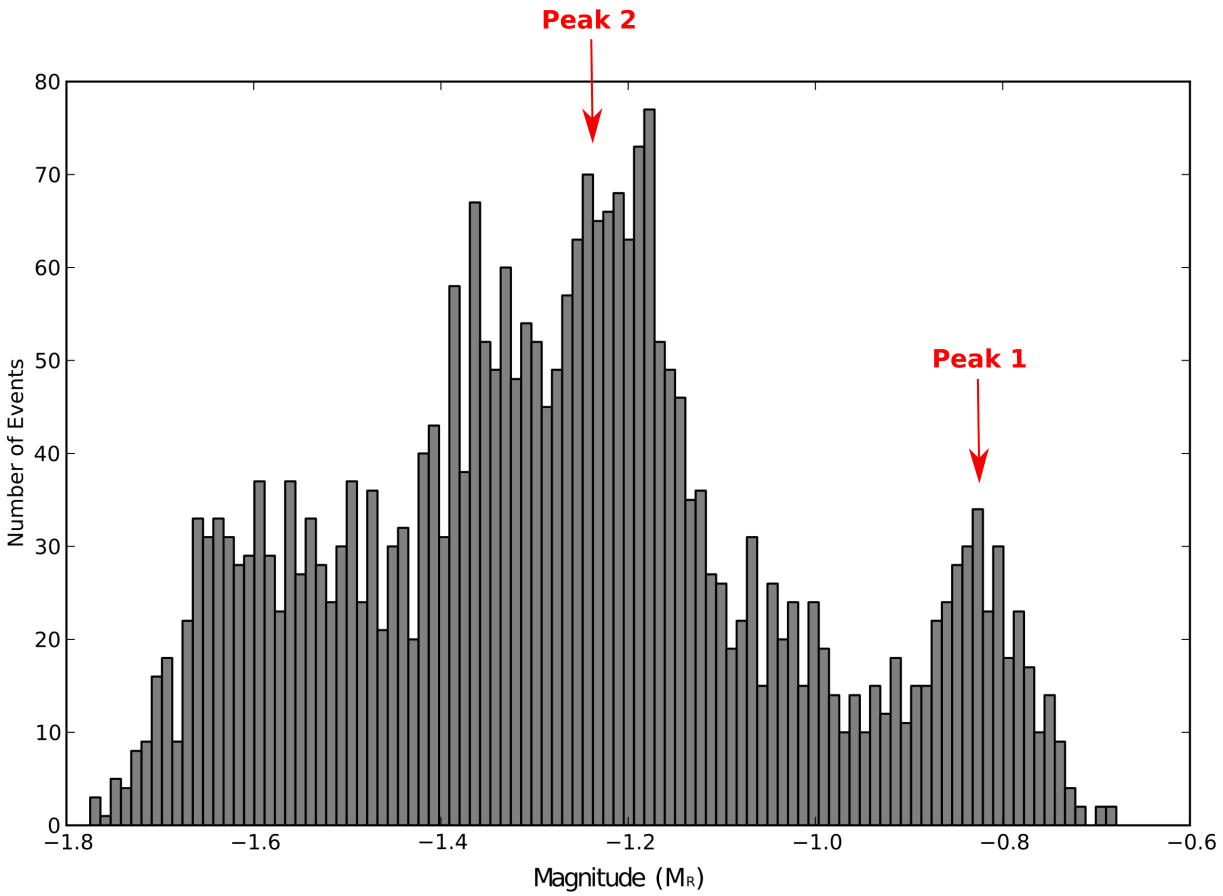

Figure 4.3: ***Histogram of the magnitudes (M_R) of the 2967 good quality events observed over the 32-day recording period.*** *Events are binned at intervals of 0.01. The tail off of events with $M_R <$ -1.48 is typical and due to the limitation on detecting smaller magnitude events. The upper limit of magnitude M_R = -0.67 suggests a maximum seismic moment of M_0 = 9.6x10^7 Nm. The distribution appears to show a double peak.*

In general, for a given region, one would expect to find more small seismic events than large ones. The seismic b-value, defined by *Gutenberg and Richter* (1944) relates the size of earthquakes to the frequency of occurrence using Equation 4.5, where N is the number of events with a magnitude greater than or equal to the magnitude M (in our case we use M_R). Plotting M_R against $\log_{10}(N)/N_{TOTAL}$ and evaluating the slope of the line gives the b-value for a set of observations.

$$\log_{10}(N) = a - bM \tag{4.5}$$

The b-value plot for all 2967 events (Figure 4.4) shows two clear sections, relating to the two peaks in the magnitude distribution (Figure 4.3). The section of the b-value curve corresponding to peak 1 has a value of b = 15 and peak 2 has a value of b = 2. This is an unusual distribution in the relationship between event magnitude and frequency of occurrence, for most systems a single line with a slope of b ∼1 represents the relative size distribution of seismicity. Unusual b-values are known to occur in a number of circumstances (*El-Isa and Eaton*, 2014), including situations where the stress regime changes significantly over the observation time. It is well established that tidal forcing transmitted upstream from the grounding line of Rutford Ice Stream causes variations in basal stress which result in surface velocity variations along the flow of around ±10% (see Section 3.4). This changing stress regime is a possible cause of the unusual seismic magnitude distribution.

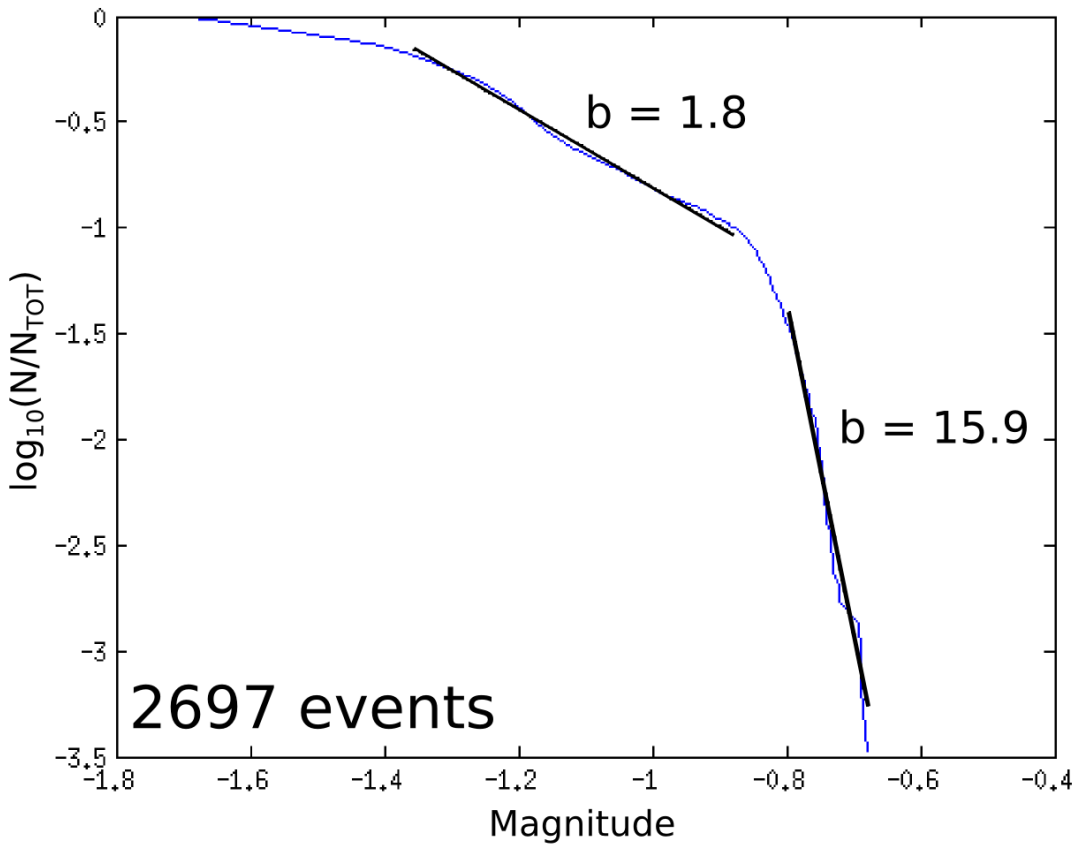

Figure 4.4: ***Seismic b-value plot for total basal seismicity under Rutford Ice Stream***

4.3.1 Re-assessment of Temporal Characteristics of Seismicity

In Section 3.4 it was observed that there was no clear correlation between the timing of the overall levels of basal seismicity and the 14.77 day periodic cycle in surface flow velocity of ±10% (*Gudmundsson*, 2006; *Murray et al.*, 2007), which is caused by changes in basal stress due to tidal forcing of Rutford Ice Stream. It has been shown that there are two distinct peaks in the seismic magnitudes and it would follow that the magnitude peaks may have a relationship to the changing stresses in this system. Plotting a histogram of just the events in peak 1 ($M_R > -0.9$) over time, indicates there are bursts of high magnitude seismicity around the time of lowest surface flow velocity (Figure 4.5). This suggests that while smaller magnitude events are not sensitive to changing basal stress, the high magnitude events occur predominantly at low ice stream velocity.

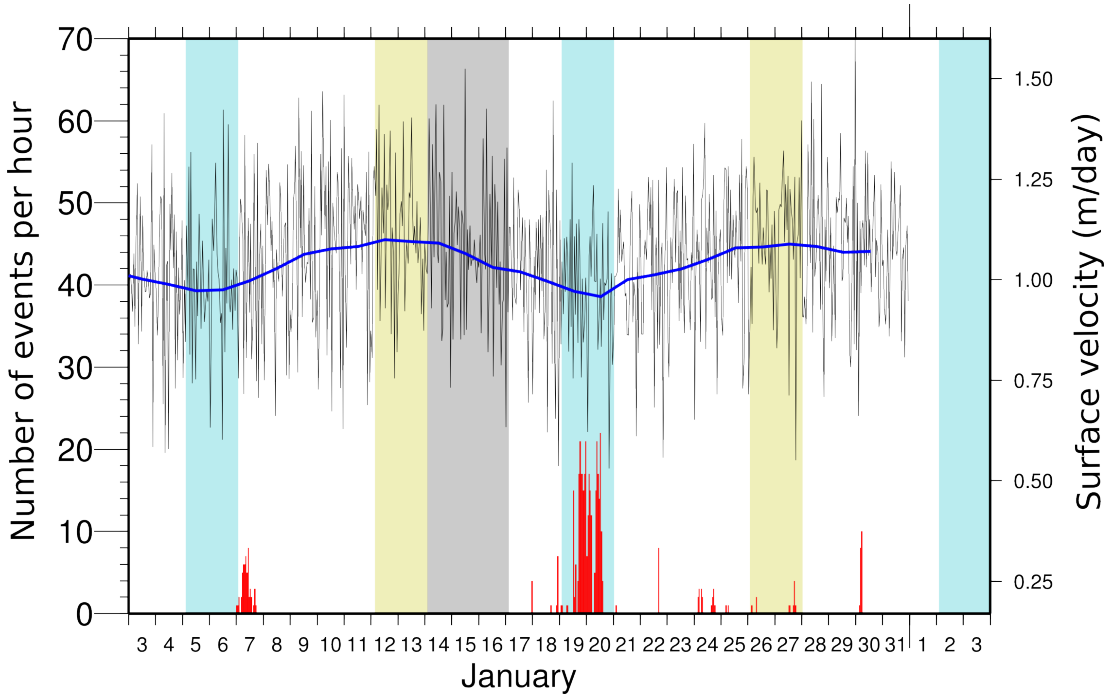

Figure 4.5: ***Histogram of the high magnitude events ($M_R > -0.9$) observed over the 32-day recording period.*** *Events (red) are binned in number of events per hour (left axis) and the surface velocity of the ice stream (right axis) determined from surface kinematic GPS data is also shown. The surface velocity is calculated once per hour (black). The blue line highlights the long wavelength cyclicity of 14.77 days, spring tides at the grounding line are highlighted in yellow and neap tides in blue (S. Rosier, personal communication). The level of seismicity of high magnitude events (peak 1, Figure 4.3) appears to increase at, or just after the lowest surface velocity values, which co-coincide with neap tides at the grounding line.*

This is again somewhat different to the findings of *Adalgeirsdóttir et al.* (2008) who observed highest levels of seismicity correlating with spring tides and high surface velocities. However, *Adalgeirsdóttir et al.* (2008) were looking at overall levels of seismicity. There are many more small magnitude seismic events compared to large events (in fitting with the Gutenberg-Richter law - see Section 4.3) and it remains possible that small magnitude events are more frequent during periods of higher ice stream flow velocity. However we do not see evidence of this in our data.

4.4 Fault Geometry

Estimating the dimensions of the source area which produces these seismic events at the base of Rutford Ice Stream can be achieved using Equation 4.6 (*Brune*, 1970, 1971; *Hanks and Thatcher*, 1972). This equation relates the radius of the fault (failure area, rather than a geological fault) to the corner frequency of the far-field S-wave displacement amplitude spectrum, assuming a circular fault geometry. The amplitude spectrum was determined from a clear S-wave arrival (Figure 4.6a), which was integrated to get the displacement waveform (Figure 4.6b) and then a fast Fourier transform was used to transform the signal from the time to the frequency domain. The resulting amplitude spectrum (Figure 4.6c, black line) shows a clear low frequency spectral level (Ω_0), which is proportional to the moment (M_0) and a corner frequency (f_c) of 50 Hz where the amplitude of the spectrum begins to fall off at higher frequencies. This spectrum is typical of S-wave spectra across the survey, suggesting that all the events are caused by faults of a similar size. Using this value of $f_c = 50$ Hz and a S-wave velocity $\beta = 1970\ ms^{-1}$, Equation 4.6 gives a fault radius of $r = 14.7$ m and a fault area, $A = 679\ m^2$.

$$r = \frac{2.34\beta}{2\pi f_c} \tag{4.6}$$

The stress drop ($\Delta\sigma$) on a fault of this geometry can also be calculated for the maximum seismic moment ($M_0 = 9.6\text{x}10^7$ Nm) and fault radius ($r = 14.7$ m) using Equation 4.7 (*Eshelby*, 1957). This gives a stress drop of $\Delta\sigma = 13.2$ kPa. The value of $\Delta\sigma$ is very sensitive to the chosen value of r as the term is cubed. The value of r is calculated from the corner frequency (f_c) of the S-wave displacement amplitude spectrum and therefore the effect of an error in determining f_c must be considered. A corner frequency (f_c) of 60 Hz (Figure 4.6c),

corresponds to a value of $r = 12.2$ m and $A = 469\ m^2$, this gives $\Delta\sigma = 23.0$ KPa. A corner frequency (f_c) of 40 Hz (Figure 4.6c), corresponds to a value $r = 18.3$ m and $A = 1052\ m^2$, this gives $\Delta\sigma = 6.9$ KPa. Therefore the value of stress drop should be seen as an order of magnitude approximation with $\Delta\sigma$ of the order of 10^1 kPa, r of the order of 10^1 m and A of the order of 10^2-$10^3\ m^2$. These values are all comparable with *Anandakrishnan and Alley* (1994) who calculated that basal seismic events with a moment of 10^7 Nm would have fault area of around $10^2\ m^2$ giving a stress drop of around 100 kPa.

$$\Delta\sigma = \frac{7M_0}{16r^3} \tag{4.7}$$

In this area of Rutford Ice Stream the average basal shear stress is around 35 kPa (*Vaughan et al.*, 2003), however, it is likely that the localised stress field at the base of Rutford Ice Stream is much higher than 35 kPa in places due to variations in bed topography and basal material, meaning that the stress is concentrated at particular points. The stress drop for a maximum magnitude event calculated above ($\Delta\sigma$ of the order of 10^1 kPa) is of the same order as the average basal shear stress, this suggests that in these fault areas the motion of the overlying ice stream could be accounted for purely seismically. However, the localised stress on 'sticky spots' is likely to be greater than the average, meaning that the amount of stress accounted for by a basal seismic events is probably much smaller.

Using Equation 4.2 the displacement (D) on the fault for a maximum moment ($M_0 = 9.6\text{x}10^7$ Nm) can be calculated, from the range of fault areas ($1052\ m^2 > A > 469\ m^2$) determined above and a rigidity between that of ice and till, $\mu = 2.73\text{x}10^9$ Nm^{-2} (*Anandakrishnan and Bentley*, 1993). This calculation gives a maximum displacement (0.03 mm $< D <$ 0.07 mm). This value, along with stress drop due to a basal seismic event of this type suggests that the amount of motion taken up by seismic deformation is small and that the ice stream motion over a 'sticky spot' is by both seismic and aseismic deformation.

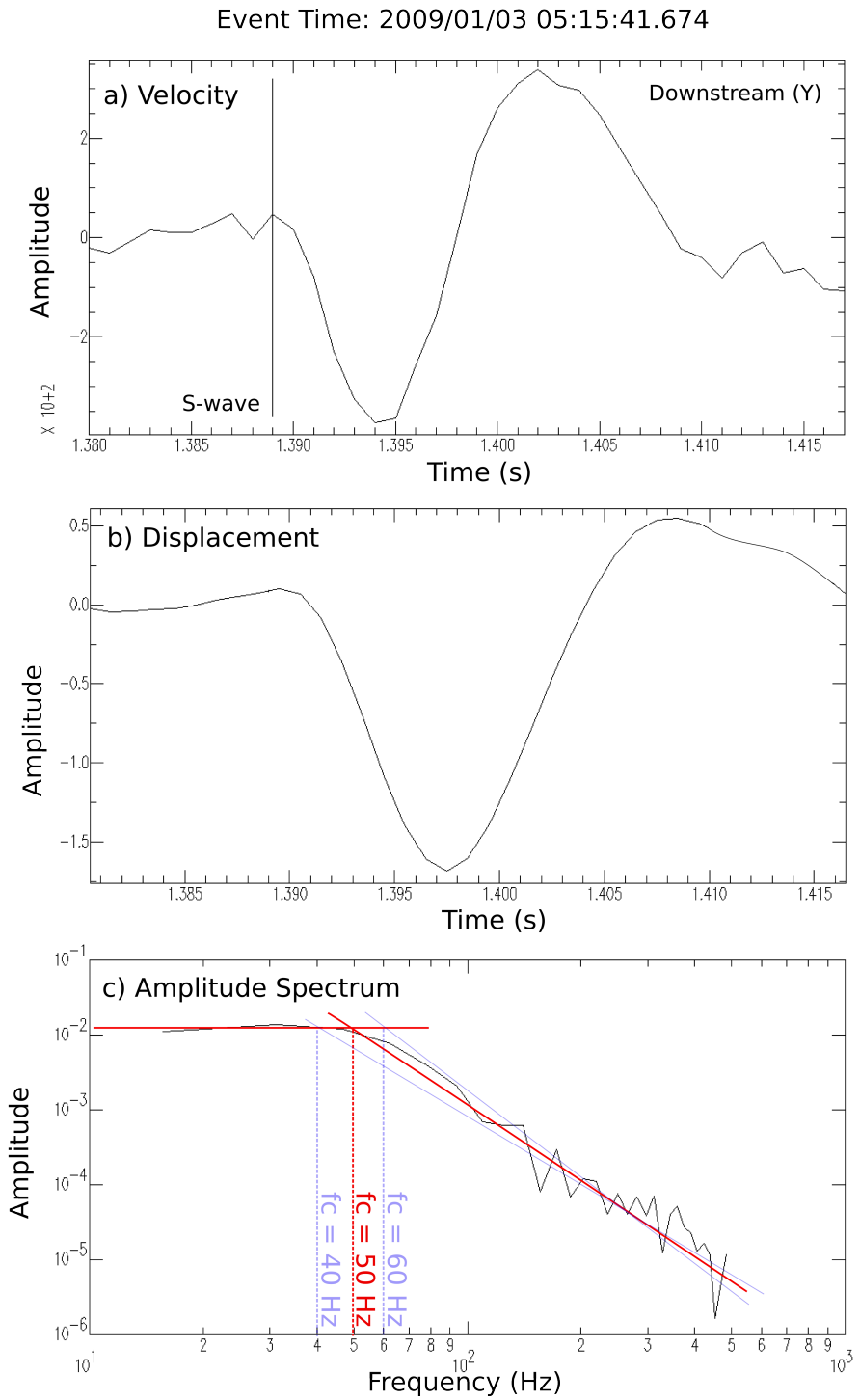

Figure 4.6: ***Determining the corner frequency for S-wave arrivals from the displacement amplitude spectrum.*** *a) A clear S-wave arrival on the downstream (Y) component of a single station. b) The displacement waveform (integral of a). c) The amplitude spectrum of the displacement waveform in b (black line). There is a clear corner frequency of 50 Hz.*

4.5 Discussion

I have suggested that event clusters identified in Chapter 3 are 'sticky spots' of stiff basal sediment at the ice-bed interface. Further inspection of the source of these events supports this 'sticky spot' hypothesis. Fault plane solutions constructed for a representative event in each cluster are consistent with low-angled faulting, slipping in the ice-flow direction, suggesting a basal sliding mechanism of ice over basal sediment is responsible for generating the events. Furthermore, when the location of 'sticky spots' are compared with a boundary between stiff and dilatant basal sediment areas, mapped from independent studies (G. Boulton personal communication) using seismic reflection and radar data (*Smith and Murray*, 2009; *King et al.*, 2009), it can be seen that the microseismic 'sticky spots' coincide with areas identified as stiff sediment (Figure 4.1). The dashed line in Figure 4.1 indicates the boundary between stiff and dilatant sediment, with the stiff-sediment areas lying to the south of this boundary. The majority of 'sticky spots' fall inside the stiff-sediment areas and many are located at, or close to, the boundary between the contrasting sediment types. This pattern suggests the change in basal conditions and sliding characteristics at this boundary may play a role in initiating the seismicity.

The magnitude of events varies through the 32-day recording period with a range of -1.77 $< M_R <$ -0.67 showing two distinct peaks in the distribution, above and below M_R = -0.9. I have hypothesised this is due to changing basal stresses as a result to tidal forcing at the grounding line. A re-assessment of the timing of seismicity shows that the high magnitude events appear to occur in bursts around times of low surface velocities. Although the length of the data record is not sufficient to confirm this pattern, it hints at a correlation between surface velocity and basal seismicity rates. *Rosier et al.* (2015) showed that changing subglacial water pressure and thus changing effective pressure at the base of Rutford Ice Stream could explain the surface velocity variations observed in this area. This mechanism can be used to explain the occurrence of high magnitude events at low surface velocities. If water pressure in the sediments underlying Rutford Ice Stream is changing, a stiffening of the sediment may be expected at lower surface velocities. If the sediment at the 'sticky spots' stiffened, it could then support a greater shear stress, reflected in the fact that the events in the high magnitude peak coincide with these times. *Anandakrishnan and Bentley* (1993) found larger events occurred under the slower moving Kamb Ice Stream than the faster moving Whillans Ice Stream, which could be due to a similar mechanism. However, a

longer record of basal seismicity over time would be needed to confirm this idea. The lack of correlation between surface velocity and overall basal seismicity levels (see Section 3.4) in Rutford Ice Stream indicates that the changes in basal stress that affect the surface velocity do not have a strong control on the amount of stress released seismically on the 'sticky spots' in this area.

The 'sticky spots' are shown to be small, of the order of 10^1 m in radius, with a single slip event giving a maximum displacement of the order of 0.1 mm and a stress drop of the order 10^1 kPa. The average basal shear stress in this area of Rutford Ice Stream is 35 kPa, although due to significant local basal topography it is likely to be much larger than this in some areas. This implies that only a small amount of the basal shear stress is taken up by seismic failure and supports the hypothesis proposed in Chapter 3 that much of the motion of Rutford Ice Stream is taken up aseismically. This is unlike other Antarctic ice streams where stick-slip on large scale 'sticky spots' is the dominant motion (*Wiens et al.*, 2008; *Winberry et al.*, 2013). It could also suggest that it is the material which is deforming aseismically, that is subject to alterations in stress due to tidal forcing.

4.6 Conclusions

In this chapter I have made an assessment of the source characteristics of the basal microseismic events in this area of Rutford Ice Stream to support the hypothesis that events occur by stick-slip basal sliding on 'sticky spots' of stiff basal sediment at the ice-bed interface. I have shown that 'sticky spots' coincide with areas independently identified as stiff basal sediment and that many of them occur close to an interpreted boundary between stiff and dilatant sediment. The 'sticky spots' are small, in the region of 10-20 m, and the displacement on them is taking up only a small amount of the overall motion of the ice stream, suggesting that the majority of movement in this area is accommodated by aseismic bed deformation.

These results highlight the value of passive seismic techniques, especially if combined with more traditional active seismic and radar methods, in providing an interpretation of the material characteristics of an ice stream bed. Microseismic monitoring proves to be an effective tool for investigating both the spatial and temporal basal dynamics that accommodate ice stream motion; using this technique I have added new and complementary information to a well-studied area of Rutford Ice Stream.

Chapter 5

Shear Wave Splitting Analysis

5.1 Introduction

A total of 5951 good shear wave splitting measurements were made over the 32-day recording period, following the automated analysis process outlined in Section 2.5. The spatial pattern and timing of SWS measurements is investigated and the sensitivity of these measurements to waveform frequency is investigated. I go on to perform an inversion for the best fitting ice fabric model for the observed measurements and discuss how this fabric relates to the stress regime of an ice stream. I show how measuring shear wave splitting in microseismic data is a highly effective means of determining the spatial distribution of ice fabric in a fast flowing ice stream.

5.2 Overview of Splitting Measurements

Measurements of the shear wave splitting parameters (polarisation orientation of the fast shear wave, Φ, and the delay time, δt) were made on all 29670 shear wave arrivals for events detected and located in this data set, using the automated method described in Section 2.5. Many of these measurements were not good, due to poor SNR of the waveforms or 'null' measurements (see Section 2.5.1.2). After quality control I obtained 5951 good splitting measurements at a wide range of azimuths and inclinations.

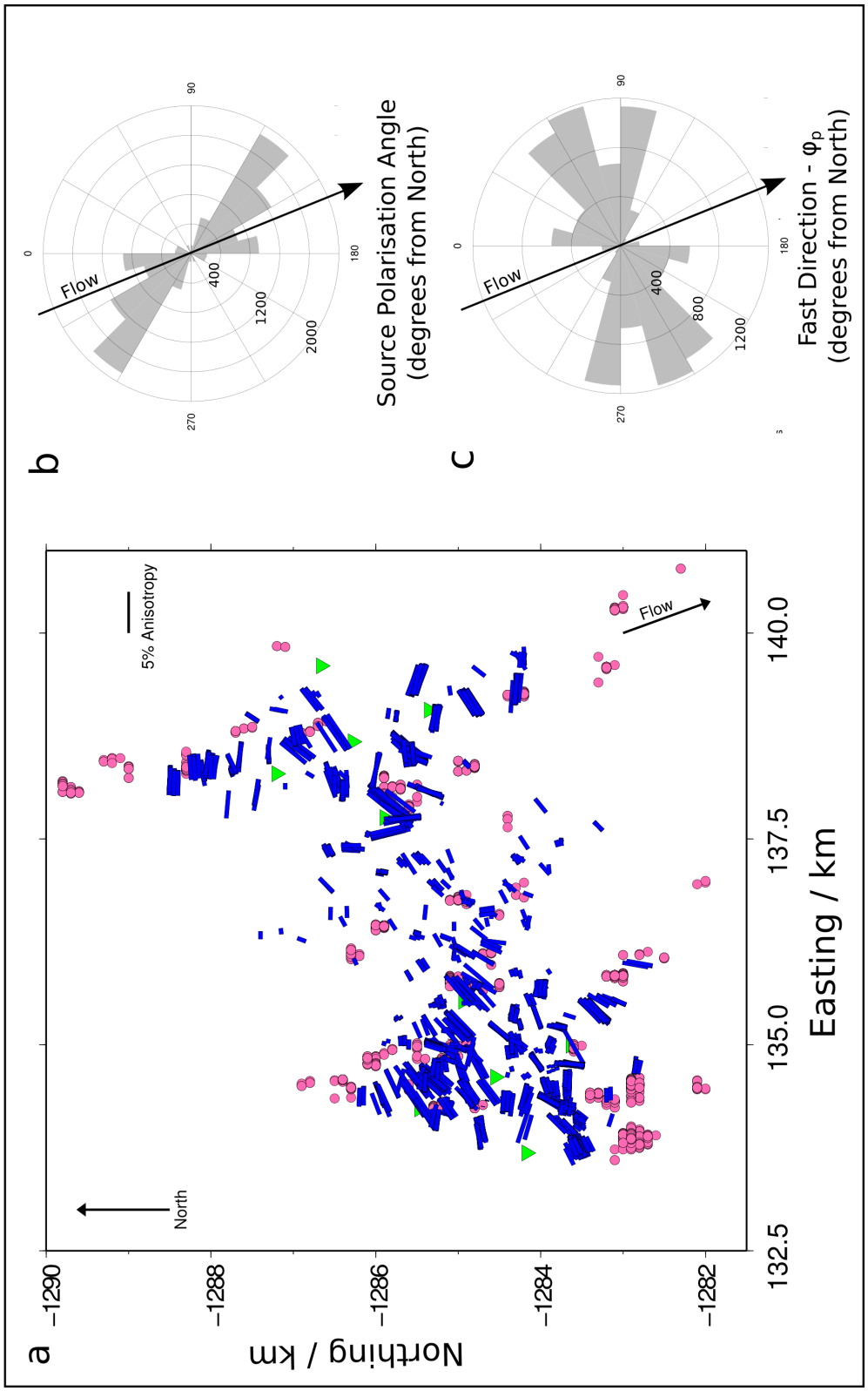

Figure 5.1: ***Overview of 5951 good shear wave splitting measurements.*** *a) Events are shown in pink, splitting measurements are blue bars, plotted half way between the event and the station. The orientation of the bar is the fast shear wave direction and the length represents % Anisotropy b) A rose diagram of the source polarisation of all splitting measurements in degrees from North (0°), the number of measurements at each azimuth is represented by the length of the bar. c) A rose diagram of the fast shear wave direction of all splitting measurements (ϕ_p) in degrees from North (0°), the number of measurements at each azimuth is represented by the length of the bar.*

Figure 5.1a gives a summary of the good SWS measurements. Each measurement (blue bar) is plotted half way between the event location and the station at which it was recorded. The orientation of the bar indicates the fast shear wave polarisation from north (ϕ_p) and the length of the bar indicates the strength of anisotropy in percent ($\%A$). Rose diagrams summarise the orientation of the source polarisation direction (Figure 5.1b) and the fast shear wave (Figure 5.1c) for all 5951 measurements. The source polarisation will be discussed in more detail in Section 5.2.1.

The general trend of measurements across the survey area is consistent, with the dominant polarisation of the fast shear wave (ϕ_p) perpendicular to the ice flow direction and maximum shear wave splitting occurring in the near vertical ray paths (Figure 5.1a). There is no systematic variation in ϕ_p for different regions of the ice stream suggesting the ice fabric in this area is uniform and all measurements can be treated as sampling the same fabric at a variety of ray azimuths and angles of inclination. The region between the two clusters appears to show reduced anisotropy. However, this area is largely being illuminated by ray-paths with a high angle of inclination (i.e. nearing horizontal) which experience less splitting than the near-vertical ray-paths (Figure 5.2).

The relationship between the strength of splitting and angle of inclination can be better seen on an upper hemisphere plot of the data (Figure 5.3), where measurements are plotted at their azimuth from north (event to station azimuth) and ray-path inclination. Near vertical ray paths plot in the centre and near horizontal ray paths at the edge. The direction of the bar representing each measurement represents ϕ_p and the length and colour represents $\%A$. The highest value of $\%A$ observed in this data set is $\sim$5%, represented by the blue coloured measurements. The pattern of SWS shows a general trend of greatest SWS in the vertical, weakening with increasing angle. However, the strength of splitting is not consistent for a given inclination, showing some azimuthal variation. For example, ray paths at 30°-40° inclination at 45° azimuth (Figure 5.3) show around 1.5% splitting (red), whereas measurements at the same inclination at 180° azimuth show around 2.5-3% splitting (green), almost double.

This pattern does not appear to fit any single one of the fabric models shown in Figure 2.15, indicating there is some complexity in the ice fabric in the region and suggesting a combination of the fabric models maybe be needed to explain the pattern of observed SWS.

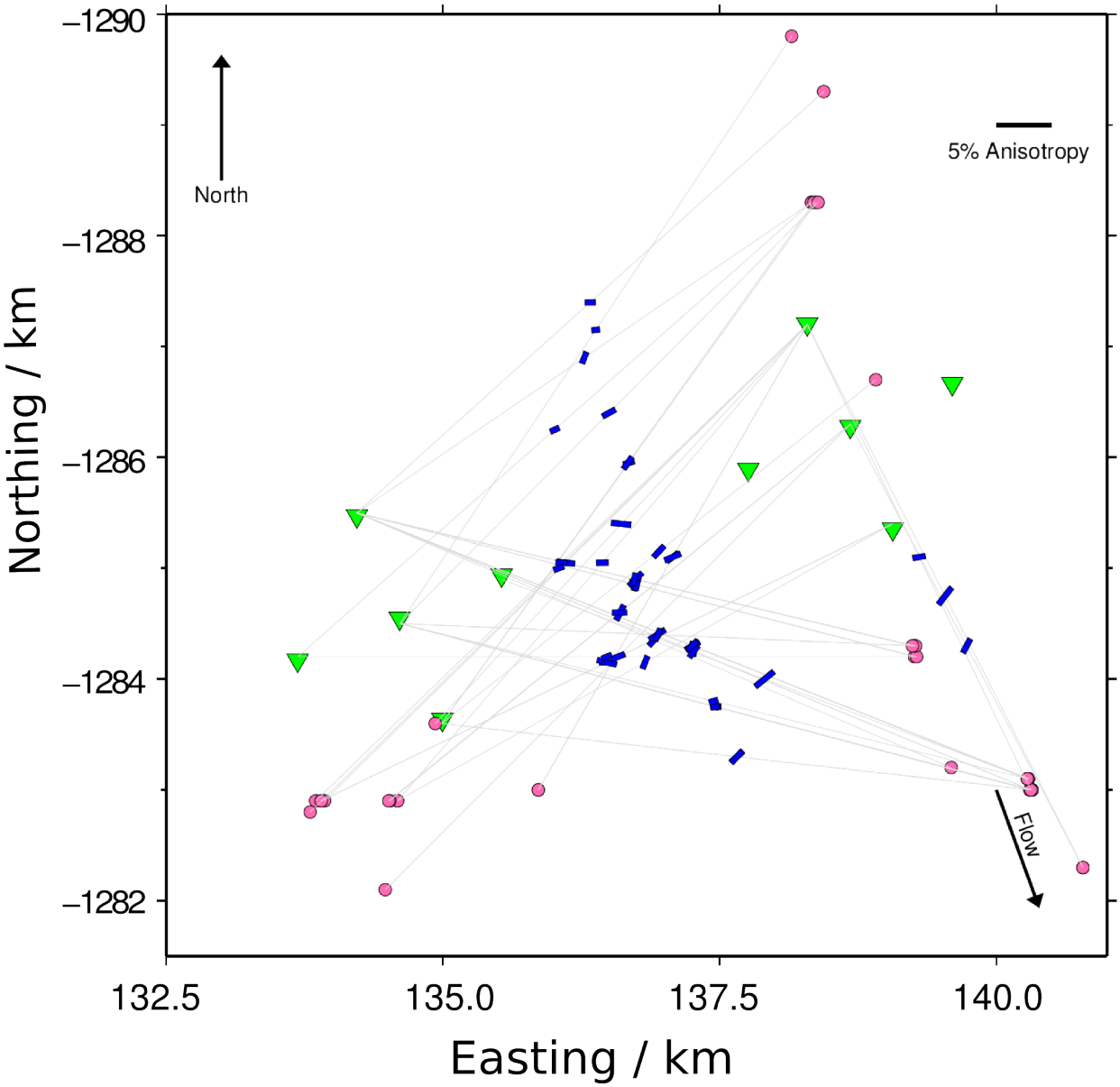

Figure 5.2: ***Shear wave splitting measurements at inclination angles > 65°.*** *Events are shown in pink, splitting measurements are blue bars, plotted half way along the ray path (grey line) between the event and the station. The area between the two arrays is illuminated by high inclination ray paths which experience less spitting than near-vertical ray paths, meaning it appears to have reduced anisotropy.*

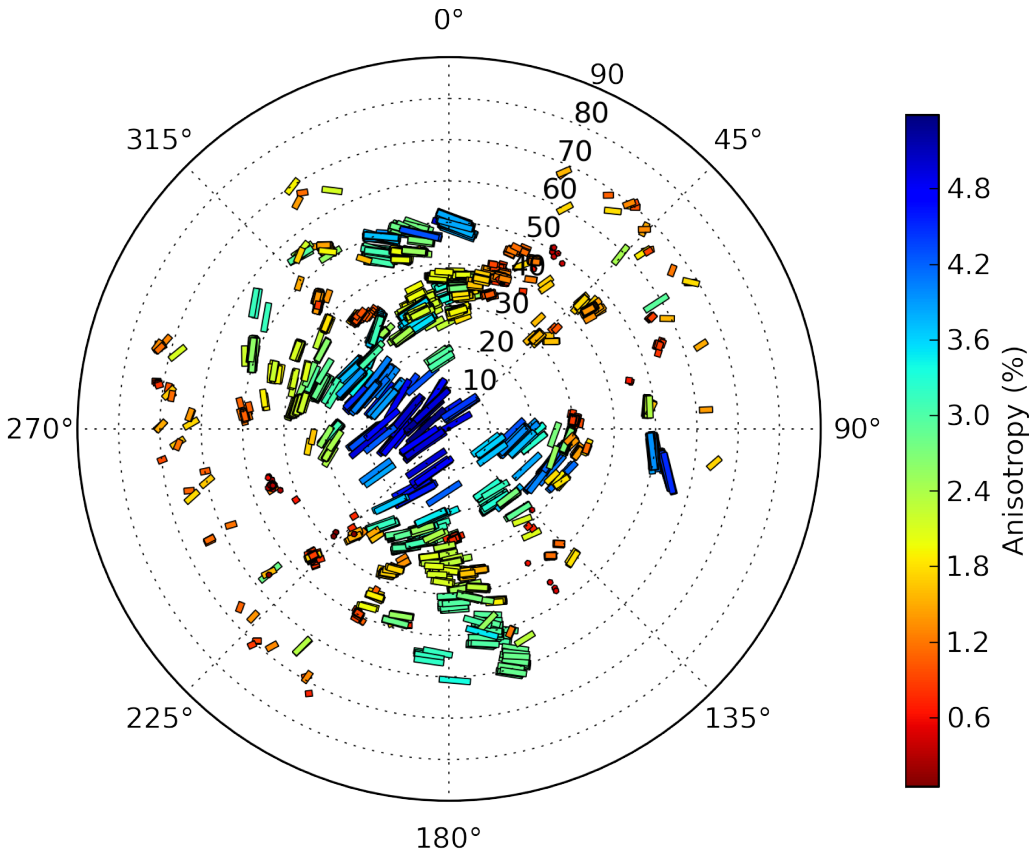

Figure 5.3: ***Upper hemisphere plot of 5951 good splitting measurements.*** *Measurements are plotted at their azimuth from north (event to station) and ray-path inclination. The direction of the bar representing each measurement represents ϕ_p and the length and colour represents $\%A$. The maximum inclination at which good quality measurements were observed was 73°, hence there are no measurements towards the outside of the plot.*

5.2.1 Source Polarisation

Estimates of source polarisation (Figure 5.1b) for all the shear waves show that they are predominantly between 20-40 degrees anti-clockwise from the ice flow direction. In Section 4.2, I constructed fault plane solutions for a representative event from each location cluster. The orientation of the slip vectors for the fault planes should be comparable to the source polarisation measurements determined from SWS measurements for the same events. Figure 5.4 shows a comparison between the slip vector orientation and the corresponding source

polarisation direction for the same subset of events. The two measurements are largely consistent with the majority of the slip vectors showing an orientation of 0-10 degrees anti-clockwise from the ice flow direction and the majority of source polarisation measurements showing an orientation of 10-20 degrees anti-clockwise from the ice flow direction. The fault plane solutions and thus the slip vectors derived from them are determined from the P-wave polarities, whereas, the source polarisations measurements are derived from S-wave particle motion. This means they provide two independent measurements of the direction of slip at the source of these events and show it is consistently anti-clockwise from the ice flow direction.

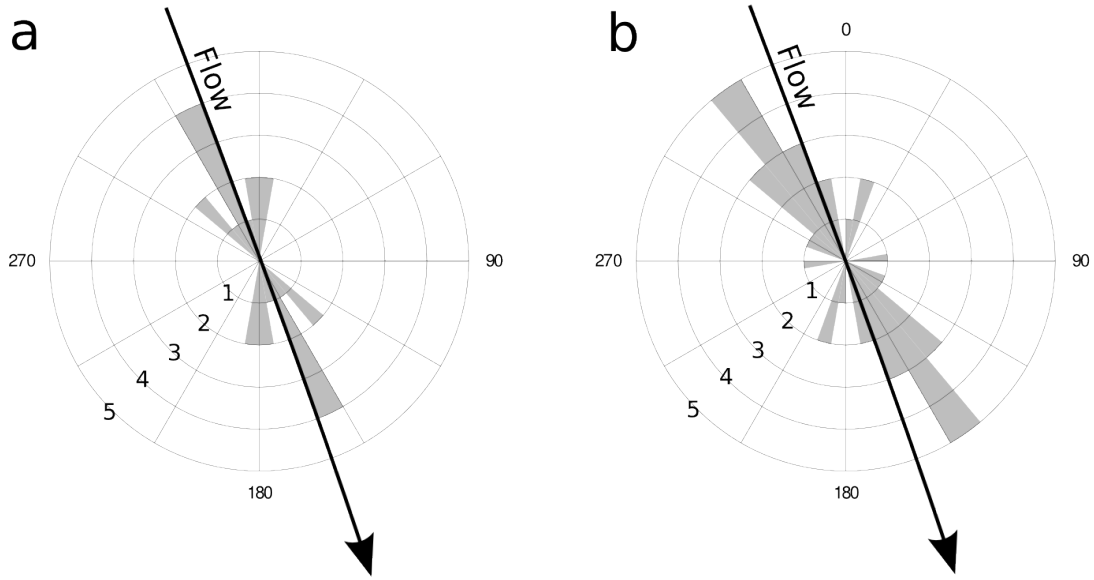

Figure 5.4: ***Comparison of source polarisation measurements from SWS analysis with slip vectors determined from fault plane solutions.*** *a) Rose diagram of the orientation of slip vectors of the fault plane solutions for representative events in each location cluster (Figure 4.1). b) Rose diagram of the source polarisation direction, for the same subset of events, determined from SWS analysis.*

5.2.2 Frequency of S-wave Used for Analysis

The sensitivity of SWS measurements to the frequency of the input waveform provides information about how sensitive the measurement may be to different length scale features in the ice fabric. If a splitting measurement is not stable over a variety of input waveform frequencies, it would suggest that shear waves are being affected by certain length scale features, such as layering of different ice fabrics. This would mean that the measurements become frequency dependent. This can be tested by comparing splitting measurements made on the same input waveforms, bandpass filtered at a range of frequencies.

The shear wave splitting results (Figure 5.1) were made on unfiltered waveforms with a frequency range of 1-500 Hz, with 500 Hz being the Nyquist frequency. An example of such a measurement is given in Figure 5.5.

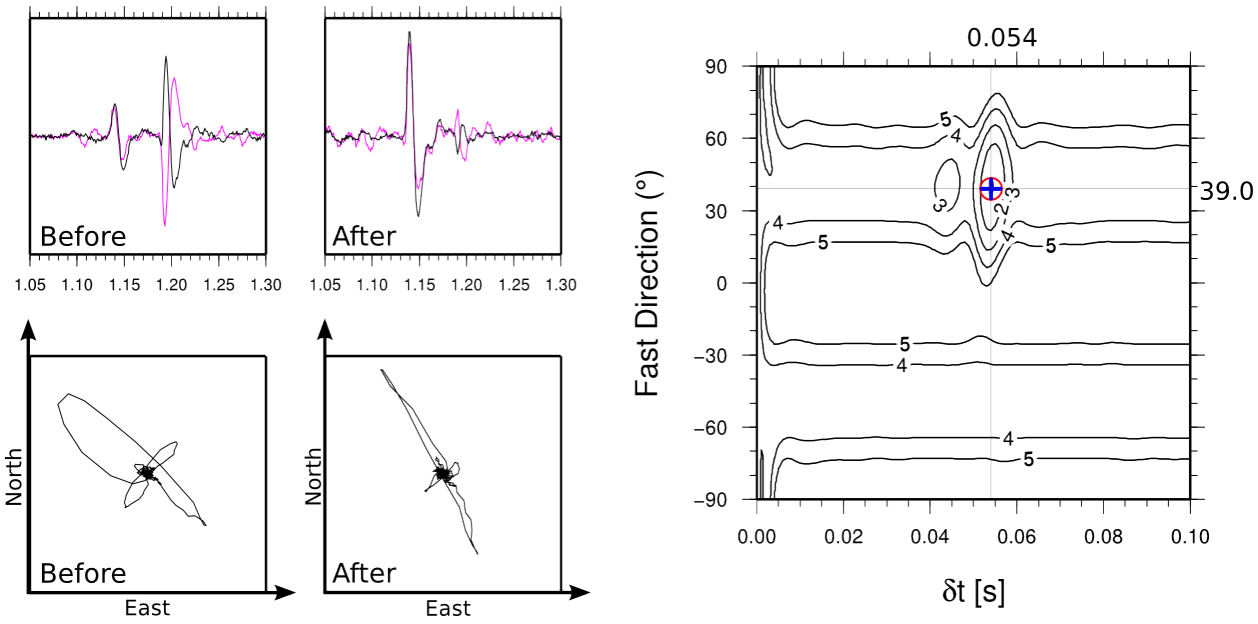

Figure 5.5: ***Full frequency shear wave splitting measurement (1-500 Hz).*** *A clear split shear wave before correction and the well matched waveforms after correction (top left). The shear wave particle motion before correction showing two clear orthogonal directions and after correction showing linearised particle motion (bottom left). The error surface for the full range of Φ and δt values using the EV method, with the minimum marked by the blue cross. The red circle shows the minimum for the XC method, which is in agreement with the minimum determined by the EV method, the value of each splitting parameter at this minimum is shown (Φ = 39.0° and δt = 0.054).*

The error surface of trial values of Φ and δt (right hand side, Figure 5.5) shows a clear minimum for both the XC method (red circle) and the EV method (blue cross), which are in good agreement. The orientation of the fast shear wave (Φ) is 39.0 $\pm$1.5° and the delay time (δt) is 0.054 $\pm$ 0.000 s. Errors are determined using an F test to calculate the 95% confidence interval (*Silver and Chan*, 1991).

The corner frequency of a typical shear wave is $\sim$50 Hz (see Section 2.2), therefore two frequency bands below this value were chosen to test the sensitivity of the splitting measurement to the frequency of the input waveform. Performing the SWS measurement on the same input data but with bandpass filtered waveforms at 0-10 Hz (Figure 5.6a) and 20-40 Hz (Figure 5.6b) shows good correction of the splitting and linearisation of the particle motion in both cases. Despite the fact that the 0-10 Hz waveforms are not clear, the splitting parameters are close to those determined from the unfiltered waveforms. The measured fast shear wave polarisation (Φ = 51.0 $\pm$8.7°) and delay time (δt = 0.056 $\pm$ 0.003 s) differ from the full frequency result by only 12.0° and 0.002 s respectively. These differences are within the 95% confidence interval for δt and just outside the 95% confidence interval for Φ. The parameters determined from the 20-40 Hz waveforms are, unsurprisingly, closer to those determined from the unfiltered data with Φ = 38.0 $\pm$ 2.8° and δt = 0.055 $\pm$ 0.000 s.

The SWS measurement appears to be stable over a range of frequencies and thus wavelengths. The inversion method used to determine ice fabric from SWS measurements (Section 2.5.2) can be used to mix different ice fabrics together but does not account for layered ice fabrics. As the SWS measurements are stable of over a range of frequencies this suggests that using a mixed, rather than a layered, ice fabric model is a reasonable solution for this region.

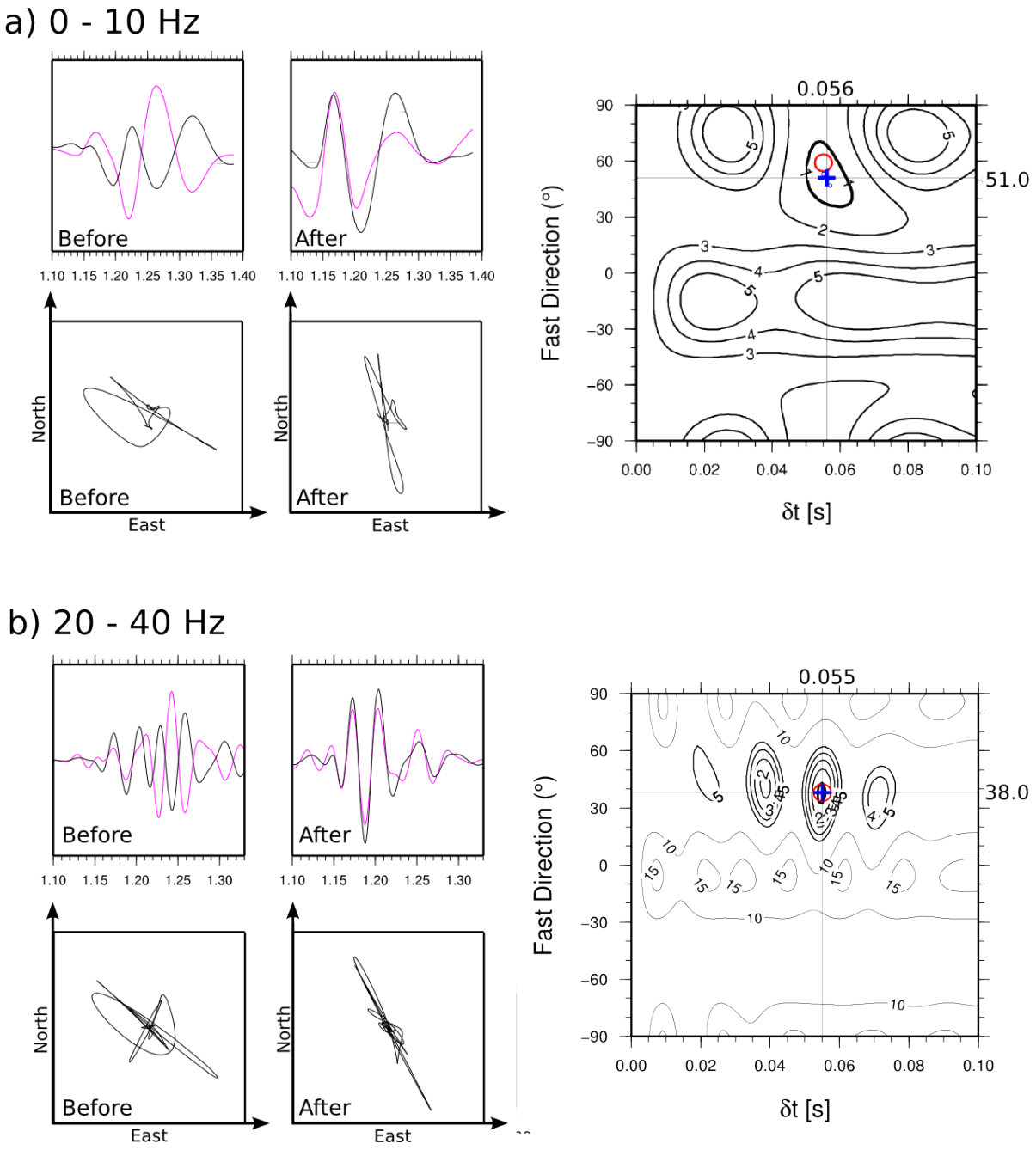

Figure 5.6: ***Shear wave splitting measurements on frequency filtered waveforms*** *a) Waveforms filtered between 0-10 Hz before analysis. Although the waveforms are not clear they appear to be matched after correction (top left) and the particle motion is linearised (bottom left). The error surface shows a clear minimum, with a slight difference between the values determined by the EV (blue cross) and XC methods (red circle). The thick black line indicates the 95% confidence contour b) Waveforms filtered between 20-40 Hz before analysis. The waveforms are well matched after correction (top left) and the particle motion linearised (bottom left). The error surface shows a clear minimum, with the values determined by the EV (blue cross) and XC (red circle) methods being in agreement.*

5.2.3 Timing

The 5951 SWS measurements presented here were made on events that occurred during the full 32-day recording period. In order to use all the measurements to invert for a bulk ice fabric it is important to establish that there are no significant changes in anisotropy over time. Figure 5.7 shows the value of $\%A$ (pink circles) over time. It is clear that a range of values of $\%A$ occur throughout the recording period and that there is no systematic variation or pattern in the values of $\%A$ over time, which means treating all measurements as sampling the same ice fabric over the recording period is a valid assumption.

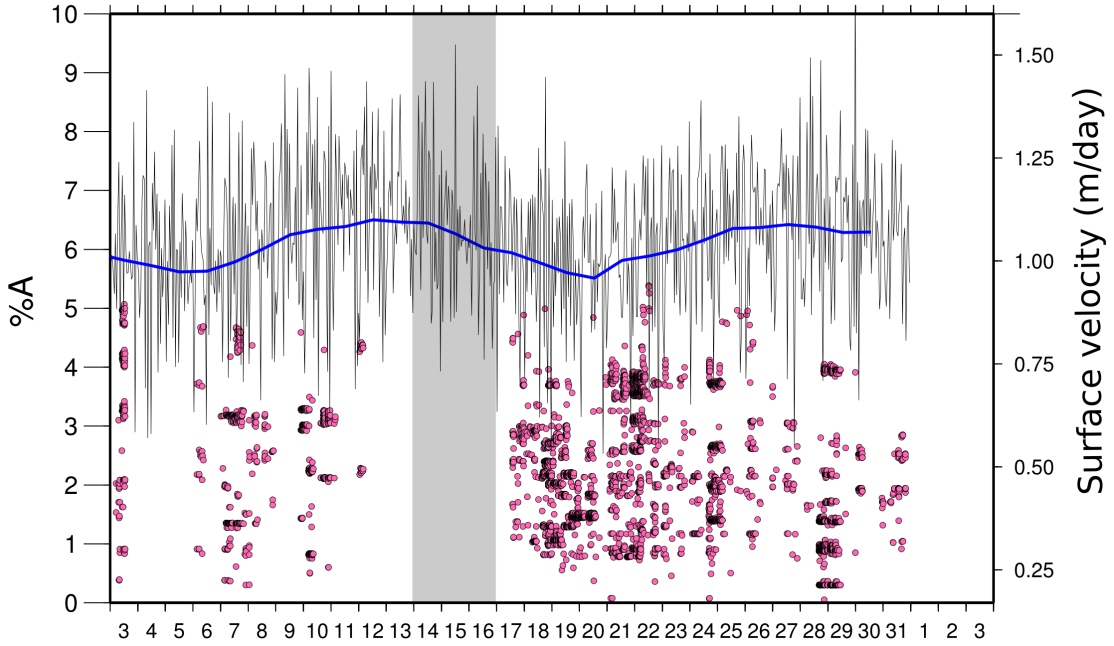

Figure 5.7: ***The change in*** $\%A$ ***over time for 5951 shear wave splitting measurements.*** *The value of* $\%A$ *is shown by the pink circles (left axis) and the surface flow velocity of the ice stream (right axis) determined from surface kinematic GPS data is also shown (see Section 3.4). The grey bar indicates a period of data drop out where no events were detected. A range of* $\%A$ *occur through time with no clear temporal pattern. In particular, no correlation of* $\%A$ *with the changing surface velocity is seen.*

It is well documented that the surface velocity of Rutford Ice Stream changes periodically due to perturbations in basal shear stress caused by tidal forcing, transmitted up stream of the grounding line. If a periodic change in $\%A$ were observed it could suggest that the

changing stresses in the ice stream were causing cracks in the ice to open and close, as a CPO fabric would not change significantly on these time scales. This is not apparent in these data (Figure 5.7) and so using a purely intrinsic CPO ice fabric model (as opposed to a model that includes other forms of anisotropy, such as cracks in the ice) is reasonable for this area.

5.3 Inversion for Anisotropy Model

The observed pattern of shear wave splitting measurements can be inverted for the type of ice CPO fabric that would affect the propagation of shear waves in this way, following the process outlined in Section 2.5.2. Initial observations in the pattern of SWS measurements (Section 5.2) are used to inform the choice of ice fabric combinations to invert for. The observed pattern of SWS shows a clear maximum in $\%A$ for vertically propagating shear waves and a clear variation in strength of splitting with azimuth (Figure 5.3). This immediately rules out a pure cluster ice fabric as this has VTI symmetry and exhibits a minimum in SWS for vertically propagating S-waves. The splitting would also be azimuthally invariant for a given angle from the vertical (Figure 2.15a). The expected pattern of splitting for each of the girdle fabrics (Figure 2.15b,c,d) shows strong $\%A$ in vertically propagating shear waves, with the orientation of the fast shear wave perpendicular to ice flow, as in the observed data. The thick girdle fabric is a pure HTI fabric and predicts a band of high splitting across all inclinations of shear waves propagating perpendicular to the ice flow direction. This is not apparent in the observed data, where splitting decreases at high inclinations. Therefore, the fabric is not pure HTI either. The patterns of SWS predicted by each of the partial girdle fabrics (which have orthorhombic symmetry) appear to fit many of the features of the observed data but they both predict a much higher percentage of splitting than the observed data. Therefore, a combination of the ice fabric models is inverted for. I have chosen three starting conditions - a combination of a cluster fabric with each of the different girdles.

The observed measurements were smoothed before inversion by taking the average of the measurements in inclination and azimuth bins of $5^\circ \times 5^\circ$, to prevent the inversion being biased by the uneven distribution of observations (Section 2.5.2). Figure 5.8 shows the observations before and after smoothing. It is these smoothed data that are used in the inversion process and so each of the results presented are compared to the smoothed data. As described in Section 2.5.2 the inversion process mixes the two input fabrics together for the full range of proportions of each and for all possible opening angle combinations for each

fabric. Therefore, it is possible to end up with a result that is purely one of the input fabrics, or a mixture of the two. The best fitting result of each of the three inversions is presented here. Each result is shown with the individual ice fabric components (a and b) and the mixed fabric (c), the smoothed measurements are shown for comparison (d).

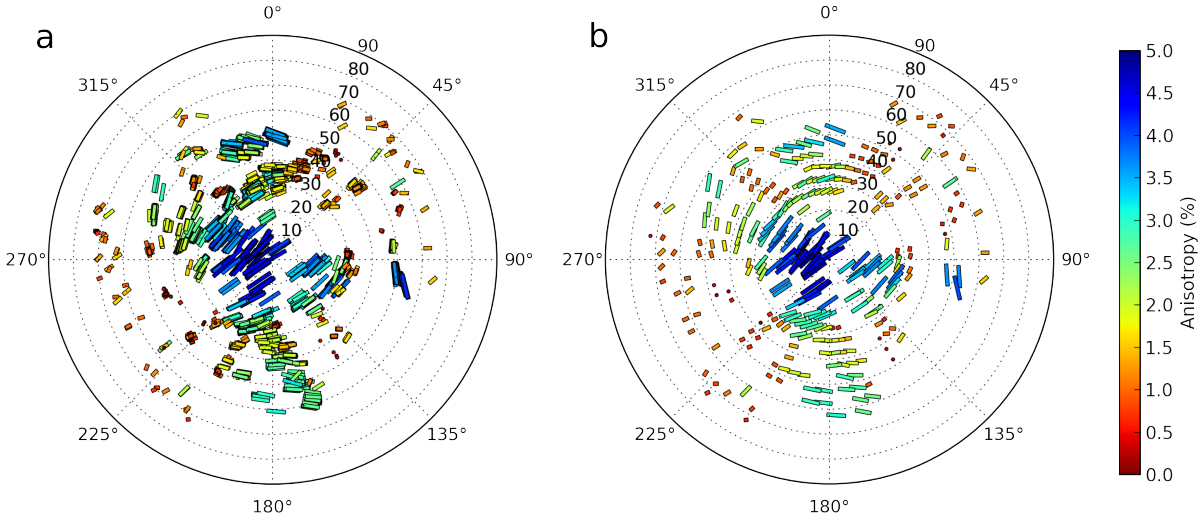

Figure 5.8: ***Upper hemisphere plots of all 5951 shear wave splitting measurements before and after smoothing.*** *a) Shear wave splitting measurements before smoothing, as in Figure 5.3. Shear wave splitting measurements which have been smoothed by taking the average of the measurements in inclination and azimuth bins of 5°× 5°.*

Thick Girdle + Cluster

The first model is a combination of a thick girdle and a cluster fabric (Figure 5.9). The best fitting model is 67% cluster with an opening angle of $\theta = 69°$, and 33% thick girdle with an opening angle $\xi = 0°$, orientated near orthogonal to the ice flow direction, with a girdle angle (pole to the girdle orientation) of 143° relative to true North. This means the best fitting thick girdle contains the c-axes in a single vertical plane perpendicular to the ice flow direction. This is equivalent to a partial girdle which extends to an opening angle $\theta = 90°$, suggesting that a partial girdle model may provide a good fit to these data also. A cluster fabric with an opening angle of $\theta = 69°$ has a very low degree of anisotropy and when mixed with a thick girdle it essentially reduces the overall strength of anisotropy in the resulting combined ice fabric.

When compared to the observed measurements the best fitting model (Figure 5.9c) shows a reasonable fit to the general trend of observed measurements (Figure 5.9d) with greater splitting in the vertically travelling rays (centre of the plot) and an azimuthally varying pattern of splitting away from the vertical. However, the strength of anisotropy is overall much weaker than the observed measurements, with the $\%A$ of vertically travelling rays being around 2.3%, half of the observed value. The misfit, calculated from Equation 2.2, which is the sum of the magnitude of the vector difference between the modelled splitting parameters and the measured splitting parameters is 448 for the combined thick girdle and cluster model. This number alone does not tell us a great deal, however, it provides a quantitative comparison for the fit of the observed measurements to each of the inversions.

Vertical Partial Girdle + Cluster

The second model is a combination of a vertical partial girdle and a cluster fabric (Figure 5.10). The best fitting model is 56% cluster with an opening angle of $\theta = 70°$, and 44% vertical partial girdle with an opening angle $\theta = 48°$, orientated near orthogonal to the ice flow direction at 144° relative to true North. This combined fabric (Figure 5.10c) has a greater range of strength of anisotropy than the thick girdle and cluster combination (Figure 5.9), which is a better match to the observed data. This is reflected in misfit value of 431, compared to 448 for the thick girdle and cluster model. The general pattern in $\%A$ and orientation of the fast shear wave matches well (Figure 5.10c), although the $\%A$ is still weaker than the observed measurements. For example, at an azimuth of 180° both the modelled and observed data at an inclination of 50° show stronger $\%A$ than those at 40°, showing the model fits the trend of $\%A$ in the measured data. However, the value of the modelled $\%A$ at 50° is 2.1%, whereas the measured value is around 3.1%.

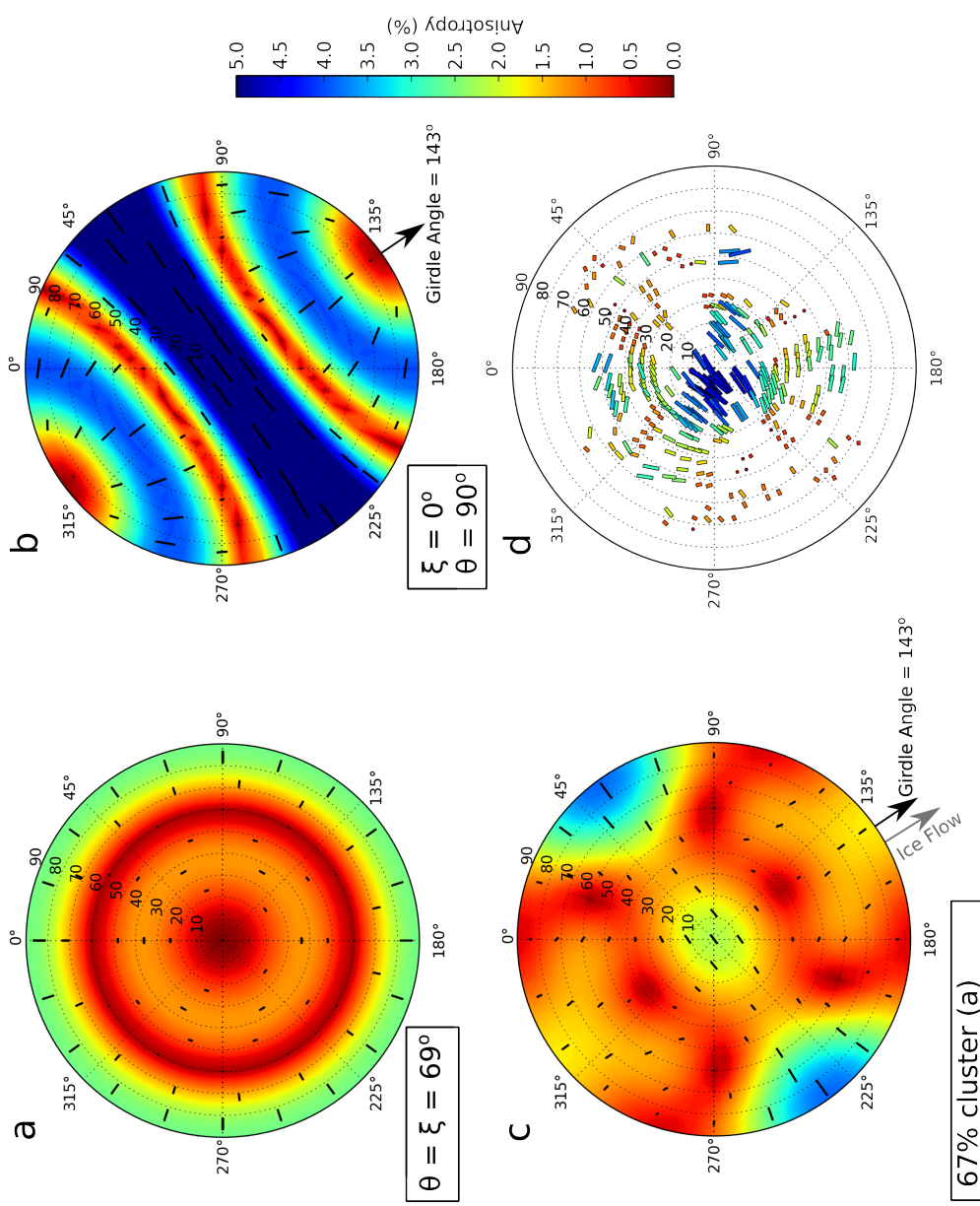

Figure 5.9: ***Result of inversion for a combination of thick girdle and cluster fabric on an upper hemisphere plot.*** *a) The cluster component of the best fit fabric mixture, it is a broad cluster with an opening angle of $\theta = 69°$. b) The thick girdle component of the best fit fabric mixture, it is a single plane ($\xi = 0°$) orientated across the ice flow direction, with a girdle angle (pole to the girdle orientation) of 143°. c) The best fit mixed model, 67% cluster and 33% thick girdle. d) The smoothed SWS measurements for comparison.*

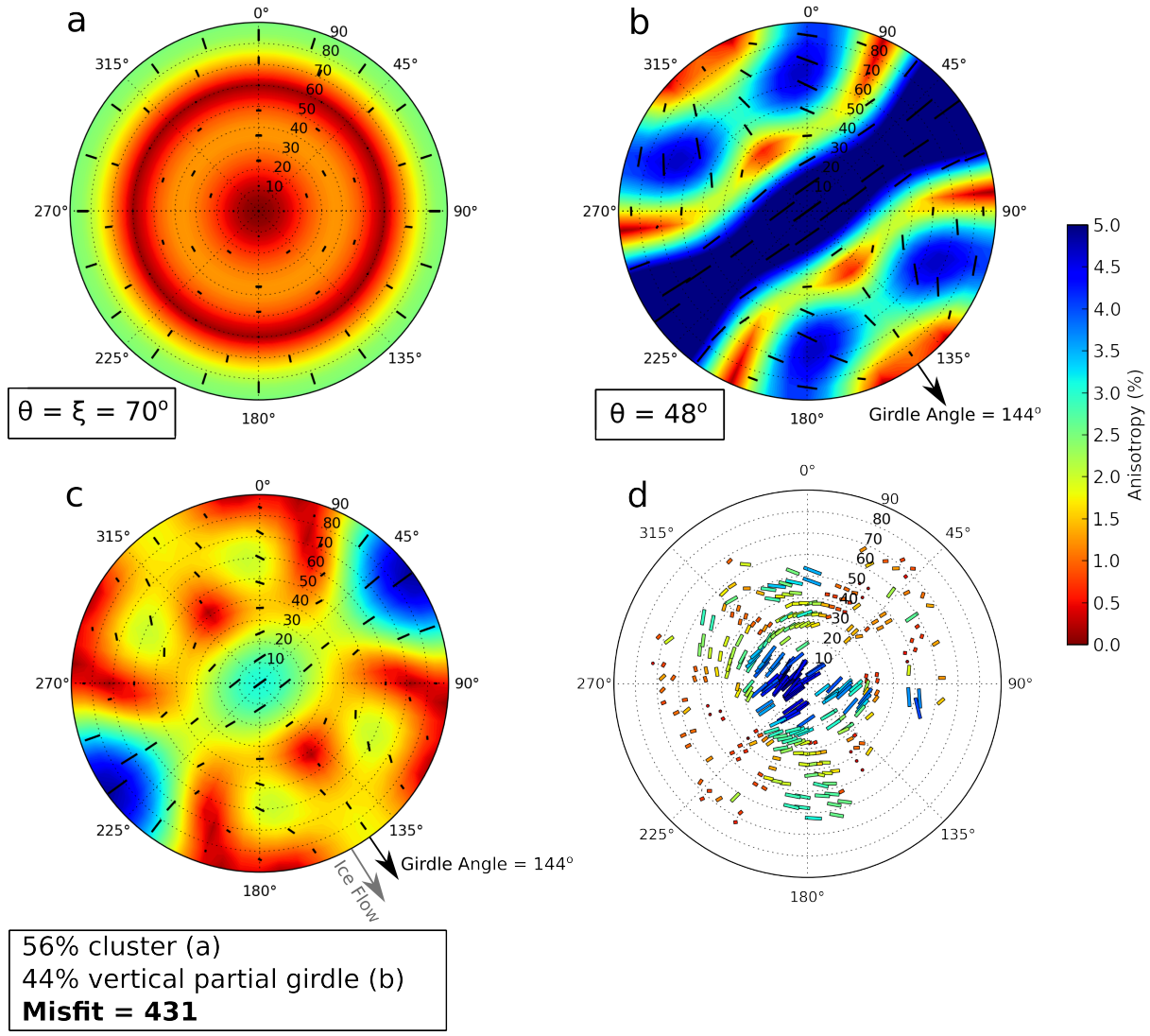

Figure 5.10: ***Result of inversion for a combination of vertical partial girdle and cluster fabric on an upper hemisphere plot.*** *a) The cluster component of the best fit fabric mixture, it is a broad cluster with an opening angle of $\theta = 70°$. b) The vertical partial girdle component of the best fit fabric mixture, with an opening angle of $\theta = 48°$, orientated near orthogonal to the ice flow direction, with a girdle angle (pole to the girdle orientation) of 144°. c) The best fit mixed model, 56% cluster and 44% vertical partial girdle. d) The smoothed SWS measurements for comparison.*

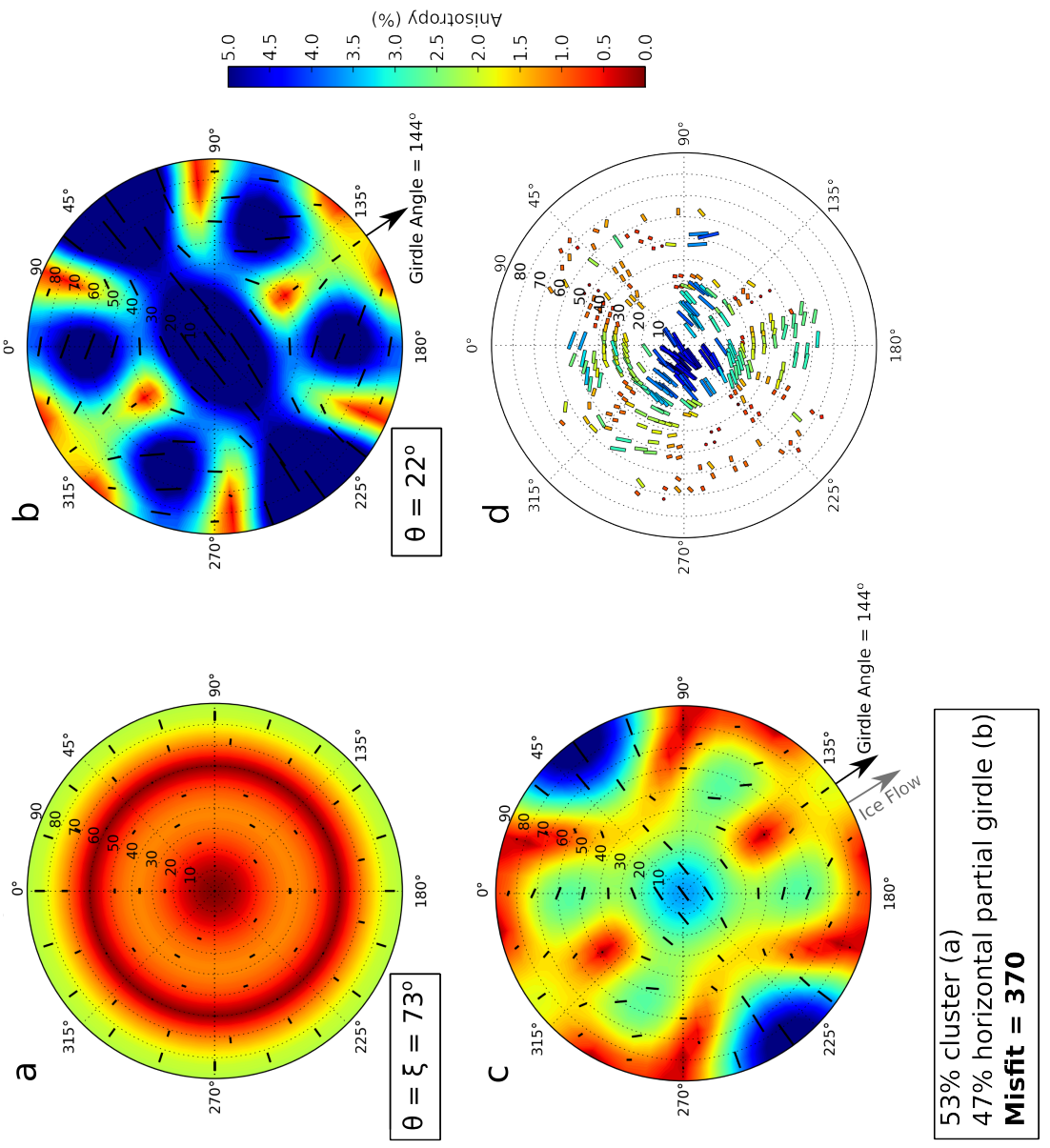

Figure 5.11: ***Result of inversion for a combination of horizontal partial girdle and cluster fabric on an upper hemisphere plot.*** *a) The cluster component of the best fit fabric mixture, it is a broad cluster with an opening angle of $\theta = 73°$. b) The horizontal partial girdle component of the best fit fabric mixture, with a narrow opening angle of $\theta = 22°$, orientated near orthogonal to the ice flow direction, with a girdle angle (pole to the girdle orientation) of 144°. c) The best fit mixed model, 53% cluster and 47% horizontal partial girdle. d) The smoothed SWS measurements for comparison.*

Horizontal Partial Girdle + Cluster

The third model is a combination of a horizontal partial girdle and a cluster fabric (Figure 5.11). The best fitting model is 53% cluster with an opening angle of $\theta = 73°$, and 47% horizontal partial girdle with a narrow opening angle of $\theta = 22°$, orientated near orthogonal to the ice flow direction at 144° relative to true North. This combined fabric (Figure 5.11c) provides a better fit to these data than the previous two models, with a significantly lower misfit value of 370. This overall misfit value is simply the sum of the length of the misfit vector for each inclination and azimuth bin, calculated by a vector subtraction of the modelled splitting parameters for that bin from the observed splitting parameters (Figure 5.12), the average misfit per measurement bin is low $\sim$ 1.2%. Figure 5.12 shows an overall good fit of the model to the data. The areas of worst fit are at high inclination ray paths and the strength of splitting in vertically travelling rays is somewhat underestimated.

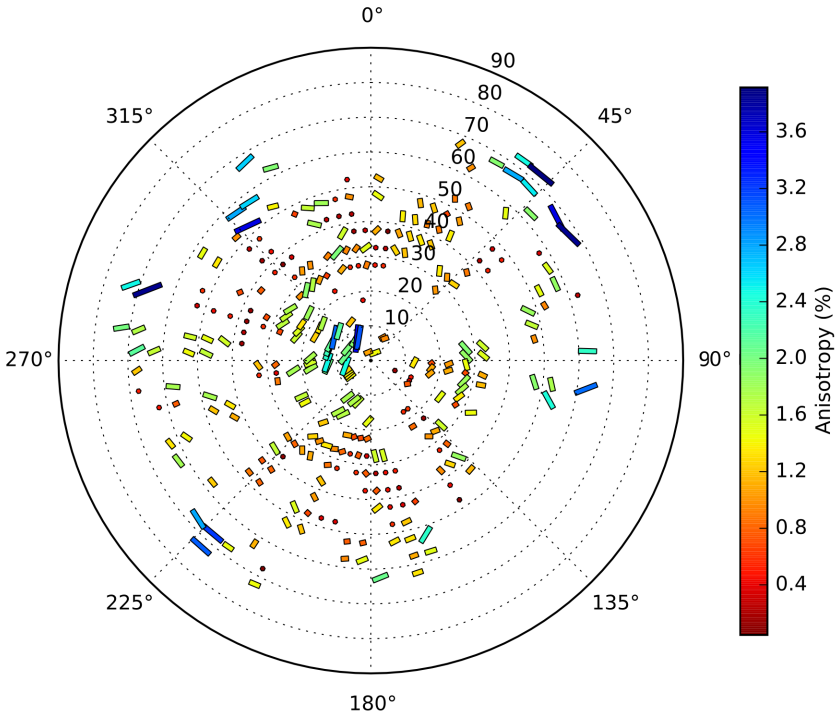

Figure 5.12: ***Residual error between modelled splitting parameters and observed splitting parameters for a combination of horizontal partial girdle and cluster fabric on an upper hemisphere plot.*** *The length of the bar represents the misfit value. High inclination rays show the worst fit to the data and the strength of splitting in vertical rays is somewhat underestimated. The overall misfit, sum of the length of all vectors shown is 370, this is $\sim$ 1.2% per measurement bin.*

Overlaying the measured values on this best fit model (Figure 5.13) allows the goodness of fit to be seen more clearly. For example, following the comparison made for the vertical partial girdle and a cluster fabric model, at an azimuth of 180° both the modelled and observed $\%A$ at an inclination of 50° and 40° match well, as does the orientation of the fast shear wave. The lobes of low $\%A$ at azimuths of 145 ° and 325° match the observed data well. The strength of $\%A$ for vertically travelling waves is still modelled a little low at around 3.7%, whereas the measured value is higher at around 4.5-5%.

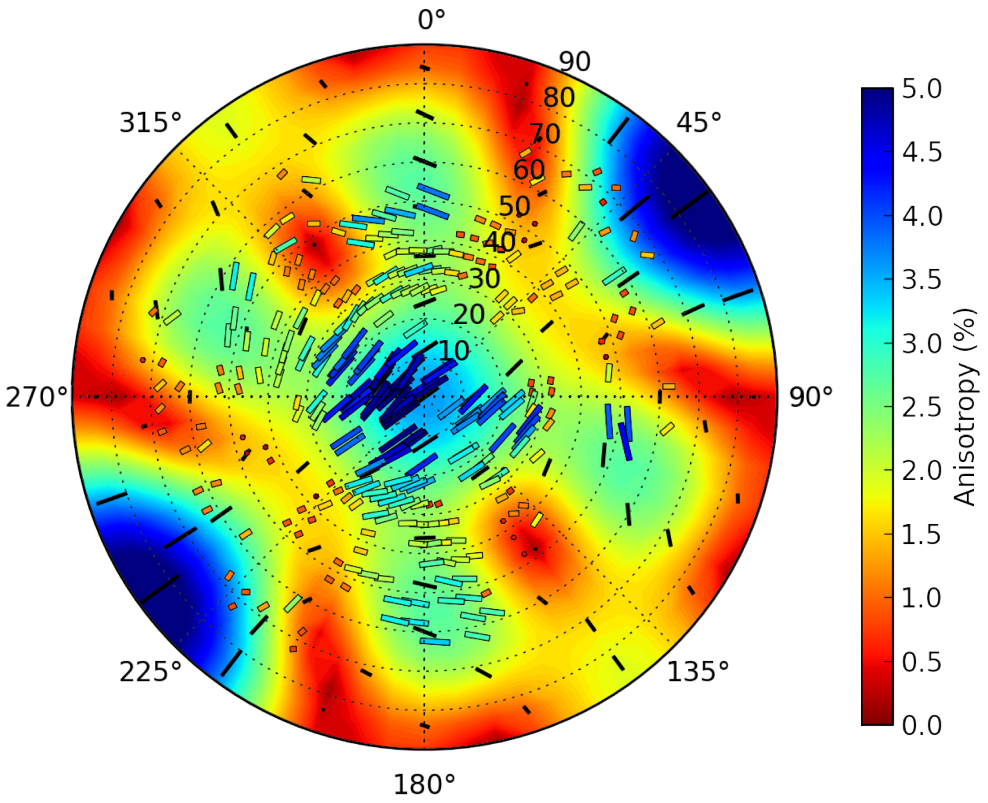

Figure 5.13: ***Best fitting ice fabric inversion with shear wave splitting measurements overlaid on an upper hemisphere plot.*** *An ice fabric model that is a combination of horizontal partial girdle (47%) and cluster fabric (53%) shows a good match to the SWS measurements in both orientation of the fast shear wave and strength of splitting. The areas of strongest modelled %A, high inclination rays at azimuths of 50° and 230°, show the worst fit to the data. However there are few measurements at these inclinations and high inclination measurements are likely to have a lower accuracy.*

The areas of strongest $\%A$ in the modelled data are for high inclination rays at azimuths of 50° and 230°, these appear to contradict the measurements, which show low $\%A$ in these regions.

However, it is worth noting that one of the assumptions when processing these data was that many of the arrivals would be near vertical, due to refraction in the low velocity surface firn layer. Therefore, the waveforms were not rotated into the ray frame before analysis. High inclinations rays will deviate most from this assumption and so the measurements at these inclinations are likely to be less reliable. There are also relatively few measurements at high inclinations and none above 73°, where the majority of the strong $\%A$ region is modelled, so it is is not possible to say with certainty how well the two compare in these areas.

5.4 Discussion

Measurements of shear wave splitting in this basal microseismic data set have shown that the dominant polarisation of the fast shear wave is perpendicular to the ice flow direction with maximum shear wave splitting occurring in the near vertical ray paths. The best fit model to the observed depth integrated pattern of splitting is a mixture of around equal proportions of a horizontal partial girdle (HPG) fabric and a broad cluster fabric. The HPG fabric has a tight opening angle of $\theta = 22°$ and is orientated across the ice flow direction, suggesting it was formed by a stress regime with strong longitudinal extension and lateral confinement. This is consistent with an ice stream environment where ice crystal c-axes rotate towards the axis of compression (the side walls of the ice stream) and away from the axis of extension (the ice flow direction), showing that the ice fabric is clearly influenced by the stress environment of ice stream flow.

The other half of the fabric mixture is a cluster fabric, with an opening angle of $\theta = 73°$. This is a weakly anisotropic fabric with a maximum $\%A$ of around 2% at near horizontal inclinations of 80° - 90° (Figure 5.11a). In fact the opening angle for the cluster is the same as that of the maximum inclination of SWS measurements made, suggesting it may be possible to fit an isotropic model (cone with $\theta = 90°$) to these data if any were available at these high inclinations. As the cluster is a weakly anisotropic fabric it essentially serves to weaken the $\%A$ of the mixed ice fabric and the pattern of anisotropy is largely influenced by the HPG fabric.

There are a number of explanations for the presence of a broad cluster fabric as a component of the resulting best fit mixture for this data set. In an ice stream environment a broad cluster fabric could exist as part of the ice fabric mixture, as a remnant fabric from a previous stress

regime that has not been completely modified by the ice stream flow. A broad cluster could also be formed in the shallow regions of this part of the ice stream as snow that falls in the area becomes compressed into ice. However, the firn layer is known to be around 100 m thick in this area of Rutford Ice Stream, which is only about 5% of the total ice thickness, whereas the broad cluster account for 53% of the fabric mixture. *Azuma* (1994) showed that simple shear at the ice-bed interface can cause a basal layer of cluster fabric to develop, however, clusters formed by simple shear are generally tight clusters with small opening angles. A thick basal layer of cluster fabric would cause shear waves split twice, by travelling through two different anisotropic mediums, and it is not obvious that this is the case from these data.

As the cluster is so broad, verging of isotropic, it could also be thought of as a component of the model that serves to weaken the total $\%A$ of the bulk ice fabric, which could come from a combination of different areas throughout the ice column. Thin layers of ice fabrics that are below the resolution of the seismic wavelength would serve to reduce the overall bulk anisotropy in the ice fabric. I have shown that the splitting measurements are stable over a range of frequencies but layering thinner than $\frac{\lambda}{8}$ (*Slack et al.*, 1993), around 5 m in this case, would not cause clear splitting but would reduce the strength of the bulk anisotropy. A weakening in the observed $\%A$ of the overall ice fabric could be due to the presence of impurities in the ice, for example, sediment in the basal layers or the presence of warm ice near the bed. Overall, the observed pattern of SWS in this area of Rutford Ice Stream appears to be largely controlled by an HPG fabric, which makes up 47% of the best fitting ice fabric mixture and is likely to be formed by ice flow in a laterally confined and longitudinally extensional ice stream environment. There is also a component of weak cluster, verging on isotropic fabric, which makes up 53% of the best fitting ice fabric and may have multiple origins.

A preliminary study on one day of this data set was made by *Harland et al.* (2013), using SWS measurements made on 41 basal microseismic events. *Harland et al.* (2013) suggested a mixture of a VTI and HTI fabric would best fit the observed pattern of splitting but they were not able to constrain the ice fabric model further with so few measurements. The study presented here uses 5951 measurements providing much better coverage of different azimuths and inclinations. I have also corrected a number of issues with the polarity of the waveforms (see Section 2.3.2) that would have given incorrect results for some of the measurements described by *Harland et al.* (2013). I have inverted for a number of ice CPO

fabrics using elasticity tensors to describe shear wave propagation through each CPO ice fabric. Using a purely intrinsic anisotropy model is a realistic representation of the expected cause of anisotropy in this area of Rutford Ice Stream, as we do not see any evidence of time varying anisotropy, which would suggest stress-sensitive cracks in the ice were contributing to the observed anisotropy.

5.5 Conclusions

I have made 5951 good quality shear wave splitting measurements on this data set, covering a large range of azimuths and inclinations out to 73°. I have inverted these measurements for a number of ice CPO fabrics commonly found in ice cores and introduced the idea of a horizontal partial girdle fabric, formed by extensional ice flow in a laterally confined environment. The best fit fabric model to these data is a horizontal partial girdle fabric mixed with a broad cluster which has a low degree of anisotropy, verging on isotropic. This produces a fabric where the pattern of splitting is largely influenced by the horizontal partial girdle fabric but with an overall reduced strength of shear wave splitting due to the cluster fabric. The presence of a horizontal partial girdle fabric indicates that the ice fabric in this region has deformed due to the stress environment of ice stream flow. This ice fabric should be taken into account when modelling the future response of Rutford Ice Stream as it will affect the ice rheology and thus ice flow in this region. Rutford Ice Stream is a typical convergent flow environment as therefore this finding also has implications for the modelling of ice stream flow in general.

This study has demonstrated that measurements of shear wave splitting in passive seismic data are a highly effective way to investigate ice CPO fabrics in an ice stream environment, where traditional techniques such as drilling ice cores are not possible. Passive seismic data produce strong shear waves at a large range of angles and azimuths making them well suited to studying the structure of polycrystaline ice fabrics. I have produced the first conclusive study of ice fabric in this area and shown that the ice is deforming as a result of flow in an ice stream environment. This result both informs the deformation history of this ice and provides a model of the rheological anisotropy to allow future ice stream flow to be better predicted and modelled.

Chapter 6

The Dynamics of Rutford Ice Stream

The aim of this chapter is to provide an overall synthesis of the dynamics of Rutford Ice Stream from passive microseismic observations. In Chapters 3-5, I have provided an analysis of the locations of 2967 basal microseismic events (Chapter 3), the source characteristics of the seismicity (Chapter 4) and a model of the ice fabric in this area of the ice stream from shear wave splitting analysis (Chapter 5). This chapter will bring together these elements to show the extent of the knowledge gained from this passive microseismic study and suggest an overall model of the flow dynamics of this area of Rutford Ice Stream.

6.1 The Dynamics of Rutford Ice Stream - Evidence from Basal Microseismicity

Rutford Ice Stream is a fast-flowing ice stream in West Antarctica which drains ∼48,000 km^2 of the West Antarctica Ice Sheet (WAIS) into the Ronne Ice Shelf. Understanding the factors that govern the movement of Rutford Ice Stream, both the basal motion and the internal ice fabric, is essential in order to better predict the future of the ice stream and the West Antarctic Ice Sheet as a whole.

Previous studies of the basal environment in this area of Rutford Ice Stream, ∼40 km upstream of the grounding line, have indicated that areas of high-porosity deforming sediment and lower porosity stiff sediment coexist beneath the ice stream. The hypocentral locations and source characteristics of naturally occurring basal microseismic events corroborate these ideas. Furthermore, they inform the dynamic characteristics of the ice-bed interface in this area. The material underlying this region of the ice stream is complex with motion of the overlying ice stream predominantly being accommodated aseismically, suggesting pervasive sediment deformation or well lubricated sliding dominates basal motion in this region. Small seismic 'stick spots', on the order of 10-20 m radius, have been located along a boundary (determined from independent seismic reflection and RES surveys) between deforming and stiff sediment (Figure 6.1). This suggests the change in basal conditions and sliding characteristics at this boundary may play a role in initiating the seismicity. There are a number 'sticky spots' located in stiff sediment areas beyond the boundary (Figure 6.1) indicating that the boundary may extend further downstream in these areas.

It has been shown that new bedforms beneath Rutford Ice Stream can be formed and eroded over periods of a few years (*Smith et al.*, 2007). The passive microseismic data set described in this study was only 32-days long and, not unexpectedly, the location of 'sticky spots' appears to be stable over this period. However, the type of information gained from this study shows that an extended passive seismic record would be a useful tool in investigating long term changes in basal characteristics by determining any change in the location or source mechanism of basal seismicity. Short term changes in the basal stress of Rutford Ice Stream are known to occur due to stress transmission of tidal forcing upstream of the grounding line (*Gudmundsson*, 2006; *Murray et al.*, 2007); causing a surface flow velocity variation of around ±10% on a periodic cycle of 14.77 days. Interestingly, there is no clear pattern in the overall seismic event rate correlating with this pattern of changing basal stress. This suggests that 'sticky spots' in this area are unaffected by changes in basal stress and that the stress changes may be transmitted upstream of the grounding line through the deforming sediment areas.

Two independent estimates of the direction of slip on 'sticky spots' have shown a trend of slip anticlockwise to the surface ice flow direction. This holds for a range of 'sticky spots' occurring at areas of varying bed topography at the base of the ice stream. *Smith et al.* (2007) showed that elongated drumlin-like bedforms in this area also deviate from the surface flow

direction, this hints at the idea that there are stresses at the base of the ice stream in this area causing a trend of basal slip to the east of the ice surface flow direction. A detailed study of the strike of bed-form features and spatial patterns in source polarisation would be needed to confirm this.

Basal microseismicity has been studied on other ice streams in Antarctica, probably the most well studied is Whillans Ice Stream (WIS) on the Siple Coast (Figure 1.1). Both WIS and Rutford Ice Stream are fast moving ice streams flowing into large ice shelves, the Ross and the Ronne respectively. Around 300 km upstream from the grounding line of WIS, in an area that is a similar in width and moving at similar velocity to my study area, there is evidence of a very similar basal dynamic to Rutford Ice Stream. Discrete 'sticky spots' slipping sub-horizontally in the ice flow direction are observed in this area of WIS. This indicates that this basal dynamic of movement accommodated predominantly by bed deformation with interspersed 'sticky spots' may be typical of flow in long, thin ice stream environments underlain by porous sediment. By contrast the downstream portion of WIS is made up of a large ice plain that moves by large scale stick-slip basal sliding twice daily (*Wiens et al.*, 2008; *Winberry et al.*, 2013) modulated by tidal forcing. During a stick-slip event the surface of the ice stream shoots forwards, accompanied by $\sim M_w$ 4 glacial earthquakes, a very different ice dynamic from the two bounded ice stream regions described above.

The lateral boundaries of Rutford Ice Stream and WIS are rather different, although they appear to exhibit similar basal dynamics and characteristics. Rutford Ice Stream has obvious topographically bounded margins, it occupies a deep trough between the Ellsworth Mountains to the West and the Fletcher Promontory to the East. The margins of the Siple Coast ice streams, such as WIS, are made up of slow moving ice and the areas of fast flowing ice are thought to be controlled by the presence of regions of deformable sediment at their base (*Studinger et al.*, 2001; *Peters et al.*, 2006). This can be seen in the BEDMAP2 image of Antarctica (Figure 1.1) where the Siple Coast is relatively flat compared to Rutford Ice Stream, which clearly occupies a topographic low.

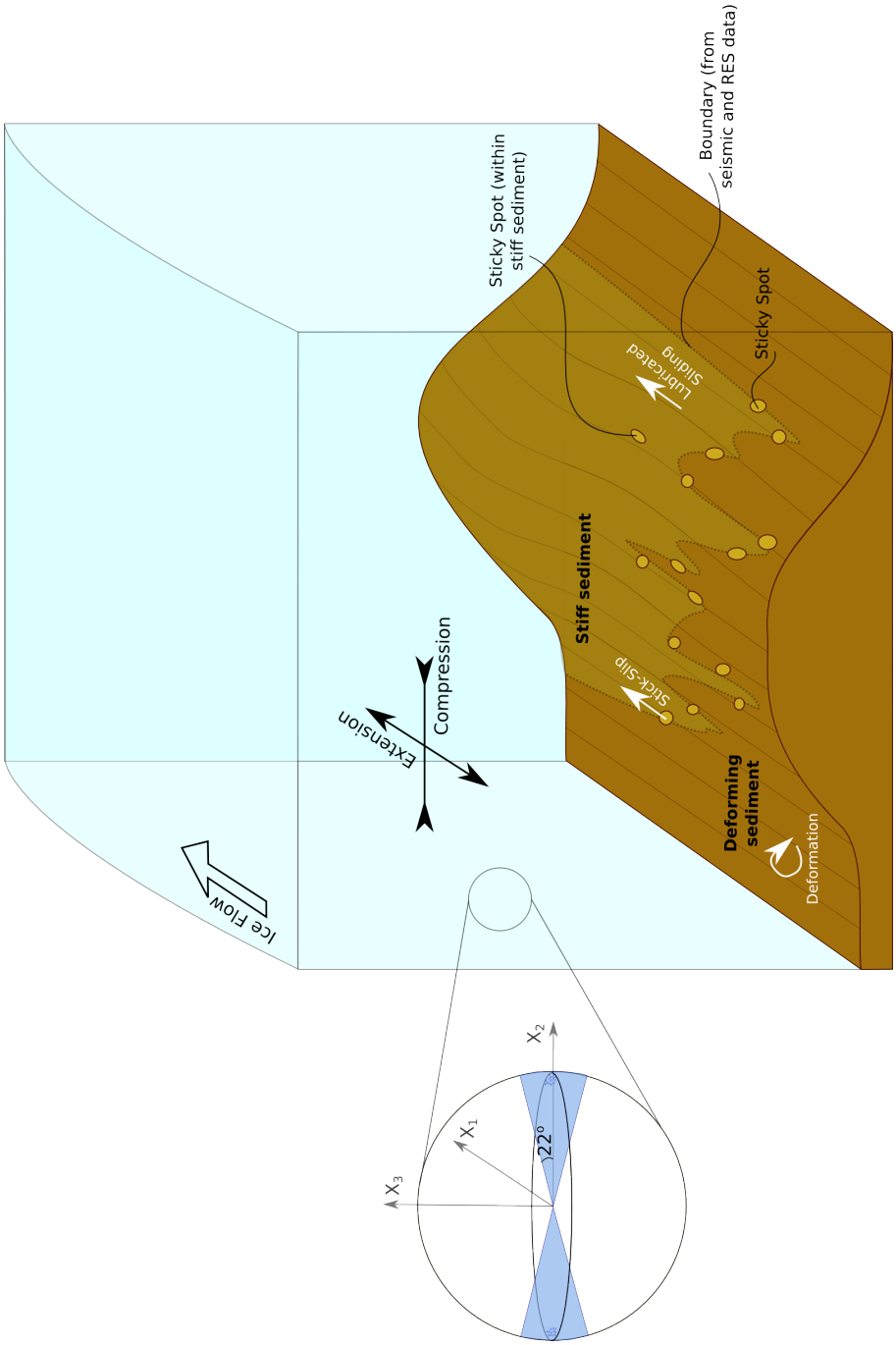

Figure 6.1: *Schematic model of the dynamics of Rutford Ice Stream.* *View looking downstream, showing the basal characteristics and internal ice fabric, the schematic is highly vertically exaggerated. The basal environment is interpreted to be made up of a mixture of deforming and stiff sediment, with the boundary between them being the location of microseismic 'sticky spots'. In this area of Rutford Ice Stream the ice is being extended in the ice flow direction and compressed by the side walls perpendicular to ice flow. This stress regime has formed a horizontal partial girdle ice fabric, orientated across the flow direction (in the X_2 plane) with an opening angle of $\theta = 22°$ towards the X_3 axis.*

The strict lateral confinement of Rutford Ice Stream is reflected in the ice crystal preferred orientation fabric at our study location. The ice fabric model, inverted from shear wave splitting measurements, shows a horizontal partial girdle fabric dominates the pattern of anisotropy in this area (Figure 6.1). This is strongly indicative of ice that is under lateral confinement and longitudinal extension (Figure 6.1), causing c-axes to rotate towards the axis of compression (the sides of the ice stream) and away from the direction of extension (along flow). In this location the ice has been flowing in a laterally bounded environment for around 200 km, and the resultant ice fabric is strongly influenced by this flow regime. There have been few studies of ice fabric in ice stream environments to date. A study on WIS, using active seismic surveying over Subglacial Lake Whillans (*Picotti et al.*, 2015), has shown the ice is made up of a broad VTI cone fabric with an opening angle of $\sim$73° and a low degree of anisotropy (an opening angle of 90° would indicate an isotropic fabric). Subglacial Lake Whillans is $\sim$50 km downstream of the main trunk of WIS, in an area where it merges with Mercer Ice Stream to form a broad low-slope ice plain. The ice in this region, as with our study area on Rutford Ice Stream, has travelled down an ice stream environment for several hundred kilometres. The fact that there is not a strong ice fabric resulting from laterally confined ice stream flow could suggest that the ice fabric in the ice bounded WIS is not as strongly influenced by lateral compression as the topographically bounded Rutford Ice Stream. It could also be the case that the ice fabric over Subglacial Lake Whillans was once similar to that found it Rutford Ice Stream, but that is has been modified by the change of stress regime on the ice plain, this would indicate that the ice fabric can change rapidly, over a distance of $\sim$50 km.

My study is this is the first conclusive study I am aware of that provides a robust model of ice stream fabric using shear wave splitting in microseismic data. It shows this method is a very effective tool for investigating ice fabric in a fast moving environment where drilling an ice core is not possible. I have also introduced a new category of ice fabric, the horizontal partial girdle, formed by strong horizontal confinement with longitudinal extension. Many of the commonly investigated ice fabrics in the literature thus far have been based upon those seen in ice cores, drilled at the interior of the ice sheet. There is a need for better understanding of ice fabric in a range of environments, in order to better understand both the deformation history of that ice and inform modelling of the response of that ice to future stresses.

Rutford Ice Stream is a typical convergent flow environment and it is likely that the fabric seen

here will be present in other fast-flowing ice streams. This presents a number of challenges to the ice flow modelling community: How best to parameterise anisotropic ice flow in order to reproduce the formation of a horizontal partial girdle fabric and how to model future ice flow in areas that contain such ice fabrics. The flow of ice is highly dependent on the type of ice fabric present and to neglect to represent this properly in models will lead to errors in predicted ice dynamics. For example, the rheology of a cluster fabric accomodates increased shear. *Wang et al.* (2003) was able to show how a speed up of ice flow leading to the onset of Bindschadler Ice Stream (Siple Coast) was due to the presence of a cluster CPO fabric, allowing greater basal shear and thus increased ice flow speed (*Hulbe et al.*, 2003). Girdle fabrics are less easily sheared than cluster fabrics but more easily accommodate transverse compression, hence they have been found to form at the onset of convergent flow environments (*Matsuoka et al.*, 2003). Current anisotropic ice flow models are able to recreate cluster and thick girdle fabrics, as well as anisotropic ice flow features such as Raymond Bumps (e.g. *Martín and Gudmundsson*, 2012; *Martín et al.*, 2014). However, more complex fabrics such as the horizontal partial girdle have not been recreated in flow models and it is unclear as to how such an ice fabric may affect future ice flow. Ice streams are the key to understanding ice discharge from Antarctica and therefore understanding how ice fabric affects the formation and flow of ice streams is of the utmost importance.

The initial aim of this study was to use passive microseismic monitoring to investigate ice stream basal dynamics and internal ice structure of Rutford Ice Stream, to better quantify the factors that govern ice stream flow. I have analysed a passive microseismic data set from Rutford Ice Stream recorded 40 km up stream from the grounding line, detecting and locating 2967 microseismic events at the ice-bed interface over the 32-day recording period (Chapter 3). The hypocentral locations and source characteristics of these data show that events originate at a number of discrete 'sticky spots' in the ice-bed interface, where the motion of the ice over its bed occurs by small magnitude sub-horizontal faulting (Chapter 4). This indicates ice is moving by basal sliding in these areas, which are largely located along the boundary between stiff and deforming sediment, interpreted from independent seismic reflection and RES studies. The material outside of these areas is accommodating ice stream motion aseismically, likely by pervasive sediment deformation. As the ice flows down the length of the ice stream a clear CPO fabric is formed that reflects the flow of ice in a laterally confined and longitudinally extensional environment (Chapter 5). Anisotropic ice

flow models must be improved to include this type of fabric if we are to better understand the evolution of ice streams, such a key component of ice sheet dynamics.

This study has shown the great range of knowledge that can be gained from this technique about both basal and internal ice dynamics. Passive microseismic monitoring also has the advantage of being a relatively logistically simple technique that does not require a huge number of work-hours to implement. This contrasts with drilling, coring and active seismic surveying, which are all highly labour intensive. Ideally a combination of these techniques would be used to investigate an ice stream environment, the key strengths that the passive seismic technique can bring are to provide a direct temporal and spatial record of ice-bed interactions and a strong source of shear waves, which are ideal for investigating seismic anisotropy.

References

Adalgeirsdóttir, G., A. M. Smith, T. Murray, M. A. King, K. Makinson, K. W. Nicholls, and A. E. Behar (2008), Tidal influence on Rutford Ice Stream, West Antarctica: observations of surface flow and basal processes from closely spaced GPS and passive seismic stations, *J. Glaciol.*, *54*, 715–724, doi:10.3189/002214308786570872.

Aki, K., and P. G. Richards (2002), *Quantitative Seismology*, University Science Books, Sausalito, CA.

Alley, R. B. (1988), Fabrics in polar ice sheets: development and prediction, *Science*, *240*(4851), 493–495, doi:10.1126/science.240.4851.493.

Alley, R. B. (1993), In search of ice-stream sticky spots, *J. Glaciol.*, *39*(133), 447–454.

Anandakrishnan, S., and R. B. Alley (1994), Ice Stream C, Antarctica , sticky spots detected by microearthquake monitoring, *Ann. Glaciol.*, *20*(1), 183–186, doi:10.3189/172756494794587276.

Anandakrishnan, S., and R. B. Alley (1997), Tidal forcing of basal seismicity of ice stream C, West Antarctica, observed far inland, *J. Geophys. Res.*, *102*(B7), 15,183–15,196, doi:10.1029/97JB01073.

Anandakrishnan, S., and C. R. Bentley (1993), Micro-earthquakes beneath Ice Streams B and C, West Antarctica: observations and implications, *J. Glaciol.*, *39*(133), 455–462.

Anandakrishnan, S., J. J. Fitzpatrick, R. B. Alley, A. J. Gow, and D. A. Meese (1994), Shear-wave detection of asymmetric c-axis fabrics in the GISP2 ice core, Greenland, *J. Glaciol.*, *40*(136), 491–496.

Ando, M., I. Ishikawa, and H. Wada (1980), S-wave anisotropy in the upper mantle under a volcanic area in Japan, *Nature*, *286*(5768), 43–46, doi:10.1038/286043a0.

Atre, S. R., and C. R. Bentley (1993), Laterally varying basal conditions beneath Ice Streams B and C, West Antarctica., *J. Glaciol.*, *39*(133), 507–514.

Atre, S. R., and C. R. Bentley (1994), Indication of a dilatant bed near Downstream B camp, Ice Stream B, Antarctica, *Ann. Glaciol.*, *20*(1), 177–182, doi:10.3189/172756494794587113.

Azuma, N. (1994), A flow law for anisotropic ice and its application to ice sheets, *Earth Planet. Sci. Lett.*, *128*(3-4), 601–614, doi:10.1016/0012-821X(94)90173-2.

Azuma, N., Y. Wang, K. Mori, H. Narita, T. Hondoh, H. Shoji, and O. Watanabe (1999), Textures and fabrics in the Dome F (Antarctica) ice core, *Ann. Glaciol.*, *29*(1), 163–168, doi:10.3189/172756499781821148.

Bamber, J. L., D. G. Vaughan, and I. Joughin (2000), Widespread complex flow in the interior of the Antarctic Ice Sheet, *Science*, *287*(5456), 1248–1250, doi:10.1126/science.287.5456.1248.

Bennett, H. F. (1968), An investigation into velocity anisotropy through measurements of ultrasonic wave velocities in snow and ice cores from Greenland and Antarctica, Ph.d. thesis, University of Wisconsin-Madison.

Bentley, C. R. (1971), Seismic Anisotropy in the West Antarctic Ice Sheet, in *Antarctic Snow and Ice Studies II*, vol. 16, edited by A. P. Crary, pp. 131–177, American Geophysical Union, doi:10.1029/AR016p0131.

Bentley, C. R. (1972), Seismic-wave velocities in anisotropic ice: A comparison of measured and calculated values in and around the deep drill hole at Byrd Station, Antarctica, *J. Geophys. Res.*, *77*(23), 4406–4420, doi:10.1029/JB077i023p04406.

Blankenship, D. D., C. R. Bentley, S. T. Rooney, and R. B. Alley (1986), Seismic measurements reveal a saturated porous layer beneath an active Antarctic ice stream, *Nature*, *322*(6074), 54–57, doi:10.1038/322054a0.

Blankenship, D. D., S. Anandakrishnan, J. L. Kempf, and C. R. Bentley (1987), Microearthquakes under and alongside Ice Stream B, Antarctica, detected by a new passive seismic array, *Ann. Glaciol.*, *9*, 30–34.

Brune, J. (1971), Correction to: Tectonic Stress and the Spectra, of Seismic Shear Waves from Earthquakes, *J. Geophys. Res.*, *76*(20), 1.

Brune, J. N. (1970), Tectonic Stress and the Spectra of Seismic Shear Waves from Earthquakes, *J. Geophys. Res.*, *75*(26), 4997–5009, doi:10.1029/JB075i026p04997/.

Budd, W., and T. Jacka (1989), A review of ice rheology for ice sheet modelling, *Cold Regions Science and Technology*, *16*(2), 107–144, doi:10.1016/0165-232X(89)90014-1.

Crampin, S. (1981), A review of wave motion in anisotropic and cracked elastic-media, *Wave Motion*, *3*(4), 343–391, doi:10.1016/0165-2125(81)90026-3.

Deichmann, N., J. Ansorge, F. Scherbaum, A. Aschwanden, F. Bernardi, and G. H. Gudmundsson (2000), Evidence for deep icequakes in an Alpine glacier, *Ann. Glaciol.*, *31*(1), 85–90, doi:10.3189/172756400781820462.

Diez, A., and O. Eisen (2015), Seismic wave propagation in anisotropic ice Part 1: Elasticity tensor and derived quantities from ice-core properties, *The Cryosphere*, *9*, 367–384, doi:10.5194/tc-9-367-2015.

Diez, A., O. Eisen, C. Hofstede, A. Lambrecht, C. Mayer, H. Miller, D. Steinhage, T. Binder, and I. Weikusat (2015), Seismic wave propagation in anisotropic ice Part 2: Effects of crystal anisotropy in geophysical data, *The Cryosphere*, *9*, 385–398, doi:10.5194/tc-9-385-2015.

Doake, C. S. M., R. M. Frolich, D. R. Mantripp, A. M. Smith, and D. G. Vaughan (1987), Glaciological studies on Rutford Ice Stream, Antarctica, *J. Geophys. Res.*, *92*(B9), 8951–8960, doi:10.1029/JB092iB09p08951.

Doake, C. S. M., H. F. J. Corr, A. Jenkins, K. Makinson, K. W. Nicholls, C. Nath, A. M. Smith, and D. G. Vaughan (2001), Rutford Ice Stream, Antarctica, in *The West Antarctic Ice Sheet: Behavior and Environment*, *Antarct. Res. Ser.*, vol. 77, edited by R. B. Alley and R. A. Bindschadler, pp. 221–235, AGU, Washington, DC, doi:10.1029/AR077p0221.

Dreger, D. S., and B. Woods (2002), Regional distance seismic moment tensors of nuclear explosions, *Tectonophysics*, *356*(1-3), 139–156, doi:10.1016/S0040-1951(02)00381-5.

Dreger, D. S., H. Tkalcic, and M. Johnston (2000), Dilational processes accompanying earthquakes in the Long Valley Caldera, *Science*, *288*(5463), 122–125, doi:10.1126/science.288.5463.122.

Drew, J., R. S. White, F. Tilmann, and J. Tarasewicz (2013), Coalescence microseismic mapping, *Geophys. J. Int.*, *195*(3), 1773–1785, doi:10.1093/gji/ggt331.

Drews, R., C. Martín, D. Steinhage, and O. Eisen (2013), Characterizing the glaciological conditions at Halvfarryggen ice dome, Dronning Maud Land, Antarctica, *J. Glaciol.*, *59*(213), 9–20, doi:10.3189/2013JoG12J134.

Durand, G., O. Gagliardini, T. Thorsteinsson, A. Svensson, S. Kipfstuhl, and D. Dahl-Jensen (2006), Ice microstructure and fabric: an up-to-date approach for measuring textures, *J. Glaciol.*, *52*(179), 619–630, doi:10.3189/172756506781828377.

Duval, P., M. F. Ashby, and I. Andermant (1983), Rate-Controlllng Processes in the Creep of Polycrystalline Ice, *J. Phys. Chem.*, *87*(21), 4066–4074, doi:10.1021/j100244a014.

Eisen, O., I. Hamann, S. Kipfstuhl, D. Steinhage, and F. Wilhelms (2007), Direct evidence for continuous radar reflector originating from changes in crystal-orientation fabric, *The Cryosphere*, *1*(1), 1–10, doi:10.5194/tc-1-1-2007.

Ekström, G., M. Nettles, and G. A. Abers (2003), Glacial earthquakes, *Science*, *302*(622), 622–624, doi:10.1126/science.1088057.

El-Isa, Z. H., and D. W. Eaton (2014), Spatiotemporal variations in the b -value of earthquake magnitude frequency distributions: Classification and causes, *Tectonophysics*, *615-616*, 1–11, doi:10.1016/j.tecto.2013.12.001.

Engelhardt, H., N. Humphrey, B. Kamb, and M. Fahnestock (1990), Physical conditions at the base of a fast moving Antarctic ice stream, *Science*, *248*(4951), 57–59, doi:10.1126/science.248.4951.57.

Eshelby, J. D. (1957), The determination of the elastic field of an ellipsoisal inclusion, and related problems, *Proc. R. Soc.*, *241*(1226), 376–196, doi:10.1098/rspa.1957.0133.

Faria, S. H., I. Weikusat, and N. Azuma (2014a), The microstructure of polar ice. Part I: Highlights from ice core research, *J. Struct. Geol.*, *61*, 2–20, doi:10.1016/j.jsg.2013.09.010.

Faria, S. H., I. Weikusat, and N. Azuma (2014b), The microstructure of polar ice. Part II: State of the art, *J. Struct. Geol.*, *61*, 21–49, doi:10.1016/j.jsg.2013.11.003.

Fretwell, P., H. D. Pritchard, D. G. Vaughan, J. L. Bamber, N. E. Barrand, R. Bell, C. Bianchi, R. G. Bingham, D. D. Blankenship, G. Casassa, G. Catania, D. Callens, H. Conway, A. J. Cook, H. F. J. Corr, D. Damaske, V. Damm, F. Ferraccioli, R. Forsberg, S. Fujita, Y. Gim, P. Gogineni, J. A. Griggs, R. C. A. Hindmarsh, P. Holmlund, J. W. Holt, R. W. Jacobel, A. Jenkins, W. Jokat, T. Jordan, E. C. King, J. Kohler, W. Krabill, M. Riger-Kusk, K. A. Langley, G. Leitchenkov, C. Leuschen, B. P. Luyendyk, K. Matsuoka, J. Mouginot, F. O. Nitsche, Y. Nogi, O. A. Nost, S. V. Popov, E. Rignot, D. M. Rippin, A. Rivera, J. Roberts, N. Ross, M. J. Siegert, A. M. Smith, D. Steinhage, M. Studinger, B. Sun, B. K. Tinto, B. C. Welch, D. Wilson, D. A. Young, C. Xiangbin, and A. Zirizzotti (2013), Bedmap2: improved ice bed, surface and thickness datasets for Antarctica, *The Cryosphere*, *7*, 375–393, doi:10.5194/tc-7-375-2013.

Frolich, R., D. R. Mantripp, D. G. Vaughan, and C. S. M. Doake (1987), Force balance of Rutford Ice Stream , Antarctica, in *The Physical Basis of Ice Sheet Modelling (Proceedings of the Vancouver Symposium)*, June, pp. 323–331.

Frolich, R. M., and C. S. M. Doake (1988), Relative importance of lateral and vertical shear of Rutford Ice Stream, Antarctica, *Ann. Glaciol.*, *11*, 19–22.

Fujita, S., H. Maeno, and K. Matsuoka (2006), Radio-wave depolarization and scattering within ice sheets : a matrix-based model to link radar and ice-core measurements and its application, *J. Glaciol.*, *52*(178), 407–424, doi:10.3189/172756506781828548.

Gow, A. J. (1967), Preliminary results of studies of ice cores from the 2164 m deep drill hole, Byrd Station, Antarctica, in *International Symposium on Antarctic Glaciological Exploration (ISAGE)*, pp. 77–90, Cambridge (Pub. No. 86 of IASH), Hanover, New Hampshire, USA.

Gow, A. J., and T. Williamson (1976), Rheological implications of the internal structure and crystal fabrics of the West Antarctic ice sheet as revealed by deep core drilling at Byrd Station, *Gel. Soc. Am. Bull.*, *87*(12), 1665–1677.

Gudmundsson, G. H. (2006), Fortnightly variations in the flow velocity of Rutford Ice Stream, West Antarctica., *Nature*, *444*(7122), 1063–1064, doi:10.1038/nature05430.

Gudmundsson, G. H. (2007), Tides and the flow of Rutford Ice Stream, West Antarctica, *J. Geophys. Res.*, *112*(F4), 1–8, doi:10.1029/2006JF000731.

Gudmundsson, G. H. (2011), Ice-stream response to ocean tides and the form of the basal sliding law, *The Cryosphere*, *5*, 259–270, doi:10.5194/tc-5-259-2011.

Gudmundsson, G. H., and A. Jenkins (2009), Ice-flow velocities on Rutford Ice Stream, West Antarctica, are stable over decadal timescales, *J. Glaciol.*, *55*(190), 339–344, doi:10.3189/002214309788608697.

Gusmeroli, A., E. C. Pettit, J. H. Kennedy, and C. Ritz (2012), The crystal fabric of ice from full-waveform borehole sonic logging, *J. Geophys. Res.*, *117*(F03021), 1–13, doi:10.1029/2012JF002343.

Gutenberg, B., and C. Richter (1944), Frequency of Earthquakes in California, *Bull. Seismol. Soc. Am.*, *34*, 185–188.

Hanks, T. C., and H. Kanamori (1979), A moment magnitude scale, *J. Geophys. Res.*, *84*(B5), 2348–2350, doi:10.1029/JB084iB05p02348.

Hanks, T. C., and W. Thatcher (1972), A graphical representation of seismic source parameters, *J. Geophys. Res.*, *77*(23), 4393–4405, doi:10.1029/JB077i023p04393.

Harland, S. R., J. M. Kendall, G. W. Stuart, G. E. Lloyd, A. F. Baird, A. M. Smith, H. D. Pritchard, and A. M. Brisbourne (2013), Deformation in Rutford Ice Stream, West Antarctica: measuring shear-wave anisotropy from icequakes, *Ann. Glaciol.*, *54*(64), 105–114, doi:10.3189/2013AoG64A033.

Helmstetter, A., B. Nicolas, P. Comon, and M. Gay (2015), Basal icequakes recorded beneath an Alpine glacier (Glacier dArgentière, Mont Blanc, France): Evidence for stick-slip motion?, *J. Geophys. Res. Earth Surf.*, *120*, 379–401, doi:10.1002/2014JF00328.

Hofstede, C., O. Eisen, A. Diez, D. Jansen, Y. Kristoffersen, A. Lambrecht, and C. Mayer (2013), Investigating englacial reflections with vibro- and explosive-seismic surveys at Halvfarryggen ice dome, Antarctica, *Ann. Glaciol.*, *54*(64), 189–200, doi: 10.3189/2013AoG64A064.

Horgan, H. J., S. Anandakrishnan, R. B. Alley, L. E. Peters, G. P. Tsoflias, D. E. Voigt, and J. P. Winberry (2008), Complex fabric development revealed by englacial seismic reflectivity: Jakobshavn Isbræ, Greenland, *Geophys. Res. Lett.*, *35*(L10501), 1–6, doi: 10.1029/2008GL033712.

Horgan, H. J., S. Anandakrishnan, R. B. Alley, P. G. Burkett, and L. E. Peters (2011), Englacial seismic reflectivity: imaging crystal-orientation fabric in West Antarctica, *J. Glaciol.*, *57*(204), 639–650, doi:10.3189/002214311797409686.

Hulbe, C. L., W. Wang, I. R. Joughin, M. J. Siegert, C. L. Hulbe, W. Wang, I. R. Joughin, and M. J. Siegert (2003), The role of lateral and vertical shear in tributary flow toward a West Antarctic ice stream, *Ann. Glaciol.*, *36*, 244–250, doi:10.3189/172756403781816194.

Joughin, I., and J. L. Bamber (2005), Thickening of the ice stream catchments feeding the Filchner-Ronne Ice Shelf, Antarctica, *Geophys. Res. Lett.*, *32*(17), 1–4, doi: 10.1029/2005GL023844.

King, E. C., R. C. A. Hindmarsh, and C. R. Stokes (2009), Formation of mega-scale glacial lineations observed beneath a West Antarctic ice stream, *Nat. Geosci.*, *2*, 585–588, doi: 10.1038/NGEO581.

King, M. A., T. Murray, and A. M. Smith (2010), Non-linear responses of Rutford Ice Stream, Antarctica, to semi-diurnal and diurnal tidal forcing, *J. Glaciol.*, *56*(195), 167–176, doi: 10.3189/002214310791190848.

Kohnen, H. (1974), The temperature dependence of seismic waves in ice, *J. Glaciol.*, *13*(67), 144–147.

Kohnen, H., and A. J. Gow (1979), Ultrasonic velocity investigations of crystal anisotropy in deep ice cores from Antarctica, *J. Geophys. Res.*, *84*(C8), 4865–4874.

Lemke, P., J. Ren, R. B. Alley, I. Allison, J. Carrasco, G. Flato, Y. Fujii, G. Kaser, P. Mote, R. H. Thomas, and T. Zhang (2007), Observations: Changes in snow, ice and frozen ground, in *Climate Change 2007: The Physical Science Basis. Contribution of Working Group I to the Fourth Assessment Report of the Intergovernmental Panel on Climate Change*, edited

by D. Qin, M. Manning, Z. Chen, M. Marquis, K. B. Averyt, M. Tignor, and H. L. Miller, pp. 337–384, Cambridge University Press.

Lipenkov, V. Y., N. I. Barkov, P. Duval, and P. Pimienta (1989), Crystalline texture of the 2083 m ice core at Vostok Station, Antarctica, *J. Glaciol.*, *35*(121), 392–398.

Lomax, A., J. Virieux, P. Volant, and C. Berge-Thierry (2000), Probabilistic earthquake location in 3D and layered models: Introduction of a Metropolis-Gibbs method and comparison with linear locations, in *Advances in Seismic Event Location*, edited by C. H. Thurber and N. Rabinowitz, pp. 101–134, Kluwer, Amsterdam.

Martín, C., and G. H. Gudmundsson (2012), Effects of nonlinear rheology, temperature and anisotropy on the relationship between age and depth at ice divides, *The Cryosphere*, *6*(5), 1221–1229, doi:10.5194/tc-6-1221-2012.

Martín, C., G. H. Gudmundsson, H. D. Pritchard, and O. Gagliardini (2009), On the effects of anisotropic rheology on ice flow, internal structure, and the age-depth relationship at ice divides, *J. Geophys. Res.*, *114*(F04001), 1–18, doi:10.1029/2008JF001204.

Martín, C., G. H. Gudmundsson, and E. C. King (2014), Modelling of Kealey Ice Rise, Antarctica, reveals stable ice-flow conditions in East Ellsworth Land over millennia, *J. Glaciol.*, *60*(219), 139–146, doi:10.3189/2014JoG13J089.

Matsuoka, K., T. Furukawa, S. Fujita, H. Maeno, S. Uratsuka, R. Naruse, and O. Watanabe (2003), Crystal orientation fabrics within the Antarctic ice sheet revealed by a multipolarization plane and dual-frequency radar survey, *J. Geophys. Res.*, *108*(B10), 1–17, doi:10.1029/2003JB002425.

Matsuoka, K., D. Power, S. Fujita, and C. F. Raymond (2012), Rapid development of anisotropic ice-crystal-alignment fabrics inferred from englacial radar polarimetry, central West Antarctica, *J. Geophys. Res.*, *117*(F03029), 1–16, doi:10.1029/2012JF002440.

Maurel, A., F. Lund, and M. Montagnat (2015), Propagation of elastic waves through textured polycrystals: application to ice, *Proc. R. Soc.*, *471*(2177), 1–28, doi:10.1098/rspa.2014.0988.

Mercer, J. H. (1978), West Antarctica ice sheet and CO2 greenhouse effect: a threat of disaster, *Nature*, *271*, 321–325,, doi:10.1038/271321a0.

Mikesell, T. D., K. Van Wijk, M. M. Haney, J. H. Bradford, H. P. Marshall, and J. T. Harper (2012), Monitoring glacier surface seismicity in time and space using Rayleigh waves, *J. Geophys. Res.*, *117*(F02020), 1–12, doi:10.1029/2011JF002259.

Murray, T., A. M. Smith, M. A. King, and G. P. Weedon (2007), Ice flow modulated by tides at up to annual periods at Rutford Ice Stream, West Antarctica, *Geophys. Res. Lett.*, *34*(L18503), 1–6, doi:10.1029/2007GL031207.

Murray, T., H. Corr, A. Forieri, and A. M. Smith (2008), Contrasts in hydrology between regions of basal deformation and sliding beneath Rutford Ice Stream, West Antarctica, mapped using radar and seismic data, *Geophys. Res. Lett.*, *35*(L12504), 1–5, doi:10.1029/2008GL033681.

Murray, T., M. Nettles, N. Selmes, L. M. Cathles, J. C. Burton, T. D. James, S. Edwards, I. Martin, T. O'Farrell, R. Aspey, I. Rutt, and T. Bauge (2015), Reverse glacier motion during iceberg calving and the cause of glacial earthquakes, *Science*, *349*(6245), 305–306, doi:10.1126/science.aab0460.

Neave, K. G., and J. C. Savage (1970), Icequakes on the Athabasca Glacier, *J. Geophys. Res.*, *75*(8), 1351–1362, doi:10.1029/JB075i008p01351.

Nippress, S. E. J., A. Rietbrock, and A. E. Heath (2010), Optimized automatic pickers: application to the ANCORP data set, *Geophys. J. Int.*, *181*(2), 911–925, doi:10.1111/j.1365-246X.2010.04531.x.

Paterson, W. S. B. (1994), *The Physics of Glaciers*, 3rd ed., 480 pp., Pergamon, New York.

Peters, L. E., S. Anandakrishnan, R. B. Alley, J. P. Winberry, D. E. Voigt, A. M. Smith, and D. L. Morse (2006), Subglacial sediments as a control on the onset and location of two Siple Coast ice streams, West Antarctica, *J. Geophys. Res.*, *111*(B1), B01,302, doi:10.1029/2005JB003766.

Peters, L. E., S. Anandakrishnan, R. B. Alley, and D. E. Voigt (2012), Seismic attenuation in glacial ice: A proxy for englacial temperature, *J. Geophys. Res.*, *117*(F03008), 1–10, doi:10.1029/2011JF002201.

Pettit, E. C., T. Thorsteinsson, H. P. Jacobson, and E. D. Waddington (2007), The role of crystal fabric in flow near an ice divide, *J. Glaciol.*, *53*(181), 277–288, doi:10.3189/172756507782202766.

Picotti, S., A. Vuan, J. M. Carcione, H. J. Horgan, and S. Anandakrishnan (2015), Anisotropy and crystalline fabric of Whillans Ice Stream (West Antarctica) inferred from multicomponent seismic data, *J. Geophys. Res. Solid Earth*, *120*(6), 4237–4262, doi:10.1002/2014JB011591.

Pratt, M. J., J. P. Winberry, D. A. Wiens, S. Anandakrishnan, and R. B. Alley (2014), Seismic and geodetic evidence for grounding-line control of Whillans Ice Stream stick-slip events, *J. Geophys. Res. Earth Surf.*, *119*(2), 333–348, doi:10.1002/2013JF002842.

Pritchard, H., A. Brisbourne, E. King, G. Gudmundsson, and A. Smith (2009), Scientific Report : Gauging Rutford Ice Stream Transients (GRIST), *Tech. rep.*, British Antarctic Survey.

Raymond, C. F. (1983), Deformation in the vicinity of ice divides, *J. Glaciol.*, *29*(103), 357–373.

Reasenburg, P., and D. H. Oppenheimer (1985), FPFIT, FPPLOT and FPPAGE; Fortran computer programs for calculating and displaying earthquake fault-plane solutions, *Tech. rep.*, USGS Open-File Report.

Rial, J. A., C. Tang, and K. Steffen (2009), Glacial rumblings from Jakobshavn ice stream, Greenland, *J. Glaciol.*, *55*(191), 389–399.

Rignot, E. (1998), Radar interferometry detection of hinge-line migration on Rutford Ice Stream and Carlson Inlet , Antarctica, *Ann. Glaciol.*, *27*, 25–32.

Rignot, E., I. Velicogna, M. R. van den Broeke, A. Monaghan, and J. T. M. Lenaerts (2011), Acceleration of the contribution of the Greenland and Antarctic ice sheets to sea level rise, *Geophys. Res. Lett.*, *38*, 1–5, doi:10.1029/2011GL046583.

Roethlisberger, H. (1955), Studies in glacier physics on the Penny Ice Cap, Baffin Island, 1953, Part III: Seismic Sounding, *J. Glaciol.*, *2*(18), 539–552, doi:10.3189/002214355793702064.

Roethlisberger, H. (1972), Seismic Exploration in Cold Regions, in *Cold Regions Science and Engineering Monograph 11-A 2a*, Cold Reg. Res. and Eng. Lab., Hannover, N. H.

Rosier, S. H. R., G. H. Gudmundsson, and J. A. M. Green (2014), Insights into ice stream dynamics through modelling their response to tidal forcing, *The Cryosphere*, *8*(5), 1763–1775, doi:10.5194/tc-8-1763-2014.

Rosier, S. H. R., G. H. Gudmundsson, and J. A. M. Green (2015), Temporal variations in the flow of a large Antarctic ice stream controlled by tidally induced changes in the subglacial water system, *The Cryosphere*, *9*(4), 1649–1661, doi:10.5194/tc-9-1649-2015.

Savage, M. K. (1999), Seismic anisotropy and mantle deformation: What have we learned from shear wave splitting?, *Rev. Geophys.*, *37*(1), 65–106, doi:10.1029/98RG02075.

Scherer, R. P., A. Aldahan, S. Tulaczyk, H. Engelhardt, and B. Kamb (1998), Pleistocene collapse of the West Antarctic Ice Sheet, *Science*, *281*(5373), 82–85, doi:10.1126/science.281.5373.82.

Schytt, V. (1958), Snow and ice studies in Antarctica, in *Norwegian-British-Swedish Antarctic Expedition, 1949-1952, Scientific Results. Glaciology II, Vol 4.*, Norsk Polarinstitutt/University of Stockholm, Oslo. Ph.D. Thesis.

Silver, P. G., and W. W. Chan (1991), Shear wave splitting and subcontinental mantle deformation, *J. Geophys. Res.*, *96*(B10), 16,429–16,454, doi:10.1029/91JB00899.

Slack, R. D., D. A. Ebrom, J. A. McDonald, and R. H. Tatham (1993), Thin layers and shear-wave splitting, *Geophysics*, *58*(10), 1468–1480, doi:10.1190/1.1443361.

Smith, A. (1997a), Basal conditions on Rutford Ice Stream, West Antarctica, from seismic observations, *J. Geophys. Res.*, *102*(B1), 543–552, doi:10.1029/96JB02933.

Smith, A. M. (1994), Introduction to high resolution seismic surveys on Rutford Ice Stream, in *Filchner-Ronne Ice Shelf Programme Report No. 7*, pp. 39–40, Alfred-Wegener Inst. for Polar and Mar. Res., Alfred-Wegener Inst. for Polar and Mar. Res., Bremerhaven, Germany.

Smith, A. M. (1997b), Variations in basal conditions on Rutford Ice Stream, West Antarctica, *J. Glaciol.*, *43*(144), 245–255.

Smith, A. M. (2006), Microearthquakes and subglacial conditions, *Geophys. Res. Lett.*, *33*, 1–5, doi:10.1029/2006GL028207.

Smith, A. M., and T. Murray (2009), Bedform topography and basal conditions beneath a fast-flowing West Antarctic ice stream, *Quat. Sci. Rev.*, *28*(7-8), 584–596, doi:10.1016/j.quascirev.2008.05.010.

Smith, A. M., T. Murray, K. W. Nicholls, K. Makinson, G. Aalgeirsdóttir, A. E. Behar, and D. G. Vaughan (2007), Rapid erosion, drumlin formation, and changing hydrology beneath an Antarctic ice stream, *Geology*, *35*(2), 127–130, doi:10.1103/G23036A.

Smith, E. C., A. M. Smith, R. S. White, A. M. Brisbourne, and H. D. Pritchard (2015), Mapping the ice-bed interface characteristics of Rutford Ice Stream , West Antarctica, using microseismicity, *J. Geophys. Res. Earth Surf.*, *120*(9), 1881–1894, doi:doi:10.1002/2015JF003587.

Stephenson, S. N. (1984), Glacier flexure and the position of grounding line: Measurements by tilmeter on Rutford Ice Stream, Antarctica, *Ann. Glaciol.*, *5*, 165–169.

Stephenson, S. N., and C. S. M. Doake (1982), Dynamic behaviour of Rutford Ice Stream, *Ann. Glaciol.*, *3*, 295–299.

Stephenson, S. N., C. S. M. Doake, and J. A. C. Horsfall (1979), Tidal flexure of ice shelves measured by tiltmeter, *Nature*, *282*(5738), 496–497, doi:10.1038/282496a0.

Storn, R., and K. Price (1997), Differential Evolution A simple and efficient heuristic for global optimization over continuous spaces, *J. Global Optim.*, *11*(4), 341–359, doi:10.1023/A:1008202821328.

Stuart, G., T. Murray, A. M. Brisbourne, P. Styles, and S. Toon (2005), Seismic emissions from a surging glacier: Bakaninbreen, Svalbard, *Ann. Glaciol.*, *42*, 151–157, doi:10.3189/172756405781812538.

Studinger, M., R. E. Bell, D. D. Blankenship, A. Carol, R. A. Arko, D. L. Morse, and I. Joughin (2001), Subglacial sediments: A regional geological template for ice flow in West Antarctica, *Geophys. Res. Lett.*, *28*(18), 3493–3496, doi:10.1029/2000GL011788.

Teanby, N. A., J. M. Kendall, and M. van der Baan (2004), Automation of shear-wave splitting measurements using cluster analysis, *Bull. Seismol. Soc. Am.*, *94*(2), 453–463, doi:10.1785/0120030123.

Thelen, W. A., K. Allstadt, S. De Angelis, S. D. Malone, S. C. Moran, and J. Vidale (2013), Shallow repeating seismic events under an alpine glacier at Mount Rainier, Washington, USA, *J. Glaciol.*, *59*(214), 345–356, doi:10.3189/2013JoG12J111.

Thompson, J., M. Simons, and V. C. Tsai (2014), Modeling the elastic transmission of tidal stresses to great distances inland in channelized ice streams, *The Cryosphere*, *8*(6), 2007–2029, doi:10.5194/tc-8-2007-2014.

Tol, R. S., M. Bohn, T. E. Downing, M. Guillerminet, E. Hizsnyik, R. Kasperson, K. Lonsdale, C. Mays, R. J. Nicholls, A. A. Olsthoorn, G. Pfeifle, M. Poumadere, F. L. Toth, A. T. Vafeidis, P. E. van der Werff, and I. H. Yetkiner (2006), Adaptation to five metres of sea level rise, *J. Risk Res.*, *9*(5), 467–482, doi:10.1080/13669870600717632.

Tsai, V. C., and G. Ekström (2007), Analysis of glacial earthquakes, *J. Geophys. Res.*, *112*(F3), 1–13, doi:10.1029/2006JF000596.

Tsai, V. C., J. R. Rice, and M. Fahnestock (2008), Possible mechanisms for glacial earthquakes, *J. Geophys. Res.*, *113*(F3), 1–17, doi:10.1029/2007JF000944.

Vaughan, D. G., H. F. J. Corr, C. S. M. Doake, and E. D. Waddington (1999), Distortion of isochronous layers in ice revealed by ground-penetrating radar, *Nature*, *398*(6725), 323–326, doi:10.1038/18653.

Vaughan, D. G., A. M. Smith, P. C. Nath, and E. Le Meur (2003), Acoustic impedance and basal shear stress beneath four Antarctic ice streams, *Ann. Glaciol.*, *36*, 225–232, doi:10.3189/172756403781816437.

Voigt, W. (1910), *Lehrbuch der Kristallphysik: (mit Ausschluss der Kristalloptik)*, 964 pp., B. G. Teubner, Leipzig.

Wadati, K. (1933), On the travel time of earthquake waves, Part II, *Geophys. Mag.*, *7*, 101–111.

Waldhauser, F., and W. L. Ellsworth (2000), A double-difference earthquake location algorithm: method and application to the northern hayward fault, California, *Bull. Seismol. Soc. Am.*, *90*(6), 1353–1368, doi:10.1785/0120000006.

Walter, F., N. Deichmann, and M. Funk (2008), Basal icequakes during changing subglacial water pressures beneath Gornergletscher, Switzerland, *J. Glaciol.*, *54*(186), 511–521, doi:10.3189/002214308785837110.

Walter, F., J. F. Clinton, N. Deichmann, D. S. Dreger, S. E. Minson, and M. Funk (2009), Moment tensor inversions of icequakes on Gornergletscher, Switzerland, *Bull. Seismol. Soc. Am.*, *99*(2A), 852–870, doi:10.1785/0120080110.

Walter, F., D. S. Dreger, J. F. Clinton, N. Deichmann, and M. Funk (2010), Evidence for near-horizontal tensile faulting at the base of Gornergletscher, a Swiss Alpine glacier, *Bull. Seismol. Soc. Am.*, *100*(2), 458–472, doi:10.1785/0120090083.

Walter, F., J. M. Amundson, S. O'Neel, M. Truffer, M. Fahnestock, and H. A. Fricker (2012), Analysis of low-frequency seismic signals generated during a multiple-iceberg calving event at Jakobshavn Isbræ, Greenland, *J. Geophys. Res. Earth Surf.*, *117*(F1), 1–11, doi:10.1029/2011JF002132.

Walter, F., P. D. Canassy, S. Husen, and J. F. Clinton (2013), Deep icequakes: What happens at the base of Alpine glaciers?, *J. Geophys. Res. Earth Surf.*, *118*(3), 1720–1728, doi:10.1002/jgrf.20124.

Walter, F., P. Roux, C. Roeoesli, A. Lecointre, D. Kilb, and P.-F. Roux (2015), Using glacier seismicity for phase velocity measurements and Green's function retrieval, *Geophys. J. Int.*, *201*(3), 1722–1737, doi:10.1093/gji/ggv069.

Wang, W., H. J. Zwally, C. L. Hulbe, M. J. Siegert, and I. R. Joughin (2003), Anisotropic ice flow leading to the onset of Ice Stream D , West Antarctica : Numerical modelling based on the observations from Byrd Station borehole, *Ann. Glaciol.*, *37*, 397–404, doi:10.3189/172756403781815591.

Wang, Y., T. Thorsteinsson, J. Kipfstuhl, H. Miller, D. Dahl-Jensen, and H. Shoji (2002), A vertical girdle fabric in the NorthGRIP deep ice core, North Greenland, *Ann. Glaciol.*, *35*, 515–520, doi:10.3189/172756402781817301.

West, M., C. Larsen, M. Truffer, S. O'Neel, and L. LeBlanc (2010), Glacier microseismicity, *Geology*, *38*(4), 319–322, doi:10.1130/G30606.1.

Wiens, D. A., S. Anandakrishnan, J. P. Winberry, and M. A. King (2008), Simultaneous teleseismic and geodetic observations of the stick-slip motion of an Antarctic ice stream, *Nature*, *453*(7196), 770–774, doi:10.1038/nature06990.

Winberry, J. P., S. Anandakrishnan, and R. B. Alley (2009), Seismic observations of transient subglacial water-flow beneath MacAyeal Ice Stream, West Antarctica, *Geophys. Res. Lett.*, *36*(L11502), 1–5, doi:10.1029/2009GL037730.

Winberry, J. P., S. Anandakrishnan, D. A. Wiens, and R. B. Alley (2013), Nucleation and seismic tremor associated with the glacial earthquakes of Whillans Ice Stream, Antarctica, *Geophys. Res. Lett.*, *40*(2), 312–315, doi:10.1002/grl.50130.

Winberry, J. P., S. Anandakrishnan, R. B. Alley, D. A. Wiens, and M. Pratt (2014), Tidal pacing, skipped slips and the slowdown of Whillans Ice Stream, Antarctica, *J. Glaciol.*, *60*(222), 795–807, doi:10.3189/2014JoG14J038.

Wuestefeld, A., O. H. Al-Harrasi, J. P. Verdon, J. Wookey, and J. M. Kendall (2010), A strategy for automated analysis of passive microseismic data to image seismic anisotropy and fracture characteristics, *Geophys. Prosp.*, *58*(5), 755–773, doi:10.1111/j.1365-2478.2010.00891.x.

Zhu, L., and L. A. Rivera (2002), A note on the dynamic and static displacements from a point source in multilayered media, *Geophys. J. Int.*, *148*(3), 619–627, doi:10.1046/j.1365-246X.2002.01610.x.

Appendices

A Elastic Wave Velocities Through a Single Ice Crystal

Elastic wave phase velocities for a single ice crystal, from *Maurel et al.* (2015), used to generate Figure 1.3b:

$$\rho {V_P}^2 = \tfrac{1}{2}[C + L + (A - C)sin^2\theta + \sqrt{D}]$$

$$\rho {V_{SV}}^2 = \tfrac{1}{2}[C + L + (A - C)sin^2\theta - \sqrt{D}]$$

$$\rho {V_{SH}}^2 = Lcos^2\theta + Ncos^2\theta]$$

$$D = [Asin^2\theta - Ccos^2\theta][Asin^2\theta - Ccos^2\theta + 2L(cos^2\theta - sin^2\theta)] + 4sin^2\theta cos^2\theta(F^2 + 2FL) + L^2$$

Where θ is the phase angle, with 0° being vertical and 90° being horizontal and ρ being the density of ice (917 kgm^{-1}). A, C, F, L and N are the elastic parameters for a single ice crystal from *Bennett* (1968):

$$A(C_{11} = C_{22}) = 14.06 \times 10^9 Nm^{-2}$$

$$C(C_{33}) = 15.24 \times 10^9 Nm^{-2}$$

$$F(C_{13} = C_{31} = C_{23} = C_{32}) = 5.88 \times 10^9 Nm^{-2}$$

$$L(C_{44} = C_{55}) = 3.06 \times 10^9 Nm^{-2}$$

$$N(C_{66}) = 3.455 \times 10^9 Nm^{-2}$$

The terms in brackets refer to the Voigt notation (*Voigt*, 1910) for the terms of the elasticity tensor:

$$C = \begin{bmatrix} A & A-2N & F & 0 & 0 & 0 \\ A-2N & A & F & 0 & 0 & 0 \\ F & F & C & 0 & 0 & 0 \\ 0 & 0 & 0 & L & 0 & 0 \\ 0 & 0 & 0 & 0 & L & 0 \\ 0 & 0 & 0 & 0 & 0 & N \end{bmatrix}$$